# Light scattering and trapping in thin film silicon solar cells with an n-i-p configuration

Wanjiao Böttler

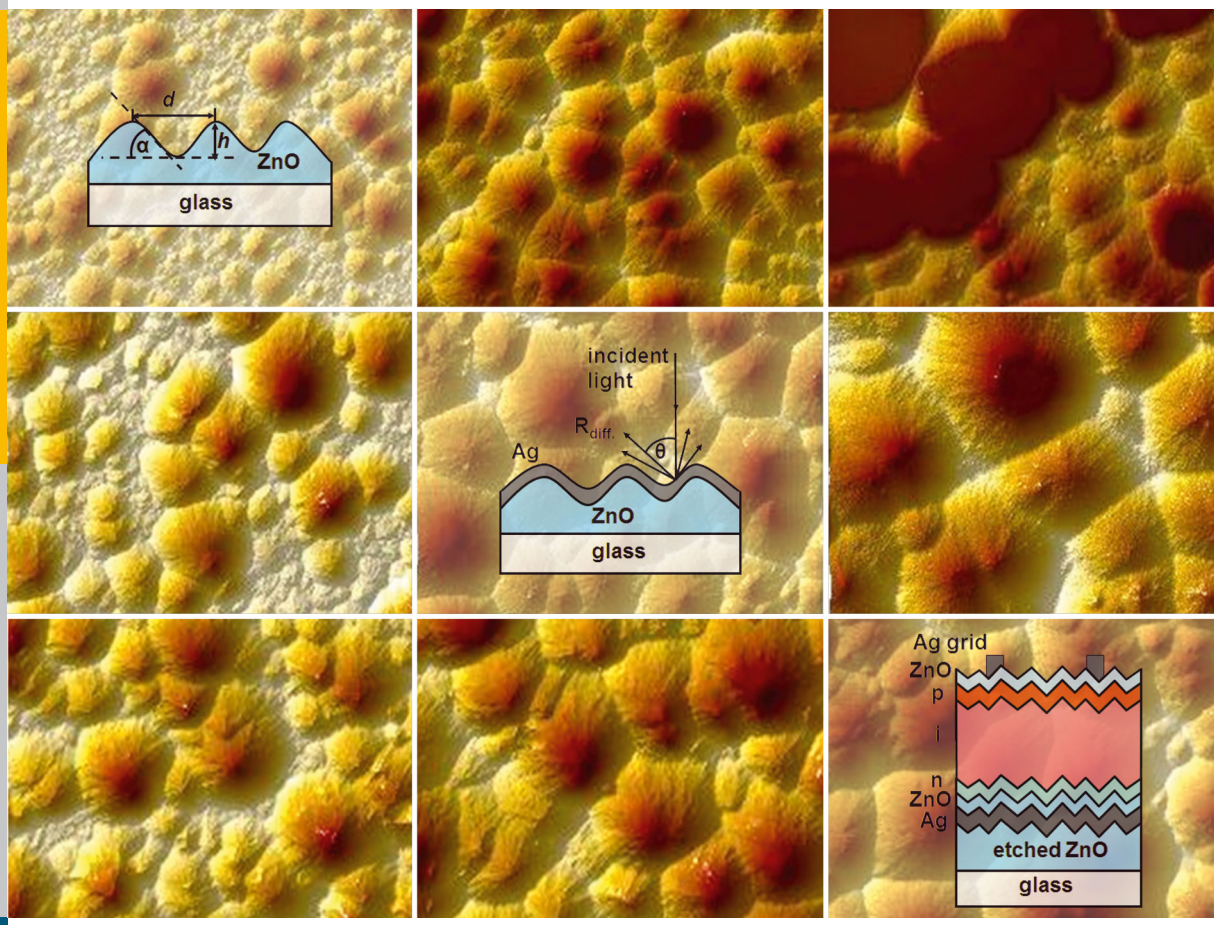


Energie & Umwelt / Energy & Environment
Band / Volume 245
ISBN 978-3-95806-023-4

JÜLICH
FORSCHUNGSZENTRUM

Schriften des Forschungszentrums Jülich
Reihe Energie & Umwelt / Energy & Environment Band / Volume 245

Forschungszentrum Jülich GmbH
Institute of Energy and Climate Research
IEK-5 Photovoltaics

# Light scattering and trapping in thin film silicon solar cells with an n-i-p configuration

Wanjiao Böttler

Schriften des Forschungszentrums Jülich
Reihe Energie & Umwelt / Energy & Environment Band / Volume 245

ISSN 1866-1793 ISBN 978-3-95806-023-4

Bibliographic information published by the Deutsche Nationalbibliothek.
The Deutsche Nationalbibliothek lists this publication in the Deutsche Nationalbibliografie; detailed bibliographic data are available in the Internet at http://dnb.d-nb.de.

Publisher and Distributor: Forschungszentrum Jülich GmbH
Zentralbibliothek
52425 Jülich
Tel: +49 2461 61-5368
Fax: +49 2461 61-6103
Email: zb-publikation@fz-juelich.de
www.fz-juelich.de/zb

Cover Design: Grafische Medien, Forschungszentrum Jülich GmbH

Printer: Grafische Medien, Forschungszentrum Jülich GmbH



Schriften des Forschungszentrums Jülich
Reihe Energie & Umwelt / Energy & Environment, Band / Volume 245

D 82 (Diss. RWTH Aachen University, 2014)

ISSN 1866-1793
ISBN 978-3-95806-023-4

The complete volume is freely available on the Internet on the Jülicher Open Access Server (JuSER) at www.fz-juelich.de/zb/openaccess.

# Contents

# Abstract

Microcrystalline silicon *μc-Si:H* thin film solar cells with an n-i-p configuration were set up based on the optimized processes for solar cells with a *p-i-n* configuration. The deposition processes of window, absorber and front contact layers were optimized. The effects of the thickness and doping ratio of *p*-type layers, the thickness of the front contact layers and the silane concentration of the absorber layers on the solar cell performance were investigated. For all the optimization and investigation, solar cells were prepared on simple glass/etched-*ZnO* substrates. To improve the short circuit current density, a highly reflective *Ag*/*ZnO* back reflector was added on glass/etched-*ZnO* substrates. Finally, a good process reproducibility and high cell performance were achieved as a base for the subsequent study of light scattering and trapping in *μc-Si:H n-i-p* solar cells.

The effects of the surface morphology of back reflectors on their light-scattering properties and the light trapping in *μc-Si:H n-i-p* solar cells were investigated. Firstly, the surfaces of sputtered *ZnO* layers were textured by etching them in *HCl* solution. The surface morphology was varied by changing the as-deposited *ZnO* thickness and etching time and measured by Atomic Force Microscopy *AFM*. Based on the *AFM* measurement results, statistically evaluation of the *ZnO* surface morphology was performed in terms of not only the rms roughness but also the diameter, depth and angle of surface features (craters) on the surfaces. With such evaluation, the relationship between the surface morphology and light-scattering properties of reflectors was analysed and related to different physical mechanisms, such as diffraction and geometrical optics. Finally, etched-*ZnO* layers with different surface morphologies were covered with a thin *Ag* and *ZnO* layer and used together as back reflectors in *μc-Si:H n-i-p* solar cells. This allows us to analyse the direct link between the surface morphology of back reflectors and light trapping in the solar cells. With this analysis, the most beneficial size and angle of craters for light trapping were estimated. In addition, to better understand the light trapping process in the solar cells, angular intensity distributions *AID*s in silicon were simulated by the so-called "phase model" both for the transmission at the *ZnO*/*μc-Si:H* interface (as on the front side of solar cells) and for the reflection at the back reflector. The *AID*s for the transmission were compared to those for the reflection with the same interface morphologies to estimate the dominant scattering process regarding the light trapping in solar cells.

# Zusammenfassung

Die Optimierung von mikrokristallinen Silizium(*µc-SiH*)-Dünnschichtsolarzellen in einer *n-i-p*-Konfiguration erfolgte unter Anwendung bereits optimierter Prozesse für Solarzellen in einer *p-i-n* Konfiguration. Die Depositionsprozesse für Fenster-, Absorber- und Frontkontaktschichten wurden optimiert. Der Einfluss der Dicke und des Dotierverhältnisses von *p*-Typ-Schichten, die Dicke des Frontkontakts und die Silankonzentration bei der Deposition der Absorberschichten wurden im Hinblick auf die Solarzelleneigenschaften untersucht. Für diese Optimierung und Untersuchung wurden Solarzellen auf einfachen Glas/geätzten-*ZnO*-Substraten hergestellt. Um die Kurzschluss-Stromdichte zu erhöhen, wurden stark reflektierende *Ag/ZnO* Rückreflektoren auf den Glas/geätzten-*ZnO*-Substraten abgeschieden. Schließlich wurden eine gute Prozessreproduzierbarkeit und hohe Effizienzen von *µc-Si:H*-Solarzellen in der *n-i-p* Konfiguration sichergestellt, um die Lichtstreuung und den Lichteinfang (engl.: light-trapping) in den Solarzellen zu untersuchen.

Der Einfluss der Oberflächenmorphologie von Rückreflektoren in *µc-Si:H*-Solarzellen auf ihre lichtstreuenden Eigenschaften und das light-trapping-Verhalten in Solarzellen wurden untersucht. Zunächst wurden die Oberflächen der gesputterten *ZnO*-Schichten durch einen Ätzprozess in verdünnter Salzsäure *HCl* texturiert. Durch Variation der *ZnO*-Schichtdicke und Ätzzeit wurde die Oberflächenmorphologie variiert und anschließend mit Hilfe der Rasterkraftmikroskopie (engl.: Atomic Force Microscopy *AFM*) vermessen. Basierend auf diesen *AFM*-Messungen wurde eine statistische Auswertung der *ZnO*-Oberflächenmorphologie durchgeführt, wobei neben der quadratischen Rauigkeit auch der Durchmesser, die Tiefe und die Winkel der Oberflächenstrukturen (Krater) in Betracht gezogen wurden. Aus diesen detaillierten Auswertungen wurde der Zusammenhang zwischen der Oberflächenmorphologie und der Lichtstreueigenschaften des Reflektors untersucht und auf verschiedene physikalische Mechanismen wie Beugung und geometrische Optik zurückgeführt. Schließlich wurden die geätzten *ZnO*-Schichten mit unterschiedlichen Oberflächenmorphologien mit einer dünnen *Ag*- und *ZnO*-Schicht bedeckt und zusammen anschließend als Rückreflektoren in *n-i-p µc-Si:H*-Solarzellen verwendet. Dies ermöglichte den direkten Zusammenhang zwischen der Oberflächenmorphologie von Rückreflektoren und das light-trapping in den Solarzellen zu analysieren. Mit dieser Analyse wurden die optimale Größe und der optimale Winkel der Krater für das light-trapping abgeschätzt. Um den light-trapping-Prozess in den Solarzellen besser zu verstehen, erfolgte darüber hinaus eine Simulation der winkelabhängigen Lichtintensitätsverteilung (engl.: Angular Intensity

Distribution *AID*) in Silizium unter Anwendung des sogenannten „Phasenmodels“. Die Simulation wurde sowohl für die Transmission an der *ZnO/μc-Si:H*-Grenzfläche (auf der Vorderseite der Solarzellen) als auch für die Reflexion am Rückreflektor durchgeführt. Durch einen Vergleich zwischen der simulierten *AID* für die Transmission und für die Reflexion wurde der dominierende Lichtstreuungs-Prozess für das light-trapping in Solarzellen bestimmt.

# 1. Introduction

With rising environmental issues and energy demand, utilization of renewable energy becomes a global consensus. The most abundant renewable energy resource is solar energy, which can be directly converted into electrical power by using solar cells. Solar cells can be prepared by certain semiconductors which exhibit the photovoltaic effect, such as crystalline silicon (mono- and multi-crystalline silicon), thin film silicon (amorphous or microcrystalline silicon), cadmium telluride, copper indium gallium selenide/sulfide, Gallium arsenide and polymers (organic semiconductors). Up to now, crystalline silicon is still mostly used as light absorbers for solar cells, since silicon is extremely abundant raw material in the earth and crystalline silicon yields stable solar cells with relatively good efficiencies. Based on the report in the journal "Progress in photovoltaics: research and application" in April 2012 [1], the highest efficiency is 24.4 % [2] for mono-crystalline solar cells and 20.3% [3] for multi-crystalline solar cells.

Besides crystalline silicon, thin film silicon (amorphous and microcrystalline silicon) has been also intensively developed for solar cells [4,5]. Thin silicon films can be deposited at low substrate temperatures (below 200°C) by chemical vapor deposition *CVD*. The low temperatures lead to reduce energy consumption for the fabrication. Moreover, flexible substrates, such as metal- or plastic-foils, can be used for thin film silicon solar cells and modules which can be better integrated into buildings than wafer-based crystalline silicon modules. However, the stabilized efficiency of thin film silicon solar cells is still much lower than that of crystalline silicon solar cells. The highest stabilized efficiencies of thin film silicon solar cells are only around 10% for single junction cells [6–8] and 12.4% for triple junction cells [9]. One of the reasons for the relatively low efficiencies is the poor electrical transport properties of silicon thin film materials, which leads to the difficulty in collection of photo-generated charge carriers. The charge carrier collection can be improved by decreasing the thickness of the intrinsic absorber layers in thin film silicon solar cells. However, with decreasing the absorber thickness, the light absorption and consequently the photo current is reduced. To increase the optical path length of light and to achieve a high absorption even in thin absorber layers, light-trapping concepts are usually used and of greatest importance for thin film silicon solar cells.

A common way to achieve light trapping is adding back reflectors and textured interfaces into solar cells. By back reflectors, the light which is not absorbed can be reflected back into

the absorber layers. By textured interfaces, the light can be scattered to different directions. If the angle between the reflected light from the back reflectors and the front surfaces of the solar cells is larger than the critical angle for internal reflections, the light will be "trapped" within the solar cells. Thus, light can travel several times within the absorber layers and the optical path length can be significantly improved.

Textured interfaces for light trapping can be placed on the front or back side of solar cells, dependent on the solar cell configuration. According to the deposition sequence of silicon layers, there are two typical configurations for thin film silicon solar cells, the *p–i–n* and *n–i–p* configurations. In the *p–i–n* configuration, silicon layers are deposited with a sequence of *p*-type, intrinsic and *n*-type layers, while they are deposited with a reverse sequence in the *n–i–p* configuration. For both configurations, the light is commonly illuminated from the *p*-type layer. Therefore, in the *p–i–n* configuration, transparent glass substrates have to be used. Moreover, in this configuration, textured interfaces for light trapping are usually provided by transparent conductive oxides *TCO*s deposited on glass substrates [8,10–14], since it is difficult to texture deposited silicon layers on the back side of solar cells. However, as front contacts, *TCO* layers have a number of requirements on their properties besides the light-scattering properties, such as high transparency and low sheet resistance. Therefore, the optimization of the light-scattering properties is limited and one has usually to work with trade-offs between non-ideal properties of *TCO* layers. On the other hand, in the *n–i–p* configuration, substrates do not have to be optically transparent and textured interfaces for light trapping are usually provided by substrates or back reflectors on the back side of solar cells [15–21]. Although one can also use textured front *TCO*s for light trapping in *n–i–p* solar cells, using textured substrates or back reflectors on the back side has an advantage that the surface morphology can be flexibly varied to improve the light-scattering properties, without taking care about other electrical or optical properties of the textured layers. Thus, the *n–i–p* configuration and textured back reflectors were used in this work to study light scattering and trapping in thin film silicon solar cells.

Up to now, different surface morphologies have been used in thin film silicon solar cells for light trapping [8,10–12,15–21]. However, these surface morphologies have quite different shape and size of textures and it is difficult to compare with each other concerning the effects on light trapping. The optimal surface morphology for light trapping is still under discussion and the relationship between the surface morphology and light trapping is still not fully understood. For periodically textured surfaces, the average period *P* of textures was usually used to describe the surface morphology and related to light trapping in solar cells [18,22].

For randomly textured surfaces, the rms roughness $\delta_{rms}$ was usually used to describe the surface morphology, like in the cases of randomly textured *Ag* [21] and *ZnO* [13,14]. However, the rms roughness alone is not sufficient to determine a surface morphology exactly [23]. A surface morphology can be descried in more details by the size and angle of textures. According to the physical mechanisms for light scattering, diffraction and geometrical optic, the lateral size and angle of textures may have also impact on the light-scattering properties. Nevertheless, it is hard to find investigations in the literature about the effects of size or angle of random textures on light scattering and trapping in solar cells. The reasons could be that the size and angle of random textures are difficult to control experimentally and evaluate quantitatively.

In this work, we find approaches to vary the size and angle of textures (craters) on sputtered *ZnO* layers independently and evaluate statistically the surface morphology in terms of not only the rms roughness, but also the diameter, depth and angle of craters. With such variations, the relationship between the surface morphology and the light scattering properties of textured-*ZnO/Ag* reflectors was investigated in details and explained by physical mechanisms: diffraction and geometrical optics. Furthermore, textured-*ZnO* was covered with a thin *Ag* and *ZnO* films and used together as back reflectors in *μc-Si:H n-i-p* solar cells. By doing so, the relation between surface morphology of back reflectors and light trapping in solar cells can be analysed directly, without taking care of electrical and optical properties of the textured-*ZnO* layers. With these analyses, the most beneficial crater size and angle for light trapping were proposed. In addition, to better understand the light trapping process in the solar cells, angular intensity distributions *AID*s in silicon were simulated by the so-called "phase model" both for the transmission at the *ZnO/μc-Si:H* interface (as on the front side of solar cells) and for the reflection at the back reflector. By comparing the *AID*s at the *μc-Si:H/ZnO* interface to those at back reflectors, the dominant scattering process regarding the light trapping in solar cells was estimated. The outline of this work is as follows:

In Chapter 2, the theory and background relevant for this work are introduced.

In Chapter 3, the experimental details are described. The layer arrangements of the *p-i-n* and *n-i-p* solar cells used in this work are introduced. The preparation methods and main parameters for the *TCO* and silicon layers are given.

In Chapter 4, characterization methods used in this work are introduced.

In Chapter 5, we present the results and discussions during transferring the existing optimized processes for *μc-Si:H* solar cells with a *p-i-n* configuration to *n-i-p μc-Si:H* solar cells. The window, absorber layers and substrates in *n-i-p μc-Si:H* solar cells were optimized

to achieve good process reproducibility and high cell performance for the study of the light scattering and trapping in solar cells. The effects of the thickness and doping ratio of *p-type* layers, the thickness of front *TCO* layers and the silane concentration of absorber layers on the cell performance are shown. Two types of substrates (glass/etched-*ZnO* and glass/etched-*ZnO*/*Ag*/*ZnO*) were used in *μc-Si:H n-i-p* solar cells. The effects of adding the highly reflective *Ag/ZnO* back reflector are presented.

In Chapter 6, the effects of the back reflector surface morphology on their light-scattering properties and the performance of *μc-Si:H n-i-p* solar cells are presented and discussed. Firstly, we show the variation and evaluation of the etched-*ZnO* surface morphology. Then, based on the evaluation, the relationship between the surface morphology and light-scattering properties for the reflection is analysed and related to different physical mechanisms, such as diffraction and geometrical optics. Finally, the relationship between the back reflector morphology and light trapping in solar cells is analysed. Based on the analysis, we propose which size, angle and shape of craters could be most beneficial for light trapping. In addition, the angular intensity distributions *AID*s in silicon were simulated both for the transmission at the *ZnO/μc-Si:H* interface and for the reflection at the back reflector. The *AID*s for the transmission are compared to those for the reflection to estimate the dominant scattering process regarding the light trapping in solar cells.

Finally, Chapter 7 provides a short summary.

# 2. Fundamentals

This chapter presents the theory and background relevant for this work. Firstly, we will briefly introduce the deposition techniques and properties of thin film silicon materials (hydrogenated amorphous and microcrystalline silicon). Then, the typical configurations of thin film silicon solar cells and the textured layers commonly used for light trapping in each configuration will be described. In this work, we focused on solar cells with an n-i-p configuration and used texture-etched zinc oxide *ZnO* as a base for the back reflectors for light trapping. Thus, several growing and etching models for *ZnO* films developed in the past will be summarized to better understand the etching behaviour of *ZnO* films in our case. In literature, various materials with different surface morphologies have been used for light trapping in thin film silicon solar cells. In this chapter, an overview and comparison of those surface morphologies will be given. Moreover, we will introduce several simulation models for light scattering at textured interfaces, which are important to understand the links between the surface morphology, light-scattering properties of back reflectors and light trapping in solar cells.

## 2.1 Hydrogenated amorphous and microcrystalline silicon

Both hydrogenated amorphous silicon *a-Si:H* and hydrogenated microcrystalline silicon *μc-Si:H* are disordered materials and can be deposited with a mixture of silane and hydrogen by chemical vapour deposition, such as plasma enhanced chemical vapour deposition *PECVD* [24–27] and hot-wire chemical vapor deposition *HWCVD* [26,28,29]. In this work, all the *a-Si:H* and *μc-Si:H* layers are grown by *PECVD*.

**Hydrogenated amorphous silicon *a-Si:H***

Amorphous silicon consists of a covalent random network of *Si-Si* and *Si-H* bonds with only a short range order. A long range disorder is represented by deviations in the bond lengths and angles of *Si-Si* bonds. These deviations result in scattering and even localization of carries, which reduces the carrier mobility. For example, the electron mobility in *a-Si:H* is only 0.1~1 $cm^2$/Vs, two or three orders of magnitude lower than in c-Si. Moreover, the long range disorder influences the distribution of states and causes a broadened tail of the conduction and valence band. Along the band edge, extended and localized states are

separated by the so-called “mobility edge”. With the mobility edges for the conduction and valence band, the mobility band gap is defined, which is around 1.7 eV for hydrogenated amorphous silicon [24].

Besides bonds with length and angle deviations, there are also a large amount of broken bonds in amorphous silicon, which generate defects (dangling bonds) in the mid-gap region. These dangling bonds act as recombination centres for charge carriers. And the lifetime of charge carriers is influenced by the density of these defects. The defect density can be significantly reduced by hydrogenation of amorphous silicon. However, the lifetime of charge carriers in hydrogenated amorphous silicon *a-Si:H* (order of 1 µs) is still much shorter than that in *c-Si* (100 µs ~ 1ms).

Moreover, hydrogenated amorphous silicon suffers from the light-induced degradation effect (Staebler-Wronski effect) [30,31]. Staebler and Wronski found in 1977 [30] that the dark conductivity and photoconductivity of amorphous silicon were reduced significantly during the illumination. This reduction can be attributed to an increase of the defect density by breaking weak *Si-Si* bonds.

**Hydrogenated microcrystalline silicon *µc-Si:H***

Hydrogenated microcrystalline silicon *µc-Si:H* can be considered as a mixture of crystallites, amorphous tissue, grain boundaries and voids. The volume fraction and spatial distribution of crystallites depend on the deposition conditions and substrate [7,27,32–35]. Vetterl et al. [36] described the growth and structure properties of *µc-Si:H* films as shown Figure 2.1. From the left to the right, the crystalline volume fraction decreases. In the high crystalline material (on the left side), large columns with diameters up to 200 nm extend to the whole film and separated by voids and cracks. These large columns consist of many coherent domains. With decreasing the crystalline volume fraction, the size of columns and coherent domains decrease. In *µc-Si:H* films with medium crystalline volume fractions, columns are passivated by amorphous tissues. With a further decrease in the crystalline volume fraction, columns are disrupted, resulting in small grains embedded in the amorphous network. Moreover, an incubation zone for the growth of *µc-Si:H* films is shown in the structure diagram from Vetterl et al. (see Figure 2.1). In the incubation zone, the crystallinity and column diameter increase with the thickness. At a certain thickness (commonly 30~50 nm), the columns connect to each other and form a stationary growth. The thickness and crystallinity of the incubation zone may vary depending on the particular deposition conditions and substrate [32].

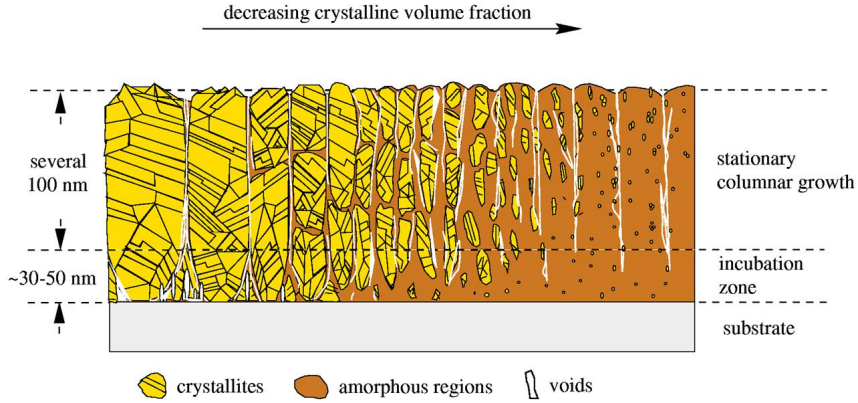


*Figure 2.1 Schematic diagram illustrating the structure properties of µc-Si:H films. From the left to the right, the crystalline volume fraction decreases. This diagram was shown in Ref.* [36].

Hydrogenated microcrystalline silicon has electrical and optical properties more similar to crystalline silicon than hydrogenated amorphous silicon. Highly crystalline *µc-Si:H* material has an "effective" band gap of around 1.1 eV, quite similar to *c-Si*. Moreover, only little light-induced degradation has been found in *µc-Si:H* material [37,38]. However, the electrical transport properties (mobility and lifetime of charge carriers) of *µc-Si:H* are much lower than those of *c-Si* [38–40], due to disorders and defects in the material.

## 2.2 Solar cells based on thin film silicon

**Introduction**

For *c-Si* solar cells, a *p-n* junction is used as the cell structure and collection of photo-generated carriers is obtained by diffusion of charge carrier within the *p-* and *n-type* layers. However, this cell structure is not suitable for solar cells based on thin film silicon (*a-Si:H* and *µc-Si:H*), since the diffusion length $L_D$ of charge carriers in thin film silicon material is too short to collect photo-generated carriers. The diffusion length in *c-Si* wafer is over 200 µm, while the diffusion length in intrinsic *a-Si:H* and *µc-Si:H* is only the order of 0.1 µm [39,41,42]. The much shorter diffusion length in thin film silicon than in *c-Si* results from the lower mobility and lifetime of charge carriers, described in Section 2.1. Thus, instead of a *p-n* junction, a *p-i-n* structure is typically used for thin film silicon solar cells, where *i* represents

an intrinsic layer. By separating the thin (20~30 nm) *p*- and *n*-type layers with a relative thick (1~3 μm) intrinsic layer, an internal electric field is built in solar cells. Most of the incident light is absorbed in the intrinsic layer and converts to electrons and holes. Electrons and holes generated in the intrinsic layer can be driven by the internal electric field to the *p*- and *n*-type layers, respectively.

With a *p-i-n* cell structure, the collection of photo-generated charge carrier in thin film silicon solar cells depends on not only the electrical properties (mobility and lifetime of carriers) but also the thickness of intrinsic layers. A decrease in the thickness of intrinsic layers leads to a stronger internal electric field and a shorter path for photo-generated carriers to travel, which can result in an improvement in carrier collection. However, a decrease in the thickness of intrinsic layers leads to a decrease in light absorption and therefore to a lower short circuit current density of the solar cells. To achieve a high light absorption even in thin intrinsic layers, light-trapping concepts have been used to increase the optical path length of light in intrinsic layers. A common way to achieve light trapping is using back reflectors and textured interfaces in solar cells [11,15,18,43–45]. By back reflectors, the light which is not absorbed can be reflected back into the intrinsic (absorber) layers. By textured interfaces, light can be scattered into different directions. If the angle between the scattered light and the front surfaces of solar cells is larger than the critical angle for internal reflections, the light will be "trapped" within the solar cells. Thus, the incident light can travel several times within the absorber layers and the optical path length can be significantly increased. More details about light trapping in thin film silicon solar cells and the light-scattering properties of textured surfaces will be introduced in Section 2.4.

**Configurations of solar cells**

According to the deposition sequence of silicon layers, two types of configurations are usually used for thin film silicon solar cells, as shown in Figure 2.2. In the so-called *p-i-n* configuration (see Figure 2.2 (a)), silicon layers are deposited with a sequence of *p*-typed (*p*), intrinsic (*i*) and *n*-typed (*n*) layers. In the so-called *n-i-p* configuration (see Figure 2.2 (b)), silicon layers are deposited with a sequence of *n*-typed (*n*), intrinsic (*i*) and *p*-typed (*p*) layers. For both configurations, light is commonly illuminated from the *p*-typed layer side. Therefore, in solar cells with a *p-i-n* configuration, transparent substrates (glass) are required and textured transparent conducting oxides *TCO*s are usually used for light trapping. In the past, different textured *TCO*s have been used, such as tin oxide $SnO_2$ [12,46] and zinc oxide *ZnO* [11,13,14,47–49]. There are several requirements for *TCO*s in *p-i-n* solar cells: high

conductivity for carrier transport, high transmission for incident light and efficient texture for light trapping. These properties of *TCO*s are difficult to vary independently and one has usually to find trade-offs between non-ideal properties.

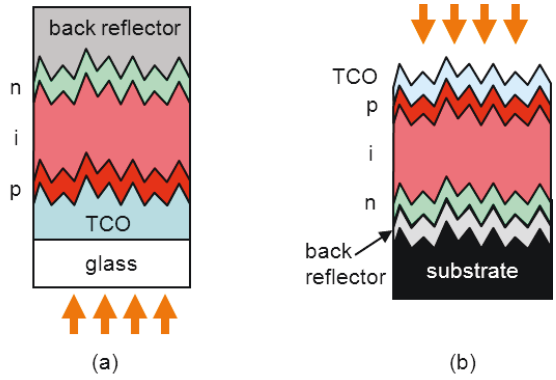


*Figure 2.2 Schematic diagram of a solar cell with (a) the p-i-n configuration and (b) the n-i-p configuration*

In solar cells with an n-i-p configuration, substrates do not have to be transparent, since light is not illuminated from the substrate side (see Figure 2.2 (b)). Thus, opaque, flexible or low-cost materials can also be used as substrates. Solar cells on flexible substrates, such as metal [15,17,50,51] and plastic foils [19,52–54], can be better integrated into buildings. In addition, in the *n-i-p* configuration, textured layers are usually placed at the rear side of solar cells. It is more flexible to modify the surface morphology of substrates or back reflectors for light trapping in the *n-i-p* configuration than the surface morphology of *TCO*s in the *p-i-n* configuration, since the modification of the *TCO* surface morphology is limited by the requirements for its electrical and optical properties.

In this work, we used the *n-i-p* configuration for solar cells. The effects of the back reflector morphology on the light scattering & trapping in solar cells were investigated (described in Chapter 6). The back reflectors used in the *n-i-p* solar cells were prepared by covering textured *ZnO* layers with a highly reflective *Ag* layer and a thin *ZnO* layer. The function for light trapping was realized by the first textured *ZnO* layer, which was prepared by sputtering and then etching in *HCl* solution. Thus, varying the surface morphology of

sputtered *ZnO* layers was one of the critical tasks in this work. In the next section, we will summarize the growing and etching models of sputtered *ZnO* films developed in the past.

## *2.3* Growing and etching of sputtered zinc oxide films

Zinc oxide *ZnO* thin films can be deposited by many different techniques, like magnetron sputtering [55–58], chemical vapour deposition *CVD* [47,48], pulsed laser deposition *PLD* [59,60] and evaporation [61,62]. Of these techniques, *CVD* and magnetron sputtering can be used for producing thin film solar cells, since large-area films can be deposited with low cost and the surface can be textured for light trapping. Magnetron sputtering was used in this work to prepare *ZnO* layers. Details about the sputtering process of *ZnO* films have been well described by Kluth [63] and Berginski [64]. Textured surfaces can be achieved by etching sputtered *ZnO* films in *HCl* solution [11,56,65]. The surface morphology after etching depends on the etching conditions (like the dilution of the acidic solution, etching time, temperature) [66] and the microstructure (like the compactness) of *ZnO* films [11,67–69]. The microstructure of *ZnO* films is influenced by the growth conditions [11,13,67,68,70]. Based on these results, several models were developed to describe the growth and etching behaviours of sputtered *ZnO* films, which will be described in more details in the following.

**Thornton model**

Thornton developed a model to describe the effects of the deposition conditions on the growth of sputtered films [71,72]. It was found that the growth of sputtered films depends on the substrate temperature and pressure, which can influence the mobility of adatoms. As shown in Figure 2.3, there are four structure zones dependent on the relative temperature ($T$s/$T_m$) and sputtering pressure in the Thornton model, where $T_s$ is defined as the substrate temperature and $T_m$ as the melting temperature.

Zone 1 is located at low substrate temperatures, from 10% of the $T_m$ at a pressure of 0.1 Pa to 40% of the $T_m$ at a pressure of 3 Pa. At these deposition conditions, the surface mobility of adatoms is so small that they stay close to the absorption site. Thus, initial nuclei grow in the direction of the sputter flux and develop to tapered crystals. Voids rather than grain boundaries may be formed between the crystals. Zone 2 is for relatively high substrate temperatures, between 40 and 75% of the melting temperature. In this region, the surface mobility of adatoms is quite high so that they can diffuse to preferred bonding sites. Moreover, at these high substrate temperatures, grain boundary migration and

recrystallization may occur and lead to large grains. Zone T exists between zones 1 and 2, for temperatures between 10% and 40% of the melting temperature dependent on the pressure. At these deposition conditions, the adatom mobility is higher than in zone 1 and leads to more dense films with crystals separated by grain boundaries. But the substrate temperatures are not high enough for grain boundaries to recrystallize. Thus, the crystals in this zone are smaller than in Zone 2. Further increasing the substrate temperature above 75% of the $T_m$ leads to the Zone 3 growth. In this region, the substrate temperature is high enough so that adatoms can diffuse into the bulk and the bulk can recrystallize. As a result, the material in Zone 3 consists of large crystals with a flat surface.

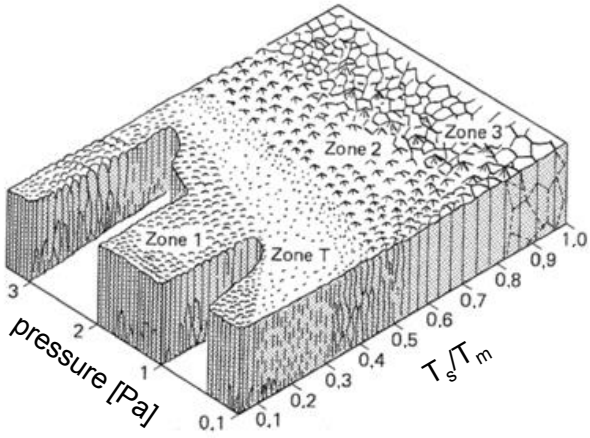


*Figure 2.3 Schematic diagram of the model for the growth of sputtered metal, given by Thornton* [71]. *Four structure zones are shown in the matrix of the relative temperature ($Ts/T_m$) and sputtering pressure.*

**Kluth model**

To describe the growth and etching behaviour of sputtered *ZnO* films, Kluth et al. proposed a "modified Thornton model" [11], which is shown in Figure 2.4. In the middle of Figure 2.4, the structure zones are shown in the matrix of the substrate temperature and deposition pressure. On the left and right sides, the *SEM* micrographs of *ZnO* films in different zones are shown for before and after *HCl* etching, respectively. Following modifications were made by Kluth et al. from the Thornton model: (1) Since the melting temperature of *ZnO* (1975 °C) is much higher than most metals and the typical substrate

temperatures are only between 80 and 400 °C, the relative temperature $T_s/T_m$ would be very small. Therefore, the substrate temperature *T*s was used in the modified model for *ZnO* films instead of the relative temperature $T_s/T_m$. (2) The pressure and temperature axis are exchanged, since it was noticed that the pressure played a more important role than the substrate temperature for sputtered *Zn*O films. (3) Zone 3 in the Thornton model is not included, since the substrate temperatures usually used for *ZnO* sputtering are much lower than the melting temperature of *ZnO* films. Thus, recrystallization of the bulk material described for Zone 3 in the Thornton model will never occur at any pressure.

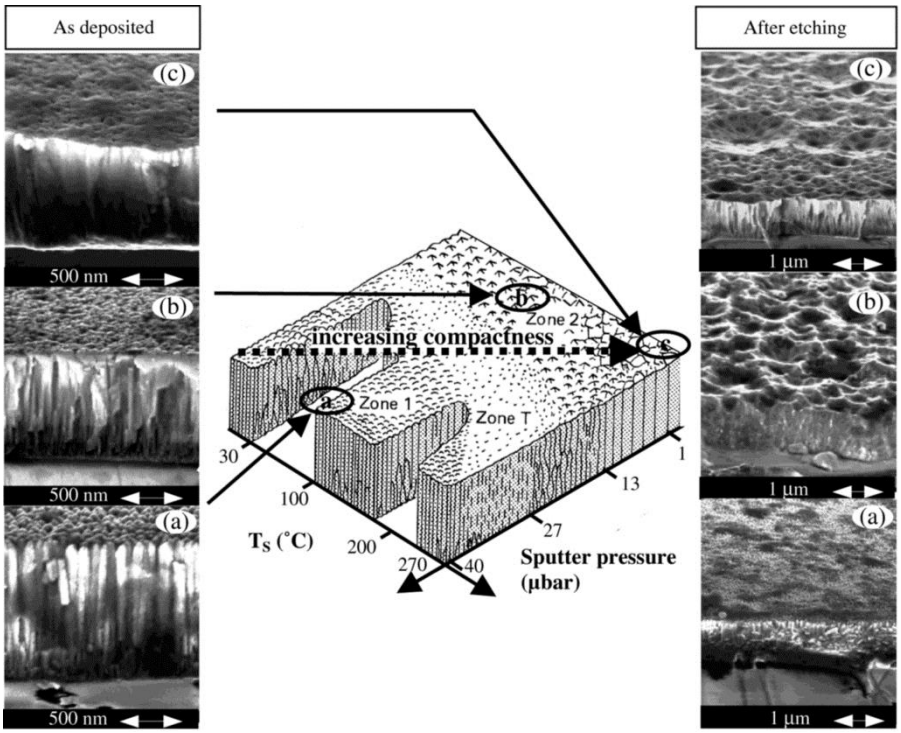


*Figure 2.4 The modified Thornton model for sputtered ZnO films as given by Kluth et al.* [11] . *In the middle, structure zones are shown in the matrix of substrate temperature and sputter pressure, according to the Thornton model* [71]. *On the left and right side, SEM micrographs of sputtered ZnO are shown for before and after etching in HCl solution, respectively.*

According to the surface morphology after etching, three types of *ZnO* were classified by Kluth et al. [11] in the modified Thornton model. Type *A ZnO* film was deposited at a high pressure and a low substrate temperature. For this type of *ZnO* films, crystals extend from the substrate to the top of the films and can be easily distinguished by the *SEM* cross-sections. In *HCl* solution, Type *A ZnO* film is relatively isotropically etched. After etching, the surface is quite flat and small hill-like structures can be seen on the surface. Type *B* and *C ZnO* films were deposited both at a low pressure, but at a low and high substrate temperature, respectively. For both Type *B* and *C* films, crystals are difficult to distinguish in the *SEM* micrographs, which may indicate a high compactness of films. The etching of both Type *B* and *C ZnO* are anisotropic in *HCl* solution, resulting in crater-like structures on the surfaces. The difference between Type *B* and *C ZnO* is that the surface of etched Type *B ZnO* is homogenously covered by craters with similar sizes, whereas the surface of etched Type *C ZnO* is composed of only few very large craters.

In the Kluth model, the different etching behaviours of *ZnO* films were related to the growth conditions and the resulting compactness of films. To further understand the relation between the etching behaviours and microstructure of sputtered *ZnO* films, Owen did more investigation and developed an etching model as shown in the following.

**Owen model**

Owen used different types of solution (*KOH*, *HCl* and *HF*) and conditions (temperature and concentration) to etch sputtered *ZnO* films in his work [66]. Based on the etching behaviours of *ZnO* films, Owen proposed an etching model for sputtered *ZnO* films with the following three postulates:

(1) Sputtered *Al* doped *ZnO* is polycrystalline and grown *Zn*-terminated. The *ZnO* grains on the surface with a (001) plane are hardly etched, whereas every grain boundary has a certain potential for etching. The etch potential depends on the disorder of the grain boundary. More disordered (more porous) grain boundaries may have a higher etch potential. A schematic representation of this postulate is shown in Figure 2.5 (a) with different colours for the different etch potentials of grain boundaries.

(2) The etching behaviour of sputtered *ZnO* films depends on the etching solution and conditions, which define an etching threshold. Grain boundaries with etch potentials above the threshold can be actively etched. Figure 2.5 (b) shows a schematic representation of this postulate. Etching solution with large molecule clusters can only etch large grain boundaries, while that with small molecules can also etch small grain boundaries.

(3) The vertical etch rate along grain boundaries depends on the nature of the grain boundary, the mobility and size of molecule or molecule clusters in etching solution. The horizontal etch rate depends on the concentration of etching solution and the crystal structure. Owen assumed that the etching of so-called "Type *B ZnO*" in *HCl* solution is limited by the vertical etch rate (see Figure 2.5 (c) left). The large etchants in *HCl* solution may only be able to slowly penetrate large grain boundaries, but expand horizontally quickly until the (101) planes [73,74]. On the other hand, the etching of *ZnO* films in *HF* is limited by the horizontal etch rate (see Figure 2.5 (c) right) and therefore can result in steeper opening angles of craters on the surfaces.

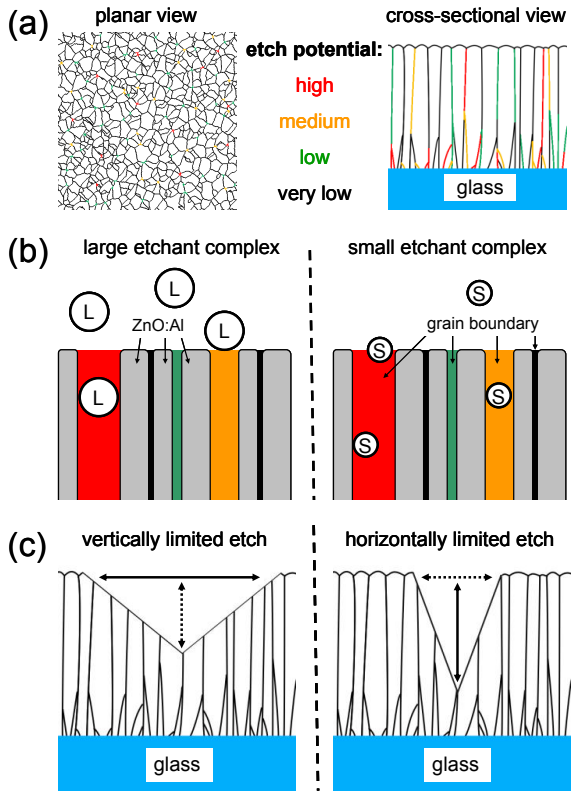


*Figure 2.5 Diagrams of the three postulates of the etching model* [66]*: (a) planar (left) and cross-sectional (right) views of a ZnO film with grain boundaries of different etch potentials, (b) interaction of the etchants with the ZnO film depending on the etchant size: large (left) and small (right) etchant complex, at grain boundaries of different etch potentials, (c)*

*resulting crater shape for large and small etchants with vertically (left) and laterally (right) limited etch rates.*

With these growing and etching models we introduced above, the variation of *ZnO* surface morphologies observed in this work will be analysed (in Chapter 6).

## 2.4 Light scattering and trapping in Si thin film solar cells

As described in Section 2.2, light trapping is of great importance for thin film silicon solar cells to increase the optical path of light in absorber layers. To achieve light trapping, textured interfaces are typically used in solar cells to scatter the light. For light trapping in thin film silicon solar cells, different surface morphologies with either random or periodic structures have been formed with various materials, such as randomly textured $SnO_2$ [14,75,76], *ZnO* grown by *LP-CVD* [8], sputtered *ZnO* [14,56,77], *Ag* [16,21,78], periodically textured $Al_2O_3$ [18], photoresist/*ZnO* [79] and plastic foils [19,20]. The *SEM* or *AFM* micrographs of some of the textured surface morphologies are showed in Figure 2.6. One can see that the surface morphologies are quite different with different sizes and shapes of surface features. Up to now, the optimal surface morphology for light trapping in thin film silicon solar cells is still under discussion.

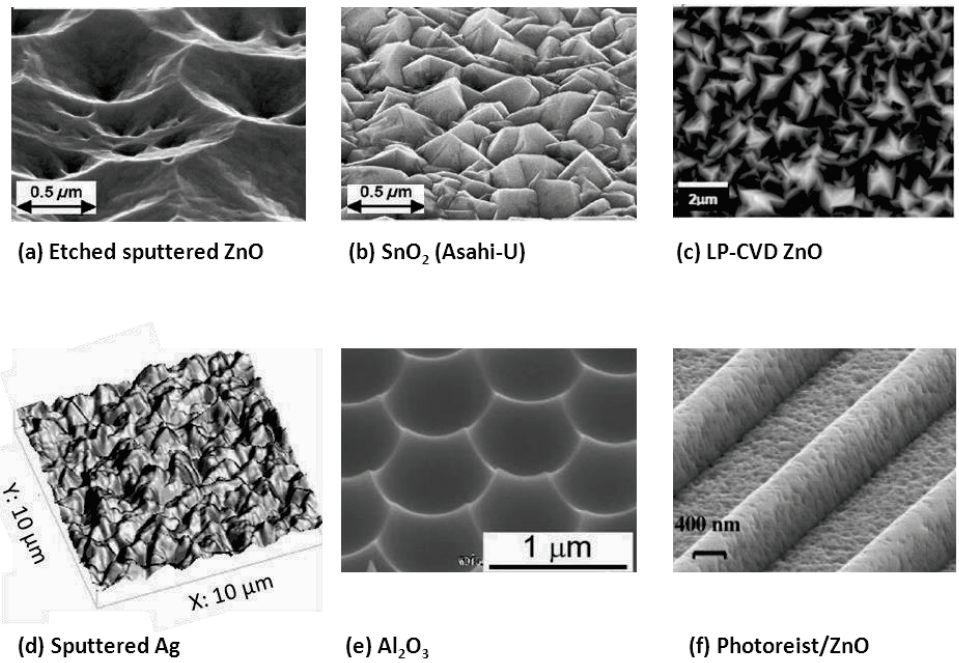


*Figure 2.6 Textured surface morphologies used for the light trapping in thin film silicon solar cells, formed with different materials, such as (a) etched sputtered ZnO* [14]*, (b) $SnO_2$ (Asahi-U)* [14]*, (c) LP-CVD ZnO* [8]*, (d) sputtered Ag* [78]*, (e) $Al_2O_3$* [18] *and (f) photoresist and ZnO* [79].

To understand the relationship between the surface morphology and light trapping in solar cells, the light-scattering properties of textured surfaces were often examined experimentally by two quantities: the haze and the angular intensity distribution *AID* [13,18,23,79–81]. The haze is defined by the ratio of the diffusely scattered light intensity to the total transmitted or reflected light intensity. The angular intensity distribution *AID* is a distribution of the light intensities at certain scattering angles. Several simulation models were proposed to describe the correlation between the surface morphology and the light-scattering properties of textured surfaces [43,81–84]. In the following, three simulation models for light scattering of textured surfaces will be introduced in details.

**Scalar scattering theory**

In the early model based on the scalar scattering theory [85], the haze for the reflection $H_R$ was given by the following equations:

$$H_R = 1 - \exp\left\{-\left[\frac{4\pi\delta_{rms} n_1 \cos\theta_i}{\lambda}\right]^2\right\} \qquad (2.1)$$

$n_1$ is the refractive index of the incident medium and $\theta_i$ is the incident angle. In this model, the interface morphology was determined only by the rms roughness $\delta_{rms}$ and the height profile of surfaces is assumed to follow a Gaussian distribution whose amplitude defines the rms roughness.

However, a substantial difference between the measured haze and calculated haze with Eq. 2.1 was found for textured $SnO_2$ and $ZnO$ surfaces [43,81,86]. One of the possible reasons for this difference is deviation of the interface morphology from the Gaussian height distribution. To obtain a better approximation of the haze, Krc et al. [81][86] suggested modification of the calculation by introducing a wavelength dependent a fitting factor $C_R(\lambda)$:

$$H_R = 1 - \exp\left\{-\left[\frac{4\pi\delta_{rms} C_R(\lambda) n_1 \cos\theta_i}{\lambda}\right]^2\right\} \qquad (2.2)$$

$C_R(\lambda)$ was determined with a fitting procedure, in which the calculations were matched with the experimental results in air. Using the determined $C_R(\lambda)$, the haze within a-Si:H material were calculated and used for the simulations of the $QE$ of the solar cells. A good agreement between the measurements and simulations of the $QE$ were found for all the investigated solar cells in Ref. [81].

**Grating model**

In the grating model, light scattering is described by diffraction of the light at gratings. The scattering angle $\theta$ can be related to the lateral component of the wave vector $k_x$ with the following equation:

$$k_x = \frac{2\pi n \sin\theta}{\lambda} \qquad (2.3)$$

where $\lambda$ is the wavelength of light and $n$ is the refractive index of the medium. As shown in Figure 2.7, a periodic grating with the grating constant $g$ diffracts the incident light by transferring multiples of a well-defined lateral wave vector $2\pi/g$. If only diffraction into the first order is taken into account, the scattering angle can be calculated by

$$\theta = \arcsin\left(\frac{\lambda}{gn}\right) \qquad (2.4)$$

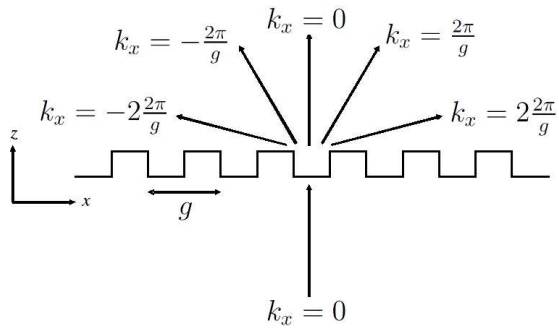


*Figure 2.7 The mechanism of the diffraction at a periodic grating with the lattice constant g. The lateral wave vector components $k_x$ for each diffraction order are given. This graphic was given by Bittkau et al. in Ref.* [87].

A randomly textured surface, such as an etched sputtered *ZnO* surface, was assumed by Bittkau et al. [87][83] to be a superposition of periodic gratings of different grating constants. By applying a fast Fourier transformation (FFT) to the *AFM* topography, the distribution of grating constants $G(k_x,k_y)$ can be extracted. The angular intensity distribution *AID* can be determined by:

$$AID(\theta) = G(k_x, k_y)\frac{2\pi m}{\lambda}\cos\theta \tag{2.5}$$

**Phase model**

Dominé et al [84] proposed the so-called phase model which is based on the Rayleigh-Sommerfeld diffraction integral [88] with some modifications from Harvey et al. [89]. In this model, the local topographic height is described by a height function $h(x, y)$. When the incident light passes a roughness zone, the phase of the light will change. The phase change $\Delta\varphi$ for the transmission of light can be calculated by [84]:

$$\Delta\varphi = \frac{2\pi}{\lambda}(h_{\max} - h_{\min})n_2 + \frac{2\pi}{\lambda}h(x,y)(n_1 - n_2) \tag{2.6}$$

where $n_1$ and $n_2$ are the refractive indices of the media of the indent light and transmitted light, respectively.

For the reflection of light, the phase change $\Delta\varphi$ can be calculated by [90]:

$$\Delta\varphi = \frac{4\pi m}{\lambda}(h_{\max} - h_{\min} - h(x,y)) \tag{2.7}$$

where $n$ is the refractive index of the medium, $h_{max}$ and $h_{min}$ are the largest and smallest height of the topography, respectively.

The scattered light intensity corresponds to the radiance $L$, which is defined as the radiant power per unit solid angle per unit projected source area. This quantity can be calculated by

$$L(k_x, k_y) = \frac{\lambda^2}{A_S} \left| F\left\{ \frac{1}{(1+\varepsilon)^2} \exp(i\Delta\varphi) \right\} \right|^2 \qquad (2.8)$$

where $k_x$ and $k_y$ are the x and y component of the wave vector $k$, respectively, $F\{\ldots\}$ is the Fourier transform and $A_s$ is the area of the surface. $\varepsilon$ is the ratio between the distance from the origin to all points ($x$, $y$) and the observation distance. Since the upper limit for ε is the ratio between the diameter of the light beam and the observation distance, the value of $\varepsilon$ can be neglected. The angular intensity distribution $AID$ can be determined by:

$$AID(\theta) = \sum_{k_x^2+k_y^2=k^2\sin^2\theta} L(k_x, k_y) \frac{2\pi n}{\lambda} \cos\theta \qquad (2.9)$$

In this work, we will compare our experimental results with the prediction of the simulation models introduced above to further understand the physical mechanisms for light scattering. Moreover, the phase model was used to simulate the *AID*s in silicon for both the transmission at the *ZnO/μc-Si:H* interface (as on the front side of solar cells) and for the reflection at the back reflector. By comparing the *AID*s for the transmission to those for the reflection, we will estimate whether the transmission at the *ZnO/μc-Si:H* interface or the reflection at the back reflector is the dominant scattering process regarding the light trapping in solar cells.

# 3. Experimental

This chapter describes the preparation of the solar cells used in this work. Firstly, we introduce the layer arrangement of the *p-i-n* solar cells and two types of the *n-i-p* solar cells with different substrates: glass/etched-*ZnO* and glass/etched-*ZnO/Ag/ZnO* substrates. Then, the preparation of the *n-i-p* solar cells are described in more details, in terms of the substrates, silicon layers and front contacts. The main preparation parameters for the *TCO* and silicon layers are given.

## 3.1 Layer arrangement of *p-i-n* and *n-i-p* solar cells

The solar cells with an n-i-p configuration used in this work were prepared on two different substrates. Figure 3.1 shows the schematic diagram of the *n-i-p μc-Si:H* solar cells on a (a) glass/etched-*ZnO* and (b) glass/etched-*ZnO/Ag/ZnO* substrate. For the investigation of the silicon and front *TCO* layers in the solar cells, the transparent glass/etched-*ZnO* substrates were used. To improve the current density of solar cells and achieve a high efficiency, the high reflective glass/etched-*ZnO/Ag/ZnO* substrates were used by covering the glass/etched-*ZnO* substrates with a 200 nm thick *Ag* and 80 nm thick *ZnO* layer (see Figure 3.1 (b)). The 80 nm *ZnO* layer was used to reduce the plasmonic absorption losses of the *Ag* layer [91,92]. On the both types of substrates, the silicon layers were prepared by *PECVD* with a sequence of *n*-type, *i*- and *p*-type layers. On the p-type layers, the *TCO* (*ZnO)* layers as front contacts were deposited. Finally, *Ag* grids were used on the front-*ZnO* layers to support the carrier collection.

It can be noticed that there are three *ZnO* layers used in one *n-i-p* solar cell on a glass/etched-*ZnO/Ag/ZnO* substrate, at different places and for different functions. As shown in Figure 3.1 (b), the first *ZnO* layer was sputtered on glass and etched after sputtering to achieve textures on the surface. This *ZnO* layer was used to provide a textured surface for the light trapping in solar cells and called in this work "etched-*ZnO*". The second *ZnO* layer was sputtered on the *Ag* layer to enhance the reflection and referred to as "back-*ZnO*" in this work. The third *ZnO* layer was sputtered on the *p*-type silicon layer and used as front contacts in the solar cells. Since this *ZnO* layer was placed on the front (illumination) side of solar cells, it is called "front-*ZnO*" in this work. Due to different functions and requirements, these three *ZnO* layers were deposited at quite different conditions, even in different deposition systems. The

details in terms of the deposition conditions and systems will be described in the following section.

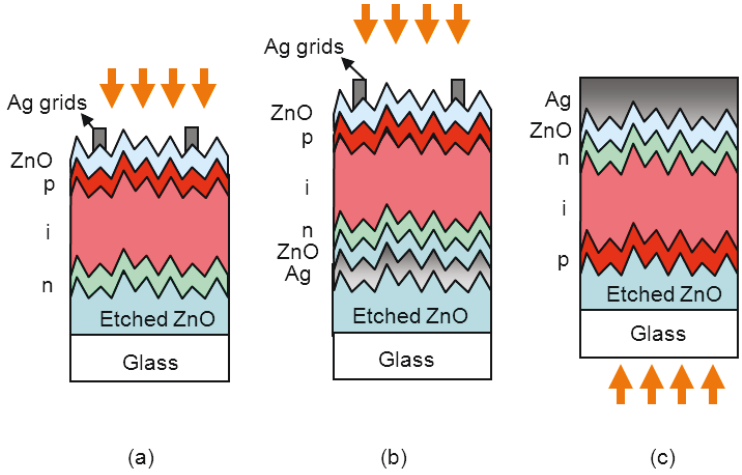


*Figure 3.1 Schematic diagram of (a) an n-i-p µc-Si:H solar cell on glass/etched-ZnO substrate and (b) an n-i-p µc-Si:H solar cell with an glass/etched-ZnO/Ag/ZnO substrate and (c) the standard p-i-n µc-Si:H solar cell.*

Solar cells with a *p-i-n* configuration used in this study have a layer arrangement as shown in Figure 3.1 (c). On a glass substrate, an 800 nm thick *ZnO* layer was sputtered and then textured by etching it in HCl solution. On the etched-ZnO layer, a 20 ~ 30 nm thick *µc-Si:H p-type* layer, ~ 1µm *µc-Si:H i*-layer and an ~ 20 nm thick *µc-Si:H n-type* layer were deposited by *PECVD* sequentially. After the deposition of the silicon layers, an 80 nm *ZnO* and 700 nm *Ag* layers were deposited sequentially.

## 3.2 Preparation of *n-i-p* solar cells

### 3.2.1 Substrate preparation

**Deposition of *ZnO* layers on glass substrates**

The *ZnO* layers were deposited in the "large area sputtering system" (VISS 300) provided by Von Ardenne Anlagentechnik GmbH. This system is a vertical in-line deposition system and operated in a dynamic mode. In the dynamic deposition, the substrate holder moves

continually in front of various targets. A linear planer ceramic $ZnO:Al_2O_3$ (1 wt%) was used as the target for the sputtering. More details about the deposition system have been described in the thesis from Berginski [64], Zhang [93] and Owen [66].

Before depositions, nine 10 x 10 $cm^2$ glass substrates (Eagle XG, Corning) were placed with a 3 x 3 matrix in the 30 x 30 $cm^2$ substrate holder and heated to 300°C (substrate temperature) for at least one hour. After heating, plasma was excited by a RF generator with a frequency of 13.56 MHz and power of 1500 W. During the deposition, the pressure and argon gas flow were kept constant at 1 µbar and 100 sccm, respectively. These deposition conditions were optimized for the front contact in *p-i-n* solar cells [94].

**Texturing of *ZnO* layers**

The sputtered *ZnO* layers were textured by etching them in *HCl* solution with a concentration of 0.5 w/w% at room temperature. These etching conditions have been optimized for p-i-n solar cells [11,56]. The etching time was varied from 10 s to 100 s, to achieve different textures on the surfaces.

**Deposition of *Ag* and back-*ZnO* layers on glass/etched-*ZnO* substrates**

An around 200 nm *Ag* and 80 nm *ZnO* layer were deposited sequentially on glass/etched-*ZnO* substrates as back reflectors. The depositions were carried out in the "large area sputtering system" (described above) at room temperature. For both depositions, the pressure was 5.6 µbar and the excitation power was 1500 W. For the deposition of Ag layers, only argon was used with the gas flow of 200 sccm. For the deposition of *ZnO* layers, argon and oxygen were used with the gas flow of 100 sccm and oxygen concentration of 0.5%.

## 3.2.2 Silicon deposition

All the silicon layers in this work were deposited in the 6-chamber *PECVD* system manufactured by MRG Inc., Denver. In this system, there are 6 chambers connected by two transfer locks and one load locks. Intrinsic layers, *n-* and *p-type* were deposited on different chambers to avoid contamination and residual doping effects. Moreover, to improve the reproducibility of the process, the *µc-Si:H* and *a-Si:H* intrinsic layers were deposited in separate chambers. More details about the 6-chamber *PECVD* system were given in [27]. In

the following, we only describe the main parameters of the silicon layers in *n-i-p* solar cells prepared in this work.

The main deposition parameters of the silicon layers in the *μc-Si:H n-i-p* solar cells are summarized in Table 3.1. All the silicon layers were deposited at a substrate temperature $T_S$ of 185 °C. Firstly, the around 20 nm thick *n*-type *μc-Si:H* layers were deposited on the substrates by using $PH_3$, $SiH_4$ and $H_2$ gases. The plasma for the deposition was excited by a power of 25 W and frequency of 13.56 MHz under a pressure of 4 mbar.

After the deposition of the *n-type μc-Si:H* layers, samples were moved to another chamber where the intrinsic *μc-Si:H* layers (*i*-layers) were deposited with $SiH_4$ and $H_2$ gases. The silane concentration *SC* which is defined by the gas flow ratio of silane to hydrogen and silane ($SC = [SiH_4]/([SiH_4]+[H_2])$). To investigate its effects on the cell performance, the *SC* of *i*-layers was changed from 4% to 6% in this work. Since the deposition rate increases with the *SC* [7], the deposition time of *i*-layers was varied dependent on the *SC* to keep the *i*-layer thickness constant (around 1μm). The plasma for the deposition was excited by a very high frequency of 94.7 MHz and power of 20 W under a pressure of 1.5 mbar.

After the deposition of *i*-layers, samples were moved to the chamber where the *p-type* layers were deposited with trimethylboron *TMB*, $SiH_4$ and $H_2$ gases. The *TMB* concentration is defined by the ratio of trimethylboron to silane gas flows ($C_{TMB} = [TMB]/[SiH_4]$). To investigate the effects of the doping ratio of *p-type* layers on the cell performance (presented in Section 5.1.5), the $C_{TMB}$ was varied from 0.5% to 2.5%. For excitation of the plasma for the deposition, a very high frequency of 94.7 MHz, a power of 10 W and a pressure of 0.4 mbar were used. The thickness of the *p-type* layers was varied from 20 nm to 100 nm by changing the deposition time from 2 minutes to 20 minutes.

| | **Gas flow [sccm]** | | | | **$T_S$ [°C]** | **Pressure [mbar]** | **Power [W]** | **Frequency [MHz]** |
|---|---|---|---|---|---|---|---|---|
| | $SiH_4$ | $H_2$ | 2% $PH_3$ in $SiH_4$ | 1% *TMB* in *He* | | | | |
| n | | 200 | 1 | - | 185 | 4 | 25 | 13.56 |
| i | 4~6 | 95 | - | - | 185 | 1.5 | 20 | 94.7 |
| p | 2 | 200 | - | 1~5 | 185 | 0.4 | 10 | 94.7 |

*Table 3.1 Deposition parameters of silicon layers in μc-Si:H n-i-p solar cells.*

### 3.2.3 Front contact deposition

On the *p-type* layers, the front contacts (front-*ZnO*) layers were deposited in the "small area sputtering system" provided by Kurt J. Lesker Company [63,64,66]. This system is a static deposition system and contains a load chamber and a process chamber. In the process chamber, there are four places for different targets with a diameter of 15.24 cm (6 inches). For each deposition, one 10x10 $cm^2$ sample was loaded on one of four substrate holders and placed 10 cm above the selected target. Before a deposition, the sample was heated for 30 minutes and the target was presputtered for 5 minutes by closing a movable shutter between the target and substrate.

To avoid possible damages of the underlying silicon layers, a heater temperature below 260° is required for front-*ZnO* layers. In order to achieve a high conductive and thin front-*ZnO* layer even at a low substrate temperature, we used in this work a *ZnO* target with a higher $Al_2O_3$ concentration of 2 wt% instead of the target with 1 wt% $Al_2O_3$ for the front-*ZnO* layers in *p-i-n* solar cells. 150°C was used as the heater temperature. Plasma was excited by a RF generator with a frequency of 13.56 MHz and power of 250 W. The pressure and argon flow during the deposition were 2 mTorr and 8 sccm, respectively. No oxygen gas was used for the sputtering.

## 3.3 Preparation of *p-i-n* solar cells

Several microcrystalline silicon *p-i-n* solar cells were also prepared in this work as references to the *n-i-p* solar cells. Firstly, the ZnO layers were deposited on the glass substrates in the so-called "large area sputtering system" (see Section 3.2.1) and etched in *HCl* solution for 40 s. The deposition and etching conditions of the *ZnO* layers were as same as for the substrates in the *n-i-p* solar cells described in the previous section (Section 3.2.1).

Glass/etched-*ZnO* substrates were loaded into the "6-chamber *PECVD* system" to deposit silicon layers. To grow a highly crystalline *μc-Si:H p*-type layer on *ZnO*, a seed *p*-type layer was firstly deposited with low $SiH_4$ and *TMB* flows for 3 minutes. The second *μc-Si:H p*-type, intrinsic and *n*-type layers were deposited at the same conditions as for the *n-i-p* solar cells (described in Section 3.2.2). The main deposition parameters of the silicon layers in *p-i-n* solar cells are summarized in Table 3.2.

| | Gas flow [sccm] | | | | $T_s$ [°C] | Pressure [mbar] | Power [W] | Frequency [MHz] |
|---|---|---|---|---|---|---|---|---|
| | $SiH_4$ | $H_2$ | 2% $PH_3$ in $SiH_4$ | 1% *TMB* in *He* | | | | |
| p-seed | 1.5 | 200 | - | 0.4 | 185 | 0.4 | 10 | 94.7 |
| p | 2 | 200 | - | 2 | 185 | 0.4 | 10 | 94.7 |
| i | 4.5 | 95 | - | - | 185 | 1.5 | 20 | 94.7 |
| n | | 200 | 1 | - | 185 | 4 | 25 | 13.56 |

*Table 3.2 Deposition parameters of silicon layers in µc-Si:H p-i-n solar cells.*

After deposition of the silicon layers, the samples were moved again into the "large area sputtering system" to grow an around 80 nm back-*ZnO* layer. The deposition conditions of the back-*ZnO* layers in the *p-i-n* solar cells were as same as in the *n-i-p* solar cells as described in Section 3.2.1. On these back-*ZnO* layers, the round 700 nm *Ag* layers as back reflectors were thermally evaporated by an in-house made setup.

# 4. Characterization methods

This chapter presents the methods used in this work to characterize structural and electrical properties of thin film silicon, the surface morphology of etched ZnO layers, the optical properties of thin films or solar cells and the performance of solar cells.

## 4.1 Structural and electrical properties of thin film silicon

### 4.1.1 Raman spectroscopy

Raman spectroscopy is a method to determine the structural properties of thin film silicon material [34,95]. Raman effect is the inelastic scattering of the incident photons by interaction with phonons in the material. During the inelastic scattering, the frequency of the incident photons shifts to higher or lower values, depending on whether phonons are absorbed or emitted, respectively. The spectrum of the Raman-scattered light depends on the chemical bonds and structural symmetry of materials and can be used for material identification and analysis. In particular for *μc-Si:H*, it can be used to estimate the crystalline volume fraction.

The *c-Si* spectrum has a prominent peak at 520 $cm^{-1}$, while the *a-Si:H* spectrum exhibits a broad hump at 480 $cm^{-1}$. The broad hump of the *a-Si:H* spectrum results from the absence of long range translation symmetry in the material. Microcrystalline silicon *μc-Si:H* consists of crystallites and amorphous tissue, as described in Section 2.1. Therefore, the *μc-Si:H* spectrum shows a crystalline and amorphous peaks simultaneously. Figure 4.1 shows the measured Raman spectra for the standard *a-Si:H* (red line) and a *μc-Si:H* sample (black line). Fitting the *μc-Si:H* spectrum with the Raman spectrum of the standard *a-Si:H*, the rest of the signal is regarded to be the crystalline silicon phase as shown with the blue line in Figure 4.1. A semi-quantitative value of the crystalline volume fraction (crystallinity) $I_{CRS}$ is calculated by:

$$I_{CRS} = \frac{I_{\mu c-Si:H} - I_{a-Si:H}}{I_{\mu c-Si:H}} \tag{4.1}$$

where $I_{\mu c\text{-}Si:H}$ and $I_{a\text{-}Si:H}$ are the integration of the area under the measured Raman spectra of *μc-Si:H* and the standard *a-Si:H*, respectively.

In this work, for the investigation of *p*-type *μc-Si:H* material, around 40 nm thick single layers were deposited on glass substrates (Corning 1737) and measured by the laser at a

wavelength of 415 nm. For the investigation of the intrinsic layers in solar cells, the solar cells without front-*ZnO* layers were measured by a laser at a wavelength of 647 nm. With this wavelength, the Raman signal is dominated by the intrinsic layers in solar cells.

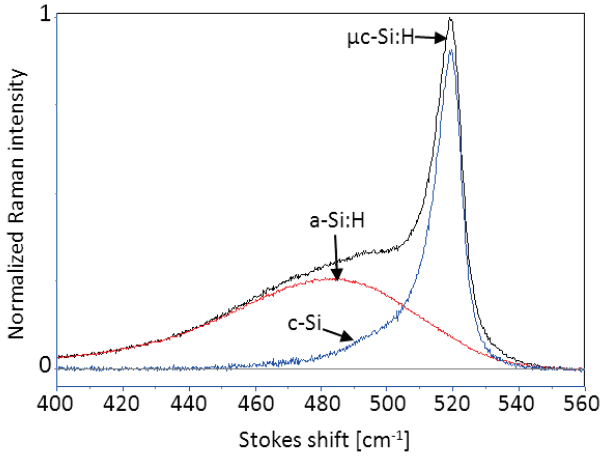


*Figure 4.1 Measured Raman spectra for the standard a-Si:H (red line) and a µc-Si:H sample (black line). Fitting the µc-Si:H Raman spectrum with the Raman spectrum of the standard a-Si:H, the rest of the signal is regarded to be the crystalline silicon phase (blue line).*

## 4.1.2 Electrical conductivity

To measure the electrical conductivity of thin film silicon, single layers were deposited on glass substrates. On the top of the single layers, two coplanar silver contacts were deposited by thermal evaporation. The width of the contacts is 5 mm and the gap between the contacts is 0.5 mm. The current $I$ at the applied voltage $V$ were measured at room temperature in vacuum after two hours annealing at 170°C. The dark conductivity $\sigma_{dark}$ was calculated by:

$$\sigma_{dark} = \frac{Il}{Vwd} \tag{4.2}$$

where $l$ is the gap between the contacts, $w$ is the width of the contacts and $d$ is the thickness of the investigated layer.

## 4.2 Surface morphology

### 4.2.1 Atomic Force Microscopy *AFM* measurement

Since its invention in 1986 [96], Atomic Force Microscopy *AFM* is intensively used for high resolution mapping of the surface topography. An *AFM* consists of a cantilever with a sharp tip at the end, a laser source and a photodiode. The tip is scanned across a surface using piezoelectric elements. When the tip is brought into proximity of a sample surface, forces between the tip and the sample lead to a deflection of the cantilever. The deflection is measured using the laser beam reflected from the cantilever into the photodiode. There are two typical imaging modes for *AFM*, contact and non-contact mode. In non-contact mode as used in this work, the tip of the cantilever does not contact the sample surface. The cantilever is oscillated at a frequency slightly above its resonant frequency and with amplitudes of a few nanometres. The oscillation amplitude and frequency are kept constant by adjusting the tip-to-sample distance. The tip-to-sample distance is measured at each (*x,y*) data point and used to construct a topographic image of the sample surface by using a scanning software. In this work, *ZnO* surfaces were measured with an *AFM* Nanostation 300, SIS.

### 4.2.2 Statistical analyses of the zinc oxide surface morphology

With the *AFM* images, statistical evaluations of the *ZnO* surface morphology were performed, in terms of the rms roughness $\delta_{rms}$, the size of surface features (craters) and the surface angular distribution. The same area of 7x7 $\mu m^2$ were used for all the *ZnO* surfaces in this work.

**i. rms roughness**

The rms roughness $\delta_{\mathrm{rms}}$ is the mostly used parameter to describe a rough surface. It is defined as the standard deviation of the *z*-values for a given *AFM* image. For an *AFM* image containing *M* and *N* data points in the *x* and *y* directions, the rms roughness is given as:

$$\delta_{rms} = \sqrt{\frac{1}{MN}\sum_{k=0}^{M-1}\sum_{l=0}^{N-1}\left[z\left(x_k, x_l\right)\right]^2} \tag{4.3}$$

where *z* is the height at a given *x* and *y* coordinate, *k* and *l* are for the indexing purposes.

**ii. Evaluation of craters on etched-*ZnO* surfaces**

In this work, sputtered *ZnO* layers were etched for different time to obtain different surface morphologies. Figure 4.2 shows exemplarily the 3D *AFM* images of three *ZnO* surfaces after etching for (a) 10 s, (b) 40 s and (c) 85 s. Craters with different sizes can be seen on all the surfaces.

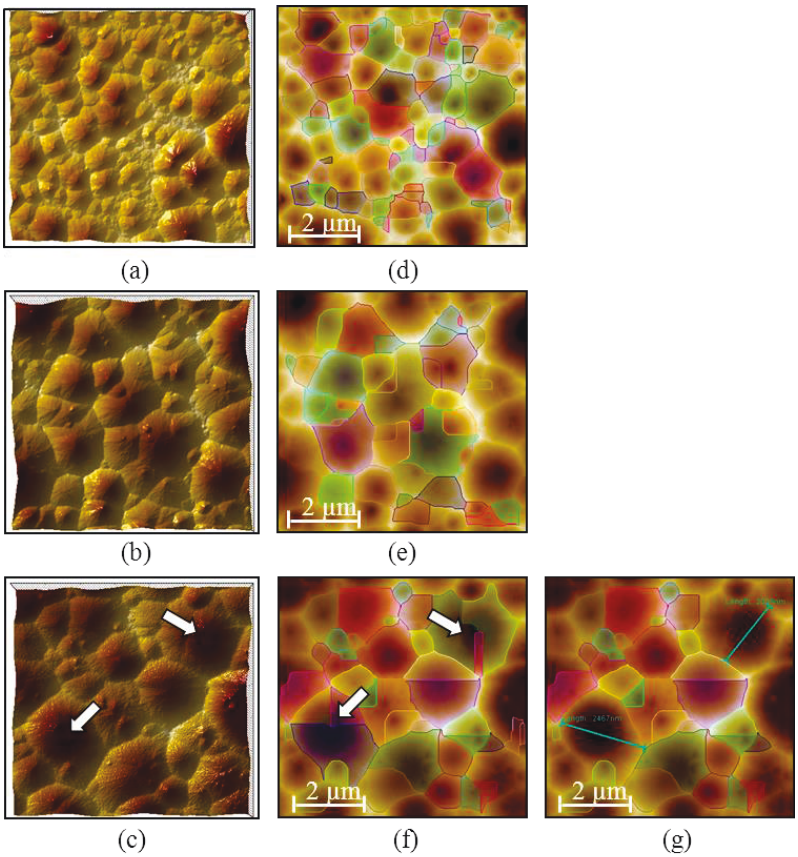


*Figure 4.2 3D AFM images of three ZnO surfaces prepared with 800 nm thick ZnO layers etched for (a) 10 s, (b) 40 s and (c) 85 s and the AFM images with craters segregated by the watershed algorithm for these surfaces in (d), (e) and (f), respectively. Figure (g) shows the AFM image of the identical surface like in (c) with craters segregated by the watershed algorithm and the manual estimation of two crater diameters using the software SPIP™. The meaning of the white arrows and blue lines is explained in the text.*

The craters on the etched-*ZnO* surfaces were quantitatively evaluated in this work by using software "Scanning Probe Image Processor™ (SPIP™)" (http://www.imagemet.com/), in terms of the crater diameter, depth and angle. Figure 4.3 shows the schematic profile of a crater, illustrating the definitions of the crater diameter *d*, crater depth *h* and crater angle *α*. The diameter *d* and depth *h* is defined by the maximal lateral and vertical distance between 2 measurement points on the crater, while the crater angle is defined by the angle between the crater wall and the substrate.

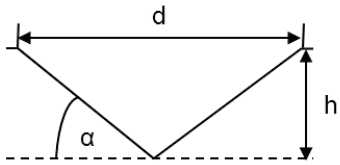


*Figure 4.3 Schematic profile of a crater, illustrating the definition of the crater diameter d, crater depth h and crater angle α.*

**Segment of craters in an AFM image**

To quantitatively evaluate the crater diameter and depth, the watershed algorithm in the software SPIP™ was used to segregate the craters in an *AFM* image. The idea of the watershed algorithm was introduced in 1979 by Beucher and Lantuéjoul in Ref. [97]. A water source is placed in each regional minimum and the pores are filled with water. A watershed boundary is build when different sources of water are meeting. With this method, an *AFM* image is divided into a set of basins. The segment with the watershed algorithm can be influenced by the threshold, the so-called "smoothing filter size" in the software SPIP™. A too small threshold may lead to an over segment of craters on a surface. To compare the crater sizes on different surfaces, a constant threshold of 250 nm was used for all the surfaces investigated in this work. Moreover, the craters on the boarders of the AFM images were not included into the evaluation to avoid a under estimation of the crater sizes.

As examples, Figure 4.2 (d), (e) and (f) show the *AFM* images with the craters segregated by the watershed algorithm, for the *ZnO* surfaces whose 3D *AFM* images are shown in Figure 4.2 (a), (b) and (c), respectively. The distinguished craters are marked with different colors in the *AFM* images (d, e and f). It is noticed that most of the craters which can be distinguished by eyes in the 3D *AFM* images are also distinguished well by using the watershed algorithm. In addition, the diameter and depth of the segregated craters can be calculated by the software

SPIP™. Only for several craters with quite large "flat bottoms", more craters are segregated by the watershed algorithm than what one can see by eyes, as shown with white arrows in Figure 4.2 (c) and (f). For this kind of craters, the diameter was determined manually by using "Draw line measurement" function in the software SPIP™, as shown with the blue lines in Figure 4.2 (g), while the depth was determined manually in the profile of *AFM* images.

**Mean diameter and depth of craters**

The mean diameter $d_{mean}$ or depth $h_{mean}$ of the craters on a surface were calculated with the sum of the diameters or depths of all the craters divided by the total number of the craters. With the mean diameter and depth, we can investigate the general variation trend of craters on the surfaces with the preparation conditions.

**Distribution of crater diameters and depths**

Since the craters on one *ZnO* surface have quite different diameter and depth (see Figure 4.2), more detailed analysis was done by calculating the distribution of the crater diameters and depths. For each surface, 10 *AFM* images (7x7 $\mu m^2$) were used to have a large amount of craters for these calculations.

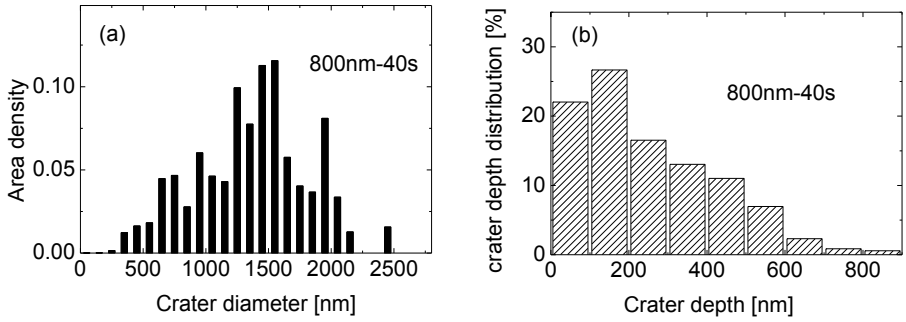


*Figure 4.4 The distribution of (a) crater diameters and (b) crater depths, for the surface prepared with 800 nm thick ZnO layers etched for 40 s.*

The distribution of the crater diameters is calculated by the area density of the craters with the diameters in a given range. The area density of these craters is defined by the ratio of

the area covered by the craters to the total area of all the craters. The distribution of crater depths is calculated by the ratio of the number of the craters with given depths to the total crater number. As an example, Figure 4.4 shows the distribution of crater diameters and depths for the surface prepared with an 800 nm thick *ZnO* layer etched for 40 s. Broad distributions can be seen for both crater diameters and depths. The maxima of crater diameter and depth distributions are located at 1500 ~ 1600 nm and 100 ~ 200 nm, respectively.

**Crater angle**

The surface angular distribution can be determined by the software SPIP™. The surface angle is defined as the angle between the plane of three neighbouring measured points and the substrate surface. Figure 4.5 shows the surface angular distribution of the surface prepared with an 800 nm thick *ZnO* layer etched for 40 s as an example. The angle at the peak of a surface angle distribution indicates the angle between the wall of most of the craters on the surface and the glass substrate, which is defined as the crater angle $\alpha$ (see Figure 4.3). Thus, the surface angular distribution in Figure 4.5 indicates that most of the craters on this surface have a crater angle of around 25°.

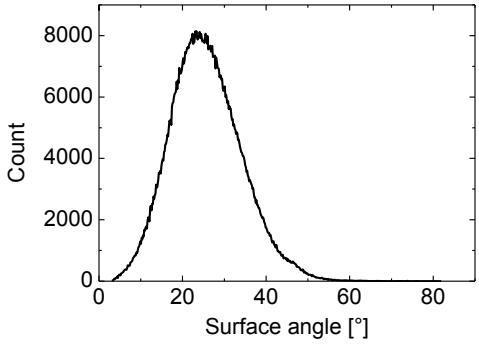


*Figure 4.5 The surface angular distribution of the surface prepared with 800 nm thick ZnO layers etched for 40 s.*

## 4.3 Optical properties

### 4.3.1 Transmission and reflection

A spectrophotometer is a photometer which can measure the light intensity as a function of the wavelength. In this work, a high performance spectrophotometer, PerkinElmer Lambda 950, was used to determine the optical properties, such as the transmission and reflection of *TCO* layers, etched-*ZnO*/*Ag* reflectors and solar cells. Using a double monochromator in this equipment, a specific wavelength is selected from the light sources emitted by a tungsten and deuterium lamp. The light intensity is measured by the detectors located in the inner wall of an integrating sphere, which allows for measurements of the total and diffuse transmission or reflectance.

With the total transmission $T_{\text{total}}$ and reflectance $R_{\text{total}}$ measured by the spectrophotometer, the absorptance $A$ of samples can be calculated by:

$$A = 1 - T_{total} - R_{total} \tag{4.4}$$

The haze is often used to characterize light scattering properties of textured samples. The haze for the reflection is defined by the ratio between the diffuse and total reflectance:

$$H_R = \frac{R_{diffuse}}{R_{total}} \tag{4.5}$$

### 4.3.2 Angular intensity distribution *AID*

The angular intensity distribution *AID* of the etched-*ZnO/Ag* reflectors was measured using an in-house made angular resolved scattering system. Figure 4.6 shows the schematic diagram of this system. A laser beam with a wavelength of 550 nm passes through a filter, chopper and aperture plate and is scattered by the sample. The intensity of scattered light is determined by a photo diode which can rotate around the sample in a plane with a step of 1°. For the reflection, the measurement was performed from 10° to 90°. The reflected light at the angles from 0 to 10° cannot be measured, because the laser beam has to pass through from this place (see Figure 4.6).

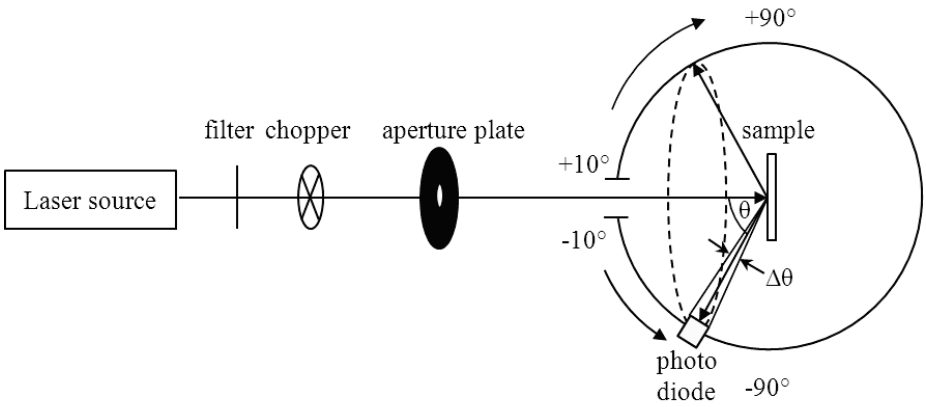


*Figure 4.6 Schematic diagram of the angular resolved scattering system.*

The voltage $V_s$ measured by the photo diode at each angle is assumed to be proportional to the light intensity. The light intensity is represented by the ratio between the $V_s$ and $V_0$ which is the reference voltage measured without samples at 0°. Since the measurement is performed in a plane, to determine the intensity in the whole light scattering cone, the measured data ($V_s/V_0$) has to be integrated over all the azimuthal angles. When the scattering angle $\theta$ is defined as the angle between the incident and scattered light, the angular intensity distribution $AID(\theta)$ for the reflection can be represented by:

$$AID(\theta) = \frac{V_s(\theta)}{V_0 a_{diode}} \int_0^{2\pi} \int_{\theta-\frac{\Delta\theta}{2}}^{\theta+\frac{\Delta\theta}{2}} R^2 \sin(\theta) d\phi d\theta \tag{4.6}$$

$$= \frac{2\pi V_s(\theta) R^2 \left[ \cos(\theta - \frac{\Delta\theta}{2}) - \cos(\theta + \frac{\Delta\theta}{2}) \right]}{V_0 a_{diode}} \tag{4.7}$$

where $R$ is the distance between the diode and the sample, $a_{\text{diode}}$ is the area of the diode and $\Delta\theta$ is the resolution of the system, which is defined by the area of the photo diode and the step of the photo diode rotating around the plane and equal to 1° for our system.

## 4.4 Solar cell performance

### 4.4.1 Current-voltage measurement

The current-voltage measurement (*I-V* measurement) is the most commonly used method to evaluate solar cells and has been described in details in Ref. [98,99]. In this work, all *I-V* measurements were performed with a so-called Class A simulator (type WACOM-WXS-140S-Super). An AM1.5 spectrum with an irradiance of 100 mW/cm$^2$ was created by this simulator and calibrated with a Hamamatsu photodiode S1336-BQ before measurements. During measurements, the temperature of solar cells was controlled at 25 ± 1°C.

All the *p-i-n* solar cells on one substrate can be contacted at the same time and measurements are controlled by a software program written in-house. For the *n-i-p* solar cells on a substrate, only one cell could be connected each time. In addition, for *n-i-p* solar cells, the region outside of the active cell area had to be covered by a mask to avoid undesired current collection. The square holes in the mask have edge lengths of 9 mm resulting in an illumination area of 81 mm$^2$. Moreover, light cannot penetrate through the *Ag* grids on top of the front-ZnO layers (see Figure 3.1). Therefore, for the calculation of the current density, an effective cell area of 69.6 mm$^2$ was used by subtracting the *Ag* grid area (around 11.4 mm$^2$) from the illumination area (81 mm$^2$).

From the *I-V* measurements, the short circuit current density $J_{SC,}$ the open circuit voltage $V_{OC}$, the fill factor *FF* and the efficiency $\eta$ of solar cells can be determined. The short circuit current density $J_{SC}$ and open circuit voltage $V_{OC}$ are the maximum current density and voltage generated by the solar cell, respectively. In the ideal case, $J_{SC}$ equals the photo-generated current density $J_{ph}$, since there is no contribution from the dark current under the condition of short circuit ($V = 0$).

Under the condition of open external circuit ($j = 0$), the so-called open circuit voltage $V_{OC}$ is build up and results in a compensation of the photo-generated current density by the dark current density $j_{dark}(V_{OC})$. Thus, $V_{OC}$ can be deduced as [98]:

$$V_{OC} = \frac{nkT}{e} \ln\left(\frac{J_{SC}}{j_0} + 1\right) \tag{4.8}$$

where $n$ the diode ideality factor, $k$ the Boltzmann constant, $T$ the temperature, $e$ the elementary charge and $j_0$ the saturation current density. The saturation current density $j_0$ depends on the energy band structure of solar cells and type of recombination mechanisms.

Assuming that all recombination processes are thermally activated, the saturation current density $j_0$ can be given by [100]:

$$j_0 = j_{00} \exp\left(-\frac{E_a}{nkT}\right) \tag{4.9}$$

where $j_{00}$ is the weakly temperature-dependent reference current density and $E_a$ is the activation energy which equals to the energy band gap $E_g$ for the recombination in bulk and space-charge zone [100]. Thus, the open circuit voltage $V_{OC}$ can be also described by:

$$V_{OC} = \frac{E_a}{e} - \frac{nkT}{e} \ln\left(\frac{j_{00}}{J_{SC}}\right) \tag{4.10}$$

The cell efficiency $\eta$ is determined by the ratio of the maximum generated power and the incident radiation power. $J_{max}$ and $V_{max}$ are defined as the current density and voltage at the maximum generated power point, respectively. The fill factor *FF* is an integral measure of the collection efficiency at the maximum power point and defined as:

$$FF = \frac{J_{max} V_{max}}{J_{SC} V_{OC}} \tag{4.11}$$

## 4.4.2 Quantum efficiency measurement

The quantum efficiency measurement provides information about the optical properties and charge carrier extraction mechanism of solar cells [98,99,101]. The quantum efficiency $QE(\lambda)$ is defined as:

$$QE(\lambda) = \frac{j_{ph}(\lambda, V)}{e\Phi(\lambda)} \tag{4.12}$$

where $j_{ph}(\lambda, V)$ is the photo-generated current collected at the electrodes and $\Phi(\lambda)$ the incident light quanta per wavelength interval. Therefore, the quantum efficiency can be interpreted as probability for a single light quantum to generate a free charge carrier pair, which then contributes to the current density.

The quantum efficiency of the solar cells in this work was measured with an in-house made differential spectral response *DSR* setup. Using a xenon lamp and a monochromator, a monochromatic light beam is generated with wavelength between 300 and 1300 nm.

# 5. Microcrystalline silicon *n-i-p* solar cells

In our institute (IEK5-Photovoltaik, Forschungszentrum Jülich), microcrystalline silicon *µc-Si:H* solar cells in an n-i-p configuration have been prepared by Vetterl [27] and Klein [102] around 10 years ago. However, *n-i-p* solar cells were not a focus of our institute, while *p-i-n* solar cells were intensively developed [7,36,94,102–106]. In this work, the optimized processes for *µc-Si:H p-i-n* solar cells were transferred to *µc-Si:H n-i-p* solar cells. The aim is to achieve reproducible processes and high enough cell performance as a base for the study of the light scattering and trapping in solar cells.

For all the *µc-Si:H n-i-p* solar cells in this work, a highly crystalline *n*-type layer optimized for tandem *p-i-n* solar cells in the past [104,107] was used. *p-type* layers as window layers and i-layers as absorber layers were optimized based on the optimized processes for *µc-Si:H p-i-n* solar cells. The effects of the *p-type* layer thickness, p-type layer doping ratio and i-layer silane concentration on the performance of the *n-i-p* solar cells were investigated and will be presented in this chapter.

In addition, the optimized deposition conditions of front contacts (*ZnO*) for *p-i-n* solar cells [94] do not fit to *n-i-p* solar cells, since the substrate temperature (~300°C) is too high for the underlying silicon layers. In this work, *ZnO* layers deposited at a low substrate temperature of ~ 100 °C were used as front contacts in the *n-i-p* solar cells. The effects of the front contact thickness on the cell performance will be present and related to the optical and electical properties of the *ZnO* layers and the anti-reflection effect.

Moreover, two types of substrates (glass/etched-*ZnO* and glass/etched-*ZnO/Ag/ZnO*) were used in the *µc-Si:H n-i-p* solar cells. The effects of a highly reflective *Ag/ZnO* back reflector on the cell performance will be shown.

## 5.1 Window layers

Window layers (*p*-type and front *ZnO* layers) with high conductivity and optical transmission are of great importance to achieve high solar cell performance and provide a base for the study of light trapping. In this work, the deposition conditions and thickness of window layers were optimized (also published in [108]). The effects of the thickness and doping ratio of *p*-type layers and the thickness of front contact layers will be present in the following.

## 5.1.1 *P*-type layer

**Effects of *p*-type layers thickness**

To examine the effects of the *p-type* layer thickness, *µc-Si:H n-i-p* solar cells were prepared on glass/etched-*ZnO* substrates with varied deposition time of *p*-type layers from 4 to 18 minutes. The deposition conditions of front *TCO*s (*ZnO* layers) and silicon layers were kept constant. Quite thick (155 nm) *ZnO* layers were used as front *TCO*s in this series of solar cells to ensure that their conductivity is enough for the carrier collection. For comparison, a *µc-Si:H p-i-n* solar cell was prepared with the same deposition conditions of the *µc-Si:H i*- and *n*-layers as in the *n-i-p* solar cells and the optimized condition of *p-type* layers for *µc-Si:H p-i-n* solar cells [103]. This optimized *p-type* layer in the *p-i-n* solar cell was deposited for 4 minutes with a *TMB* concentration $C_{TMB}$ of 1%.

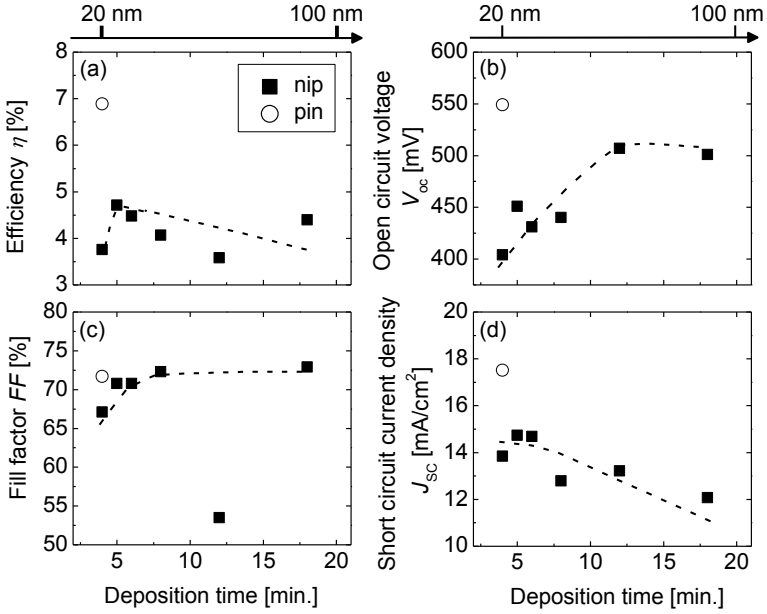


*Figure 5.1 (a) The efficiency η, (b) open circuit voltage $V_{OC}$, (c) fill factor FF and (d) short circuit current density $J_{SC}$ of the solar cells as a function of the deposition time of the p-type layers. The p-type layer thickness with the deposition time was estimated with a constant deposition rate of 0.8 Å/s and is indicated by the arrows. The dashed lines are to guide the eyes.*

As shown with the red points in Figure 5.1, the p-i-n solar cell has a high $V_{OC}$ of around 550 mV, *FF* of 71%, $J_{SC}$ of 17.5 mA/cm$^2$ and $\eta$ of around 7%. In contrast, with the same deposition conditions of silicon layers, the n-i-p solar cell has overall worse performance: an around 150 mV lower $V_{OC}$, 4% lower *FF*, 3.5 mA/cm$^2$ lower $J_{SC}$ and 3.2% lower $\eta$. Note that the lower $J_{SC}$ in the n-i-p solar cell can result from the transparent substrate (*ZnO*/Glass). Therefore, the largest reduction in the cell performance in the case of *n-i-p* cell is observed in $V_{OC.}$ The differences in $V_{OC}$ and *FF* between these two solar cells might result from: (1) different p-type layer properties, since they grow on different materials (on the *ZnO* substrate in the p-i-n solar cell and on the *μc-Si:H i*-layer in the *n-i-p* solar cell); (2) damages of the p-type layer in the n-i-p solar cell by the sputtering process of the front *TCO* layers.

The low open circuit voltage and fill factor in the *n-i-p* solar cell can be improved by increasing the *p-type* layer thickness (deposition time), as shown with the black points in Figure 5.1. $V_{OC}$ increases significantly from 400 mV up to around 510 mV when the *p-type* layer thickness increases from 20 nm to 60 nm. *FF* is improved from 67% up to 73% by increasing the p-type layer thickness. However, the values of the short circuit current density decreases with the *p-type* layer thickness, due to an increase in the parasitic absorption of *p-type* layers. The short circuit current density drops down to 12 mA/cm$^2$ for the *p-type* layer with a thickness of around 90 nm (deposition time = 18 min.).

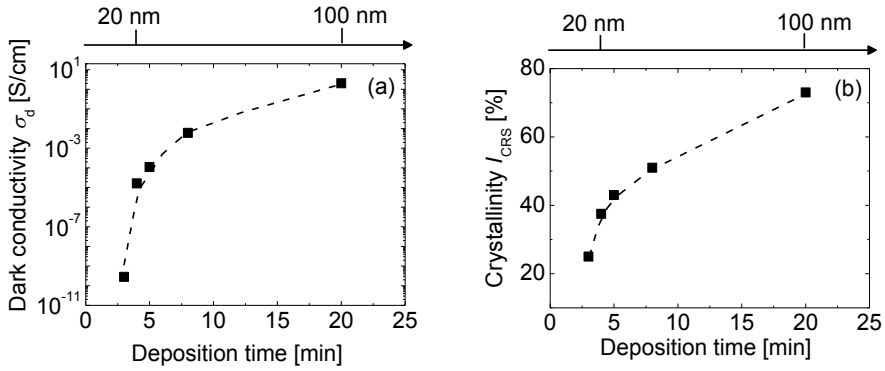


*Figure 5.2 (a) The dark conductivity and (b) crystallinity of the p-type layers deposited on the glass substrates versus the deposition time. The thickness with the deposition time was estimated with a constant deposition rate of 0.8 Å/s and is indicated by the arrows. The dashed lines are to guide the eyes.*

To understand the effects of the p-type layer thickness on the solar cell performance, the changes in the properties of *p-type* layers with the deposition time were investigated. Single *p-type* layers were deposited on glass substrates with varied deposition time from 4 minutes to 20 minutes. The dark conductivity $\sigma_d$ and the crystallinity $I_{CRS}$ of the *p*-type layers were measured and are shown as a function of the deposition time in Figure 5.2 shows (a) and (b), respectively. It is seen that both $\sigma_d$ and $I_{CRS}$ increase with the deposition time. For the 20 nm thick layer, $\sigma_d$ is around $10^{-5}$ S/cm and reaches the value of 3 S/cm for the thickest layer studied here (~ 100 nm, 20 minutes deposition time). It is known that the properties of *μc-Si:H* films prepared by *PECVD* are thickness dependent and the microstructure changes significantly with the deposition time [32,109,110]. The general trend observed in Figure 5.2, namely, an increase in $\sigma_d$ and $I_{CRS}$ with the film thickness, is largely consistent with previous reports [111,112].

The low open circuit voltage and fill factor of the *μc-Si:H n-i-p* solar cell can be improved significantly by increasing the p-type layer thickness, which may be related to the change in the conductivity of *p-type* layers. However, the short circuit current density of the solar cells is reduced with increasing the *p-type* layer thickness. Another possibility to change the *p-type* layer conductivity is varying the doping ratio. In the following, the effects of the doping ratio of *p-type* layers on the solar cell performance will be present.

**Effects of p-type layers doping ratio**

A series of solar cells were prepared on glass/etched-*ZnO* substrates with varied *TMB* concentrations $C_{TMB}$ of *p*-type layers. All the *p*-type layers were deposited for 4 minutes. Figure 5.3 shows the solar cell performance with varied *TMB* concentrations of *p*-type layers. A significant increase in the open circuit voltage (from 350 mV to 525 mV) is observed with an increase in $C_{TMB}$ from 0.5% up to 1.5%. A further increase in $C_{TMB}$ above 1.5% does not result in a $V_{OC}$ improvement. The fill factor increases from around 67% up to 74% with increasing $C_{TMB}$. The short circuit current density rises with the doping ratio for $C_{TMB} < 1.5\%$ and decrease for $C_{TMB} > 1.5\%$. For this series of solar cells, the maximum in conversion efficiency of 5.8% is obtained when the p-type layer is prepared at $C_{TMB} = 1.5\%$.

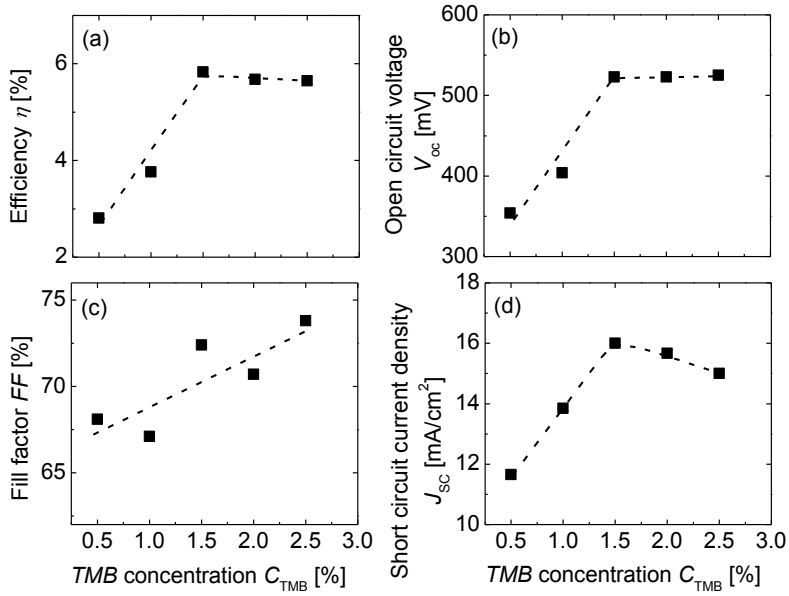


*Figure 5.3 (a) The efficiency η, (b) open circuit voltage $V_{OC}$, (c) fill factor FF and (d) short circuit current density $J_{SC}$ of the solar cells as a function of the TMB concentration $C_{TMB}$ in the p-type layers. The p-type layers in these solar cells are deposited for the same time of 4 minutes. The dashed lines are to guide the eyes.*

To investigate the changes in the properties of *p-type* layers with $C_{TMB}$, single *p-type* layers were prepared on glass substrates with varied $C_{TMB}$. Figure 5.4 shows the effects of $C_{TMB}$ on the properties of *p-type* layers: (a) the crystallinity $I_{CRS}$, (b) the dark conductivity $\sigma_d$, (c) the thickness and (d) the deposition rate. To improve the thickness measurement accuracy, all the *p-type* layers were prepared for a deposition time of 8 minutes, twice thicker than used in the solar cells shown above.

In Figure 5.4 (a), one can see a decrease in the crystallinity of *p-type* layers with the *TMB* concentration. In the case of $C_{TMB}$ = 3.5%, the p-type layer deposited on a glass is completely amorphous. It is known that an incorporation of boron may suppress the crystallinity [113,114].

The dark conductivity of *p-type* layers increases significantly from around $3x10^{-4}$ S/cm up to 0.6 S/cm with increasing $C_{TMB}$ from 0.5% to 2.25%, as shown in Figure 5.4 (b). A further increase in $C_{TMB}$ above 2.25% results in a decrease in the dark conductivity.

In addition, it is found in Figure 5.4 (c) that the thickness of the *p-type* layers increases obviously with $C_{TMB}$, although the deposition time is kept constant (8 min). The deposition rate of these *p-type* layers is calculated and shown in Figure 5.4 (d). One can see a significant increase in the deposition rate from 0.055 nm/s to 0.11 nm/s with increasing the $C_{TMB}$ from 0.5% to 3.5%. An increase in the deposition rate with the doping ratio was also previously reported [113]. With these deposition rates, one can estimate that the *p-type* layer thickness in the solar cells shown in Figure 5.3 increases from 13 nm to 25 nm with increasing $C_{TMB}$ in the investigated range (from 0.5% to 2.5%).

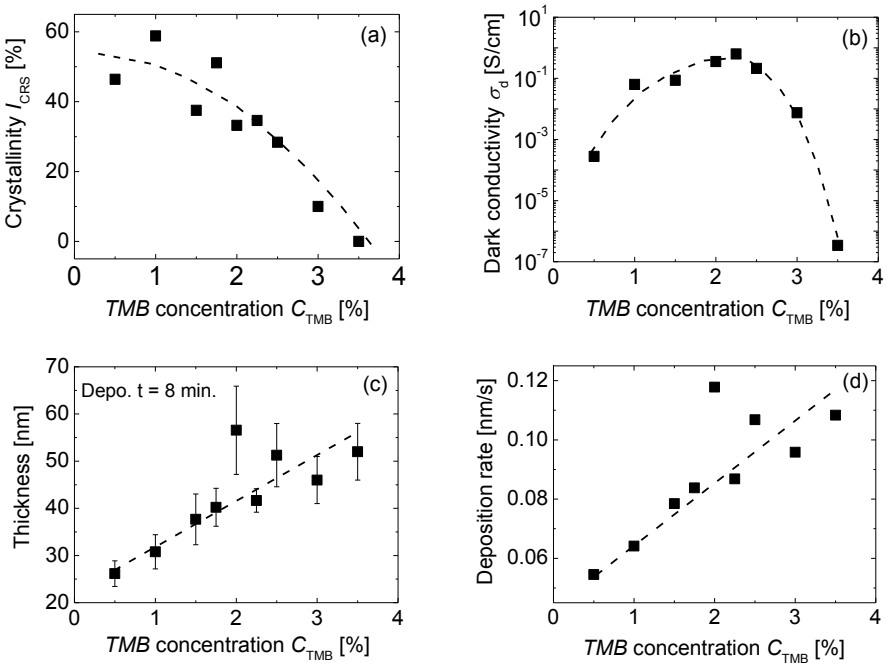


*Figure 5.4 The properties of the p-type layers: (a) the crystallinity, (b) dark conductivity, (c) thickness and (d) deposition rate as a function of the TMB concentration $C_{TMB}$. The variation trends are indicated with the dashed lines.*

**Discussion**

Both the thickness and the doping ratio influence significantly the material properties of *p-type* layers and the *n-i-p* solar cell performance. The effects on the *n-i-p* solar cell performance observed from our results are quite similar as for *p-i-n* solar cells which were

reported in [103]. In the following, these effects will be discussed with the changes in the properties of *p-type* layers.

A substantial improvement in the open circuit voltage with both rising the *p-type* layer thickness and also the doping ratio (see Figure 5.3) can be attributed to the increase in the dark conductivity in the p-type layers (see in Figure 5.2 and Figure 5.4), which results in a shifting of the Fermi level $E_F$ to the valence band and an enhancement in the built-in potential in the solar cells. The effects of the *p*-type layer thickness and the doping ratio on $V_{OC}$ are consistent with previous report on the properties of *p-i-n* solar cells [103]. However, the optimal *p-type* layer conditions for *p-i-n* and *n-i-p* cells are different since in the latter case the *p*-type layer does not serve as an immediate substrate for *μc-Si:H* absorber layer growth, and thus, the requirements for the *p-type* layer in terms of the crystallinity may be relaxed.

The fill factor values tend to rise with increasing the thickness and doping ratio of p-type layers, as evident in Figure 5.1 and Figure 5.3. It may be related to an improvement in the *TCO-p* contact. The work function difference between a *TCO* and a *p*-type layer leads to a potential barrier at the *TCO/p* interface and a depletion region in the *p*-type layer [17,115]. Increasing the thickness of *p*-type layers leads to an increase in their crystallinity (see in Figure 5.2) and therefore a decrease in the band gap. A decrease in the band gap of *p*-type layers may lead to a lower potential barrier at the *TCO/p* interface and an improvement in the transport of holes. Increasing the doping ratio of *p-type* layers can leads to a decrease in the depletion region length, which can result in an easier tunnelling for holes through the potential barrier.

The decrease in the short circuit current density seen in Figure 5.1 and Figure 5.3 can result from the increase in the p-type layer thickness and optical absorption in the *p-type* layers. The increase in $J_{SC}$ with the *TMB* doping ratio from 0.5% to 1.5% might be related to the increase in the dark conductivity of *p*-type layers, which may result in an improvement in carrier collection.

## 5.1.2 Front contact

The thickness of front contact (*ZnO*) layers can influence their electrical properties, light absorption and light in-coupling of solar cells. An increase in the *ZnO* thickness results in an enhancement in the mobility and carrier concentration of electrons [63][66] but higher absorptance. Moreover, a certain thickness of front contact layers leads to the anti-reflection effect on the front side of solar cells for the light with a certain wavelength. How exactly the

front *ZnO* thickness affects the performance of our *μc-Si:H n-i-p* solar cells were investigated and related to the change in the properties of the *ZnO* layers and the anti-reflection effect.

For this investigation, microcrystalline silicon *n-i-p* solar cells were prepared on glass/etched-*ZnO* substrates with the optimized *p-type* layer (shown in Section 5.1.2) and varied thicknesses of front contact (*ZnO*) layers from 30 nm up to 380 nm. Figure 5.5 shows the solar cell performance as a function of the front *ZnO* thickness $d_{ZnO}$. With varied thicknesses of front *ZnO* layers, the open circuit voltage remains almost constant with a mean value of 519 mV. The fill factor increases from 68.8% to 72.8% with increasing the front *ZnO* thickness in the investigated range. A significant sinusoidal-like variation in the short circuit current density with a reduced amplitude can be seen by changing the front *ZnO* thickness, with two peak positions at $d_{ZnO}$ = ~ 70 nm and $d_{ZnO}$ = ~ 240 nm. The efficiency follows the trend of the short circuit current density. The maximum short circuit current density of 19.4 mA/cm$^2$ and efficiency of 7.2% are obtained with the 70 nm thick front *ZnO* layer.

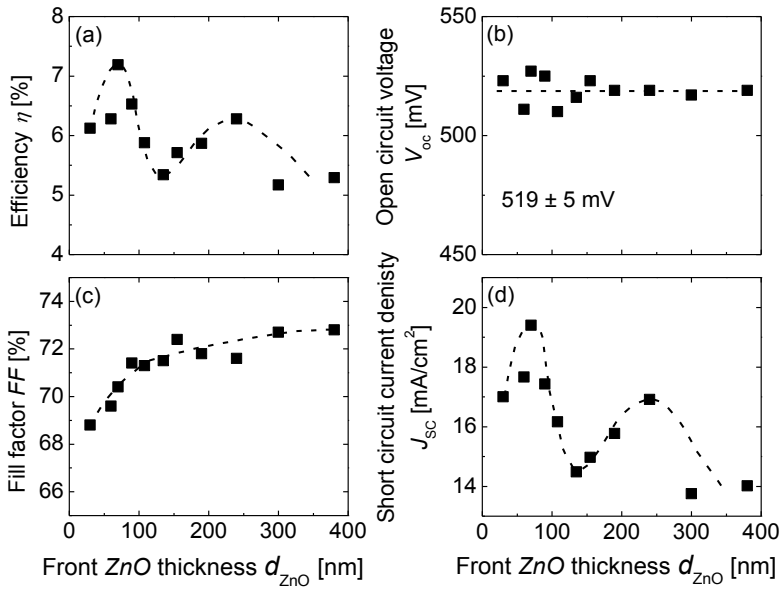


*Figure 5.5 (a) The efficiency η, (b) open circuit voltage $V_{OC}$, (c) fill factor FF and (d) short circuit current density $J_{SC}$ of the solar cells as a function of the front ZnO thickness $d_{ZnO}$. The dashed lines show the variation trends.*

To examine the effects of the thickness on the electrical and optical properties of *ZnO*, *ZnO* layers with varied thicknesses were prepared on glass substrates. The sheet resistance, light transmission $T_{ZnO}$ and reflectance $R_{ZnO}$ of the *ZnO* layers were measured. Figure 5.6 shows the resistivity and the sheet resistance of the *ZnO* layers as a function of the thickness. With increasing the *ZnO* thickness from 30 to 380 nm, the sheet resistance decreases from around 600 Ω/□ down to 20 Ω/□. The resistivity decreases slightly with increasing the *ZnO* thickness up to 155 nm and keeps almost constant with a further increase in the *ZnO* thickness. The absorptance $A_{ZnO}$ curves of the *ZnO* layers on glass substrates, calculated with $A_{ZnO} = 1 - T_{ZnO} - R_{ZnO}$, are presented in Figure 5.7 with the dashed lines, for the 30, 70, 155 and 240 nm thick layers. One can see slightly higher absorptance for thicker *ZnO* layers in the whole wavelength range.

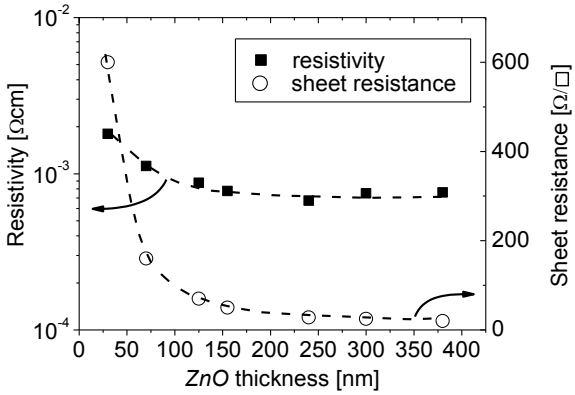


*Figure 5.6 The resistivity and sheet resistance of ZnO layers deposited on the glass substrates versus the ZnO thickness. ΄The variation trends are shown by the dashed lines.*

On the other hand, one can see in Figure 5.7 that the total reflectance of the solar cells $R_{Total}$ is significantly influenced by the thickness of front *ZnO* layers, particularly in the wavelength range between 400 nm to 800 nm. The 70 nm thick front *ZnO* results in the lowest total reflectance, which is only around 1 % at the wavelength close to 560 nm. The 155 nm thick front *ZnO* leads to the highest $R_{Total}$ (above 30 %) in the whole wavelength range from 400 nm to 1200 nm. The $R_{Total}$ values with the front *ZnO* thicknesses of 30 nm and 240 nm are between 3 % and 30 %. The 240 thick front *ZnO* leads to a sinusoidal-like curve of the total

reflectance versus the wavelength, with the highest $R_{total}$ of around 30 % at the wavelength close to 500 nm and the lowest $R_{total}$ of around 3% at the wavelength close to 640 nm.

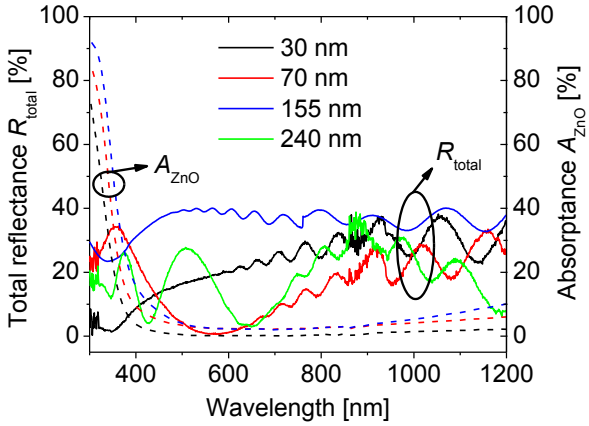


*Figure 5.7 The effects of the ZnO thickness on the total reflectance $R_{total}$ of solar cells and the absorptance $A_{ZnO}$ of the ZnO layers deposited on glass substrates.*

**Discussion**

From the results in Figure 5.5, it is found that the thickness of front *ZnO* layers influences mainly the fill factor and short circuit current density of the *μc-Si:H* solar cells. The increase in the fill factor for $d_{ZnO}$ < 155 nm is related to the decrease in the resistivity and the sheet resistance of *ZnO* layers with the thickness (see Figure 5.6).

The variation in the short circuit current density can be related to the change in the total reflectance $R_{total}$ of solar cells and the absorptance $A_{ZnO}$ of the *ZnO* layers together. For the front *ZnO* layers investigated here, the effect of the thickness on $R_{total}$ is much stronger than the effect of absorptance in *ZnO* layers (see Figure 5.7). It suggests that the variations in $J_{SC}$ with the front *ZnO* thickness are largely attributed to the total reflectance of solar cells.

The variations in total reflectance with the front *ZnO* thickness can be explained by the anti-reflection effect. There are two requirements for an anti-reflection coating on silicon [116]:

$$n_{AR} = \sqrt{n_{air} n_{Si}} \tag{5.1}$$

$$d = \frac{k\lambda}{4n_{AR}} = \frac{k\lambda}{8} (k = 1,3,5,7...) \tag{5.2}$$

where $n_{AR}$ is the refractive index of the anti-reflection coating, $n_{air}$ and $n_{Si}$ are the refractive indices of air and silicon, respectively, $d$ is the thickness of the anti-reflection coating and $\lambda$ is the wavelength of light. The front *ZnO* layer with a refractive index of around 2 may provide an anti-reflection effect, since $n_{Si}$ is close to 4. According to Eq. 5.2, the 70 nm thick *ZnO* can result in an anti-reflection effect at a wavelength of 560 nm, whereas the 240 nm thick *ZnO* at a wavelength of 640 nm. This is in agreement with our results presented in Figure 5.7.

## 5.2 Absorber layer

The structure, electrical transport properties and the optical absorption of absorber layers (*i*-layers) is significantly influenced by the deposition conditions, such as the silane concentration *SC* and the discharge power *P* of plasma [27,106]. The effects of the deposition conditions on the material properties of *i*-layers and the solar cell performance were investigated in the past for both *n-i-p* and *p-i-n* configurations [27,102,106]. In this work, the *SC* was optimized for our *μc-Si:H n-i-p* solar cells. A series of solar cells were prepared on glass/etched-*ZnO* substrates with the optimized window layers (described in Section 5.1) and varied *SC* in *i*-layers. The thickness of the absorber layers in the solar cells was kept the same (around 1 μm) by adjusting the deposition time, according to the corresponding deposition rate for a given *SC*.

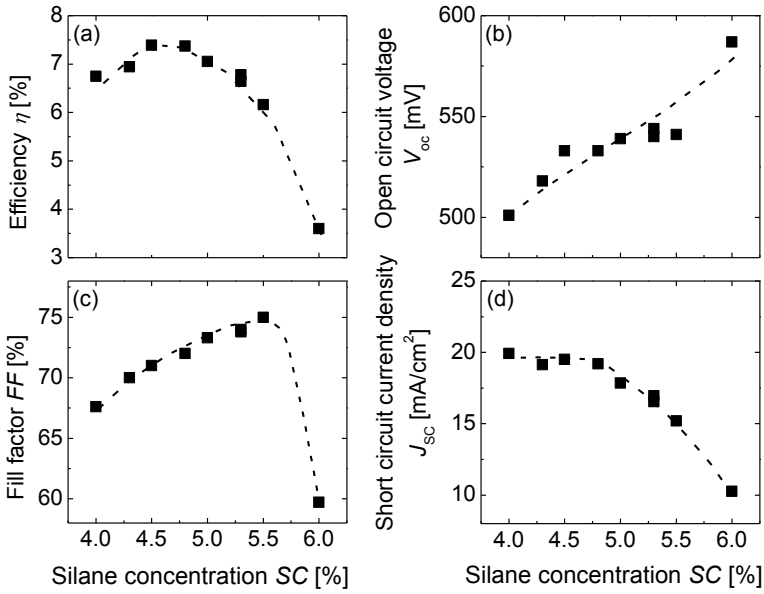


*Figure 5.8 (a) The efficiency η, (b) open circuit voltage $V_{OC}$, (c) fill factor FF and (d) short circuit current density $J_{SC}$ of the solar cells as a function of the silane concentration SC of i-layers. The dashed lines are for guiding the eyes.*

Figure 5.8 shows the performance of solar cell versus the silane concentration *SC* of *i*-layers. With increasing the silane concentration from 4% to 6%, the open circuit voltage increases from 500 mV up to 590 mV. The short circuit current density has a constant high value of around 19.5 mA/cm$^2$ at the *SC* between 4% and 4.75% and decreases down to around 10 mA/cm$^2$ with increasing the SC to 6%. The fill factor increases firstly from 68% up to 75% with the *SC* and drops suddenly down to below 60% at the *SC* of 6%. As a result of these changes in the $V_{OC}$, *FF* and $J_{SC}$, the highest efficiency of around 7.4% is achieved at the *SC* of 4.5%.

To examine the change in the structure properties (crystalline volume fraction) of the absorber *i*-layers in the solar cells, Raman scattering measurements are done through the *p-type* layers, with excitation at 647 nm. The crystallinity $I_{CRS}$ is shown in Figure 5.9 (a) versus the silane concentration *SC*. One can see that $I_{CRS}$ is reduced from 73% to 12% by increasing *SC* from 4% to 6%.

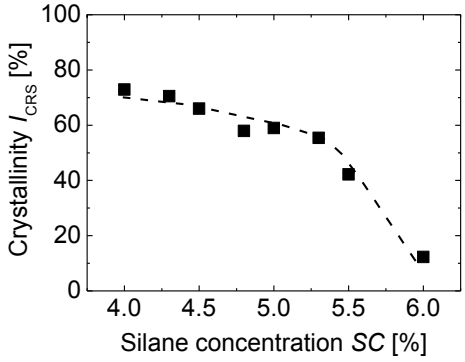


*Figure 5.9 The crystallinity $I_{CRS}$ of i-layers versus the silane concentration SC*

The effects of the silane concentration on the solar cell performance observed from our results are quite similar as those found for both *n-i-p* and *p-i-n* solar cells in the earlier work [27,102,106]. The increase in the $V_{OC}$ with the *SC* (see Figure 5.8) is attributed to the increased amorphous fraction which leads to a wider "effective" band gap of *i*-layers. The decrease in the $J_{SC}$ with the *SC* is related to lower absorption of red and infrared light [27,102] and more difficult extraction of carriers in more amorphous *i*-layers. The sudden decrease in *FF* at *SC* = 6% suggests an onset of amorphous growth and therefore degrading of the transport properties [39,40]. The highest efficiency is achieved with the *SC* of 4.5% which results in an *i*-layer crystallinity of around 65%.

## 5.3 Back reflector

For the investigation of window and absorber layers presented in the last sections, all the solar cells were prepared on simple glass/etched-*ZnO* substrates. To improve the short circuit current density, an *Ag/ZnO* back reflector was added between glass/etched-*ZnO* substrates and silicon layers. The sketches of *n-i-p* solar cells with and without the *Ag/ZnO* back reflector have been shown in Figure 3.1 (a) and (b).

A series of solar cells were prepared with varied *TMB* concentrations $C_{TMB}$ for *p*-type layers on two types of substrates: glass/etched-*ZnO* and glass/etched-*ZnO/Ag/ZnO*. The performance of solar cells is shown in Figure 5.10. The same variation trends of the solar cell performance ($V_{OC}$, *FF*, $J_{SC}$ and $\eta$) with the *TMB* concentration can be observed for both types of substrates. The open circuit voltages of the solar cells are almost the same in the both cases.

By adding the *Ag/ZnO* back reflectors, the fill factor seems to be slightly improved, whereas the short circuit current density is improved significantly by about 2 mA/cm$^2$ for all the solar cells investigated here.

Figure 5.11 shows the quantum efficiency *QE* curves of the solar cells with the optimized *p-type* layer ($C_{TMB}$ = 1.5%, deposition time = 4 min.), on both types of substrates (glass/etched-*ZnO* and glass/etched-*ZnO/Ag/ZnO*). A significant improvement in the quantum efficiency can be seen in the long wavelength range ($\lambda$ = 550 ~ 1100 nm) by adding the back reflector.

All these results suggest that a simple glass/etched-*ZnO* substrate can serve as a reproducible standard for the optimization of *n-i-p* solar cells and the $J_{SC}$ can be improved by about 2 mA/cm$^2$ by adding an *Ag/ZnO* reflector on it.

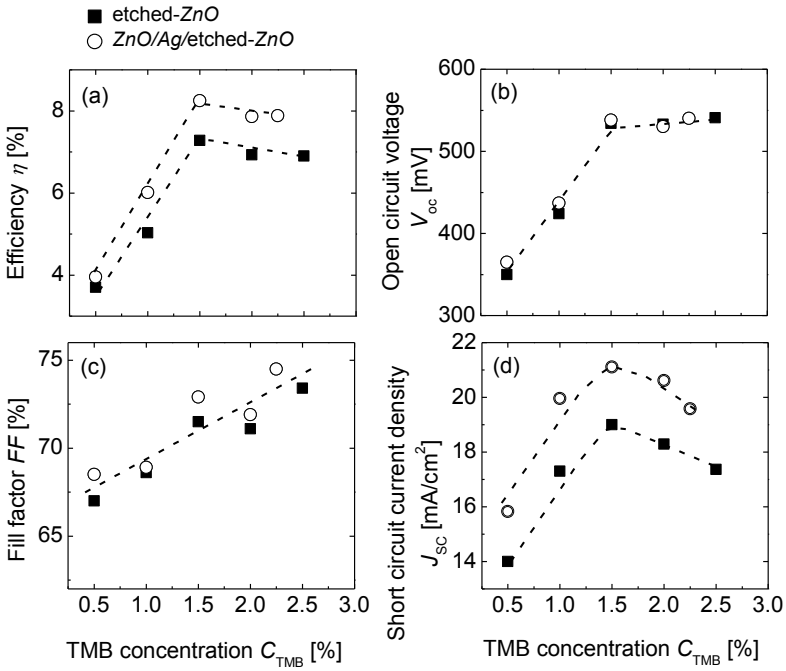


*Figure 5.10 (a) The efficiency η, (b) open circuit voltage $V_{OC}$, (c) fill factor FF and (d) short circuit current density $J_{SC}$ of a series of solar cells prepared with the different $C_{TMB}$ for the p-type layers on the two types of substrates: glass/etched-ZnO and glass/etched-ZnO/Ag/ZnO. The dashed lines are to guide the eyes.*

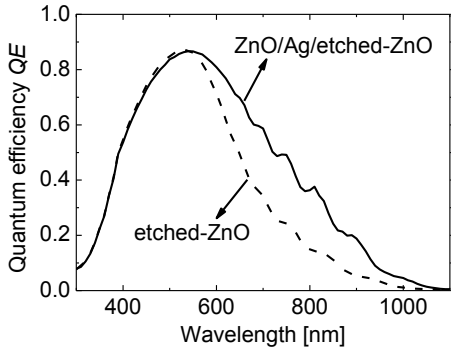


*Figure 5.11 The quantum efficiency QE curves of the solar cells with the optimized p-type layer on the two substrates: glass/etched-ZnO and glass/etched-ZnO/Ag/ZnO*

## 5.4 Summary

This chapter has presented transferring the optimized processes for *μc-Si:H p-i-n* solar cells into *μc-Si:H n-i-p* solar cells. The main results will be summarized in the following:

- **P-type layer**

Using the optimized deposition conditions of the *p-type* layers for *p-i-n* solar cells, the *n-i-p* solar cells have a poor performance with a much lower $V_{OC}$ and *FF* than that in the *p-i-n* solar cells. The lower $V_{OC}$ and *FF* might result from: (1) a lower doping concentration of the *p-type* layers grown on the *μc-Si:H i*-layer in the *n-i-p* cells than those grown on the *ZnO* substrate in the *p-i-n* solar cells; (2) damages of the *p-type* layers in the *n-i-p* solar cells by the sputtering process of the front *TCO* layer. These suspected causes for the lower $V_{OC}$ and *FF* in the *n-i-p* solar cells were not proved in this work. However, we found that both the $V_{OC}$ and *FF* in *n-i-p* solar cells can be significantly improved by increasing the doping ratio and/or thickness of *p-type* layers, which is related to the increase in the dark conductivity of the p-type layers. On the other hand, an increase in the thickness of *p-type* layers leads to a decrease in the short circuit current density, due to the higher parasitic absorption of the *p-type* layers. Therefore, a thin *p*-type layer with a high doping ratio has to be used in *n-i-p* solar cells to obtain high cell efficiencies.

- **Absorber layer (i-layer)**

The effects of the *i*-layer silane concentration *SC* on the performance of *μc-Si:H n-i-p* solar cells were investigated. The open circuit voltage increases with the *SC*, whereas the short circuit current density decreases. The fill factor increases firstly with the *SC* and drops suddenly down at *SC* > 5.5%. The highest efficiency is achieved with the *SC* of 4.5%, which leads to an *i*-layer crystallinity of around 65%, close to the transition to the amorphous growth regime.

- **Front contacts**

*ZnO* deposited at a low substrate temperature was used as the front contacts in the *μc-Si:H n-i-p* solar cells to avoid damaging the underlying silicon layers. The effects of the front *ZnO* layer thickness on the *n-i*-p solar cell performance were investigated in this work. The fill factor increases with the *ZnO* layer thickness, which is related to the decrease in the resistivity and sheet resistance of the *ZnO* layers. The open circuit voltage of all the solar cells

are almost the same, while the main effect of the *ZnO* thickness is the $J_{SC}$ of the solar cells. The variation in the $J_{SC}$ is mainly attributed to the total reflectance of solar cells. The optimal thickness of front *ZnO* layers is found to be around 70 nm, due to the anti-reflection effect.

- **Substrate**

Two types of substrates (*glass/etched-ZnO* and *glass/etched-ZnO/Ag/ZnO*) were used in a series of *μc-Si:H n-i-p* solar cells prepared with varied *p-type* layer doping ratios. The same variation trends of the cell performance are found with and without the *Ag/ZnO* reflector. It suggests that glass*/ZnO* substrates can serve as a benign and reproducible standard for the optimization of *n-i-p* solar cells. When a highly reflective *Ag/ZnO* reflector is used in a *μc-Si:H* solar cell, the short circuit current density is improved by around 2 mA/cm$^2$.

In conclusion, the window and absorber layers in *μc-Si:H n-i-p* solar cells were optimized based on the optimized deposition conditions for *p-i-n* solar cells. The effects of the thickness and doping ratio of *p*-type layers and the silane concentration of absorber layers on the *n-i-p* solar cell performance are quite similar as those observed in *p-i-n* solar cells in the past [102,103,106]. The optimal thickness of front *ZnO* layers is around 70 nm, due to the anti-reflection effect. By using the optimized window and absorber layers and a highly reflective glass/etched-*ZnO/Ag/ZnO* substrate, overall high performance with an efficiency of 8.25% is achieved for the *μc-Si:H n-i-p* solar cells with an around 1 μm thick *i*-layer. Based on the good process reproducibility and high solar cell performance, the light scattering and trapping in *μc-Si:H n-i-p* solar cells were able to be investigated and will present in the next chapter.

# 6. Back reflector morphology and light scattering & trapping in *n-i-p* solar cells

As described in Section 2.2.3, the surface of sputtered *ZnO* films can be textured by etching in *HCl* solution. Textured *ZnO* films are often used as front contacts in solar cells with a *p-i-n* configuration [11,13,14,70,77,117–119]. However, the optimization of the *ZnO* surface morphology for light trapping was limited by the requirements for the optical and electrical properties of the *ZnO* layers. In this work, we relax this limitation by covering the textured *ZnO* layer with a thin *Ag* and *ZnO* layers and use them together as back reflector in solar cells with a substrate (*n-i-p*) configuration (as described in Section 3.1). By doing so, we have large freedom to vary the *ZnO* surface morphology and possibility to directly analyse the relationship between the surface morphology, the light-scattering properties and the solar cell performance, without taking care about both the optical transparency and sheet conductance of the textured *ZnO* layers.

This chapter presents firstly the variation of the *ZnO* surface morphology by changing the etching time and as-deposited thickness of the *ZnO* layers. The *ZnO* surface morphology is evaluated by means of *AFM* measurements in terms of not only the rms roughness $\delta_{rms}$, but also the diameter $d$, depth $h$ and angle $\alpha$ of craters on the surfaces. Then, the light-scattering properties of etched-*ZnO/Ag* reflectors are examined in terms of the haze and angular intensity distribution *AID*. The relationship between the surface morphology and light-scattering properties of the reflectors is analysed. Finally, the effects of the back reflector morphology on the performance of *μc-Si:H n-i-p* solar cells are investigated. Two relationships: one between the light-scattering properties of the back reflectors and the light trapping in the solar cells and the other between the back reflector morphology and the light trapping are discussed. All types of the investigations presented in this chapter are summarized in Figure 6.1.

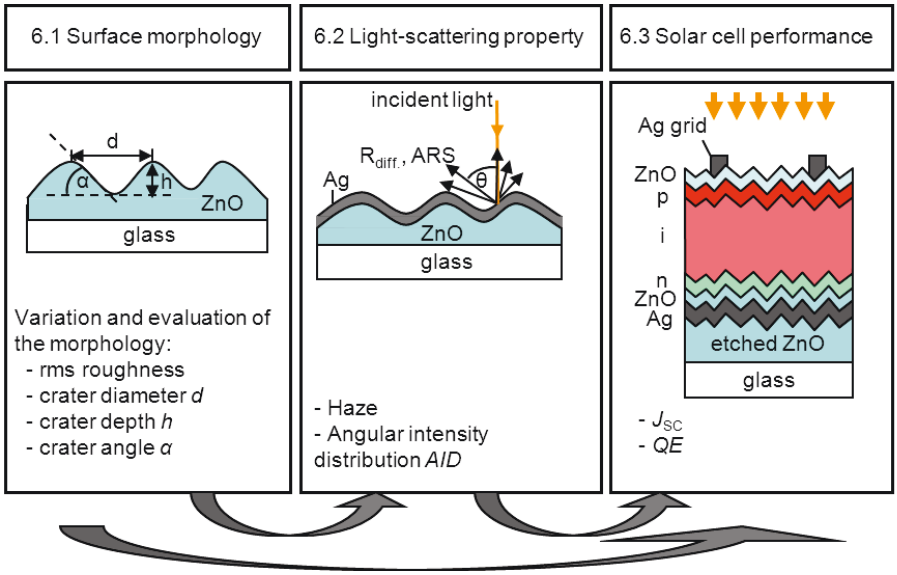


*Figure 6.1 Summary of all the investigations presented in the following sections of this chapter. Section 6.1 will present variation and evaluation of the ZnO surface morphology. Section 6.2 will present the light scattering properties of etched-ZnO/Ag reflectors. Section 6.3 will present the performance of n-i-p solar cells prepared on glass/etched-ZnO/Ag/ZnO substrates. Three relationships as shown with the arrows in the figure will be discussed in the following sections. The first relationship is between the surface morphology and light scattering properties of reflectors, the second one is between the light scattering properties of back reflectors and light trapping in the solar cells and the third one is between the surface morphology of back reflectors and the light trapping.*

## 6.1 Zinc oxide surface morphology

As already described in Section 2.2.3, there are three types of *ZnO* surface morphologies (Type *A*, *B* and *C*) after etching in *HCl* solution, depending on the deposition conditions. The so-called Type B morphology with homogenous crater-like features on the surface results in better light trapping than the others for *p-i-n* solar cells [11]. By changing the etching time, the rms roughness of Type *B ZnO* surfaces and the size of the craters can be adjusted, however, the angle $\alpha$ of the craters on the *ZnO* surfaces are quite similar [11,66,120].

Recent publications reported the modification of the surface morphology by etching *ZnO* layers in *HF* solution [66,121–123]. In comparison with etching in *HCl* solution, the crater angle $\alpha$ on the *ZnO* surfaces etched in *HF* solution is much larger; however, the diameter of most of the craters is much smaller [66,121]. The crater diameter on the *ZnO* surfaces etched in *HF* solution is only 200 ~ 300 nm, while it is 1 ~ 3 µm on the *ZnO* surfaces etched in *HCl* solution.

Therefore, keeping the textures on *ZnO* surfaces crater-like and controlling the angle and size of the craters independently seem to be a challenging issue. In this section, we will present approaches to vary the rms roughness of *ZnO* surfaces over a wide range and the angle and size of craters independently.

### 6.1.1 Variation and statistical analysis

In this work, the surface morphology of Type *B ZnO* layers was varied by changing not only the etching time but also the as-deposited thickness of *ZnO* layers. The initial motivation of using *ZnO* layers thicker than the standard front *ZnO* for *p-i-n* solar cells was to form larger and deeper craters on the surfaces before *ZnO* is etched down to glass substrates. During the experiments and evaluations, more effects of the as-deposited thickness on the etched-*ZnO* surface morphology were observed and will be present in the following.

**3D AFM image**

The *ZnO* layers with the different as-deposited thicknesses $d_{ZnO}$ of 550 nm, 800 nm, and 1050 nm were etched in *HCl* solution with the varied etching time *t* from 10s to 100s. The 3D *AFM* images of some of the etched *ZnO* layers are shown exemplarily in Figure 6.2. Crater-like structures can be seen on all the *ZnO* layers. In average, the crater diameter increases either with the etching time for a given as-deposited thickness of the *ZnO* layers or with the

as-deposited thickness at a given etching time. Above a certain etching time, the *ZnO* is over-etched down to the glass substrate, as shown with the white arrows in Figure 6.2.

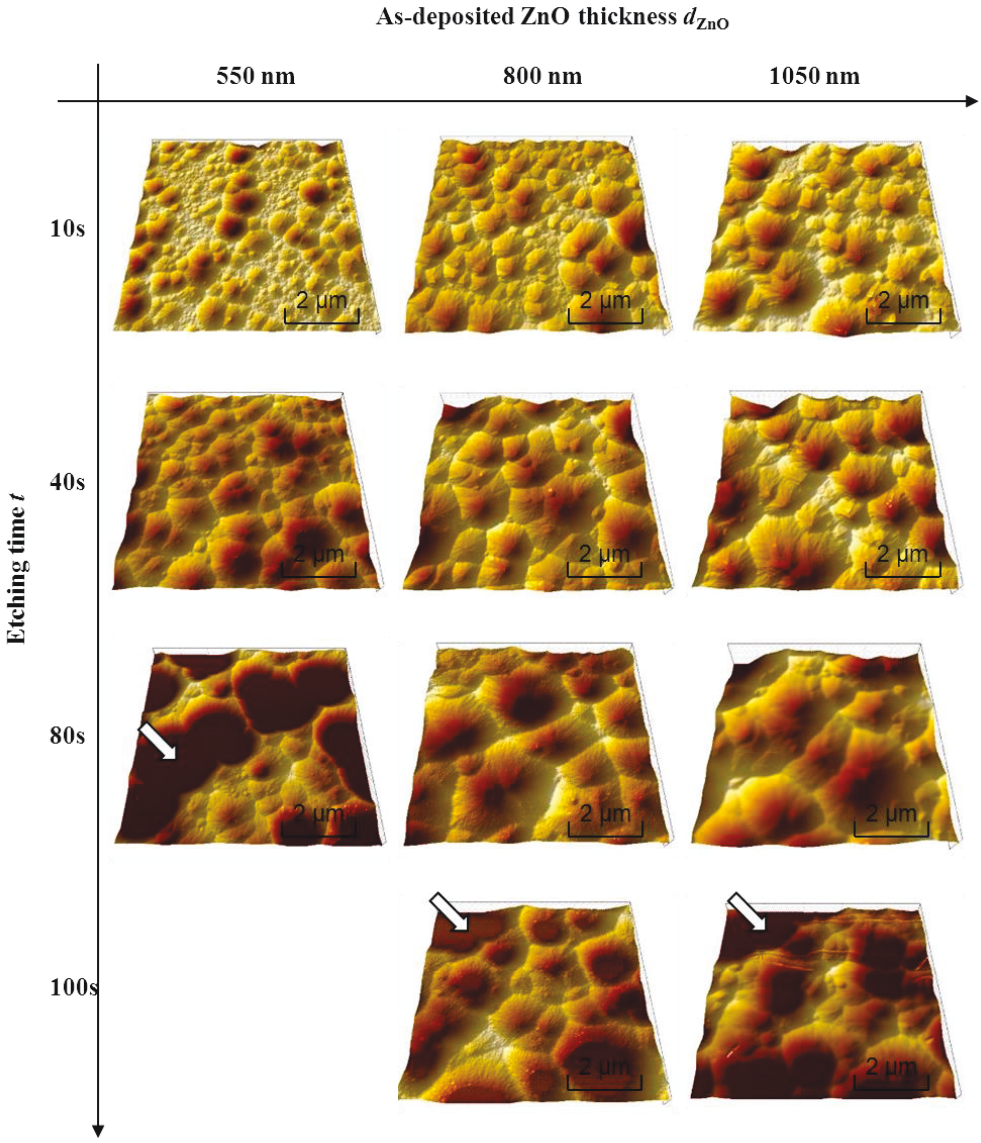


*Figure 6.2 3D AFM images of the ZnO layers with varied thicknesses of 550 nm, 800 nm, and 1050 nm, etched for 10 s, 40s, 80s and 100 s. Some flat area on the surfaces is indicated by the white arrows.*

**Root mean square (rms) roughness**

Figure 6.3 (a) shows the rms roughness $\delta_{rms}$ versus the etching time for the *ZnO* surfaces with the different as-deposited thicknesses. The $\delta_{rms}$ increases with the etching time sharply upon initial etching from the (un-etched) $\delta_{rms}$ = 3 - 5 nm to the values of 100 - 170 nm, depending on the as-deposited thickness, before it gets into a saturation. The rms roughness finally decreases again when the etch-resistant substrate (glass) is revealed. The variation in the rms roughness is influenced by the as-deposited thickness. At a given etching time, the $\delta_{rms}$ is considerably higher for the thicker films.

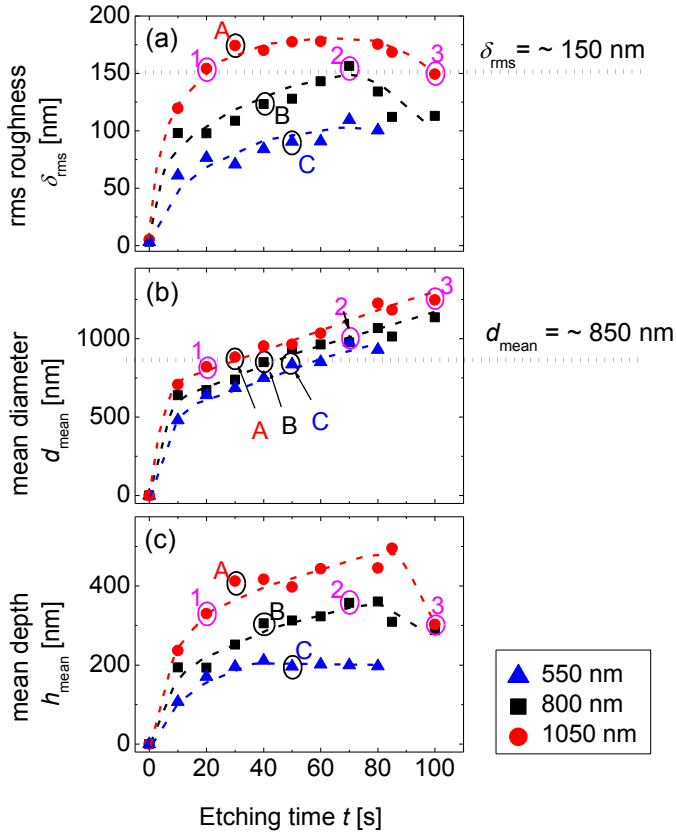


*Figure 6.3 Variations in (a) the rms roughness $\delta_{rms}$, (b) the mean diameter $d_{mean}$ and (c) the mean depth $h_{mean}$ as function of etching time t for the ZnO layers with different as-deposited thicknesses. Samples A, B, and C as well as 1, 2 and 3 are selected for comparison (see details in text).*

**Mean diameter and depth of craters**

Besides the rms roughness, more detailed analyses of the *ZnO* surface morphology are performed in this study, in terms of the geometry of craters on the surface: the diameter $d$, the depth $h$ and the angle $\alpha$. The definitions and evaluation methods of these three parameters have been introduced in Section 4.1. The mean diameter $d_{mean}$ and the mean depth $h_{mean}$ of craters on all the *ZnO* surfaces are shown in Figure 6.3 (b) and (c), respectively.

It is noticed that the *Zn*O layers with a similar $\delta_{rms}$ of 150 nm (Sample 1, 2 und 3 under the dotted line in Figure 6.3 (a)) have the quite different mean diameters from 820 nm to 1250 nm and depths from 330 nm to 360 nm (see in Figure 6.3 (b) and (c)). With such different sizes of craters, these three samples may have different light-scattering properties, which will be presented in Section 6.2. Therefore, it can be concluded that the $\delta_{rms}$ alone is not sufficient to determine a surface morphology and the combination of the diameter, depth and angle of craters on a surface may be a better description with respect to its optical functionality. In the following, the variation of the *ZnO* surface morphology with the etching time and as-deposited thickness will be analysed in terms of the mean diameter and depth of craters on the surface.

One can see in Figure 6.3 (b) and (c) that both the mean diameter and depth are varied significantly by the etching time. For the *ZnO* layers with a given as-deposited thickness, the mean diameter always increases with the etching time, while the mean depth increases only up to a certain etching time and then decreases due to the over etching of *ZnO* down to the glass substrate.

Additionally, the variations in the mean diameter and depth with the etching time are influenced by the as-deposited thicknesses of the *ZnO* layers. At a given etching time, both the values are higher for thicker *ZnO* layers. Moreover, it is noticed that the influence of the *ZnO* as-deposited thickness on the mean depth is much stronger than on the mean diameter. Consequently, the geometry of the craters should also depend on the as-deposited thickness of the *ZnO* layers. For example, the samples under the dotted line in Figure 6.3 (b) (*A*, *B* and *C*) have almost the same mean diameter of 850 nm, but the mean depth increases almost twice from around 200 nm to 410 nm with an increase in the as-deposited thickness from 550 nm to 1050 nm.

**Surface angle distribution**

Figure 6.4 shows the surface angle distributions of the *ZnO* layers with different etching time and as-deposited thicknesses. For the *ZnO* layers not over-etched down to the glass substrates, the surface angle distributions with the same as-deposited thickness have a quite

similar peak position, independent on the etching time. For example all the surface angle distributions of the 800 nm *ZnO* layers etched from 10 s to 80 s have similar peak positions of around 25°. This independency on the etching time has also been noted in Ref. [11,66]. On the other hand, with increasing the as-deposited thickness from 550 over 800 to 1050 nm, the peak position of the surface angle distributions, which is defined as the crater angle α (described in Section 2.4), shifts to higher value from around 20° over 25° to 30°.

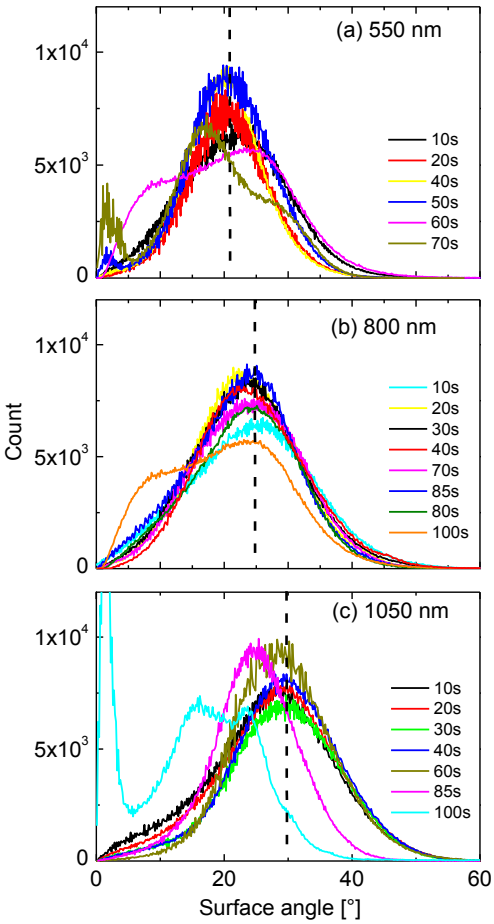


*Figure 6.4 Surface angle distributions of the ZnO layers with different etching times for different as-deposited thicknesses: (a) 550 nm, (b) 800 nm and (c) 1050 nm. The dashed lines show the peak position of the surface angle distributions for most of samples in each graphics. The arrows indicate the second peaks of the surface angle distributions for the* ZnO *layers over-etched down to the glass substrates.*

For the *ZnO* layers over-etched down to the glass substrates, for example, the 550 nm thick *ZnO* etched from 50 s to 70 s, one can see a second peak of the surface angle distribution at small angles. which has also been noted in Ref. [11,66] and considered as the surface angles of the glass substrate [66].

**Distribution of crater diameters and depths**

Above, the surface morphology has been analysed in terms of the mean diameter and depth of all the craters on the ZnO surfaces. With these mean values, we can learn the general variation trends of the craters on the surfaces with respect to the as-deposited thickness and the etching time. However, on the same etched ZnO surface, the craters have quite different diameters and depths (see

Figure 6.2). Therefore, to analyse the craters on the surfaces in more details and relate them later to light trapping in solar cells, the distributions of the crater diameters and depths are calculated for some representative surfaces. For each surface, 10 *AFM* images with a scan area of 7x7 $\mu m^2$ are used to calculate the distributions with a large amount of craters.

Figure 6.5 shows the distributions of crater diameters on an 800 nm thick *ZnO* layer etched for different times of (a) 10 s, (b) 40 s and (c) 80 s. After 10 s etching, large craters with a diameter of around 1700 nm are already formed on the surface. However, most of the surface is covered by craters with a diameter smaller than 1500 nm. The maximum of the diameter distribution on the *ZnO* etched for 10 s is located at around 700 nm. With increasing the etching time, the maximum shifts to large values. After 40 s etching, the maximum of the crater diameter distributions is located at around 1500 nm, while after 80 s etching it is located at around 1700 nm. The shift of the diameter distribution with the etching time is in agreement with the variation in the mean diameter observed in Figure 6.3 (b). In addition, it is noticed that the diameter distribution becomes broader with increasing the etching time.

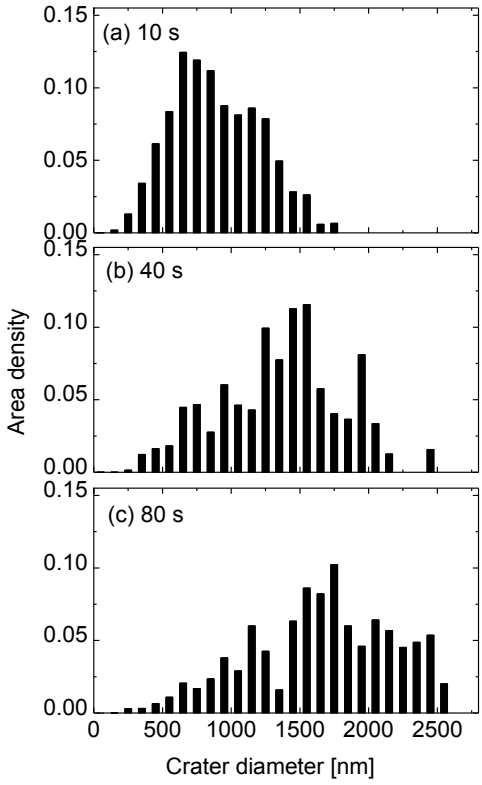


*Figure 6.5 Distributions of crater diameters on an 800 nm thick ZnO layer etched for different times of (a) 10 s, (b) 40 s and (c) 80 s.*

Figure 6.6 shows the distributions of crater depths on the *ZnO* layers with different as-deposited thicknesses of 550 nm, 800 nm and 1050 nm, etched for different time (a) 10 s, (b) 40 s and (c) 80 s. For a given *ZnO* layer, the maximum of the crater depth distributions shifts to larger values with increasing the etching time. Moreover, the crater depth distribution is significantly influenced by the as-deposited thickness of the *ZnO* layers. For a given etching time, the distribution shifts to larger depths with increasing the as-deposited thickness, which indicates a higher proportion of deep craters on thicker *ZnO* layers. For example, after a short etching of 10 s, most of the craters on the thinnest *ZnO* layer (550 nm) are shallower than 100 nm, whereas on the thickest layer (1050 nm) most of the craters are already deeper than 100 nm.

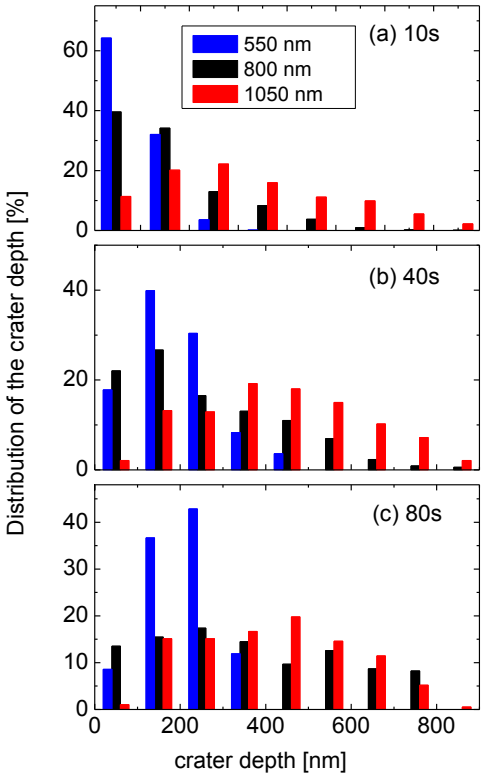


*Figure 6.6 Distributions of crater depths on the ZnO layers with different as-deposited thicknesses of 500 nm, 800 nm and 1050 nm, etched for different times of (a) 10 s, (b) 40 s and (c) 80 s.*

## 6.1.2 Etching model

Based on the statistical analysis presented above, the effect of the etching time and as-deposited thickness on the etching behaviour of *ZnO* layers in *HCl* solution will be discussed and related to the microstructure of *ZnO* material in the following.

For the *ZnO* layers with a given as-deposited thickness, both the mean diameter and depth of craters increase with the etching time before some *ZnO* is over-etched down to the glass substrate (see Figure 6.3). The peak positions of the surface angle distributions are quite similar with the different etching time (see Figure 6.4). These results indicate that with increasing the etching time, craters on the surfaces become in average larger and deeper with similar crater angles.

In addition, it is found that the increase in both the mean diameter and depth of craters is much sharper in the first 10 s of the etching, which indicates a fast initial etching rate in both lateral and vertical directions. The average etching rate in a given time range in the lateral and vertical direction was calculated with the difference in the mean diameter and depth of craters divided by the time, respectively. For the 800 nm thick *ZnO* layers, the average etching rate in the first 10 s is around 60 nm/s and 19 nm/s in lateral and vertical direction, respectively. In the etching time between 10 s and 80 s, the average etching rate drops significantly down to around 6.6 nm/s and 2.3 nm/s in lateral and vertical direction, respectively. The fast initial etching rate might indicate an inhomogeneity of the microstructure in *ZnO* material in the growth direction.

For a given etching time, both the mean diameter and depth of craters on the surfaces increase with increasing the as-deposition thickness of *ZnO* layers $d_{ZnO}$ (see Figure 6.3). The increase in the mean depth with the $d_{ZnO}$ is more significant than the mean diameter. Moreover, with increasing the $d_{ZnO}$, the peak position of the surface angle distributions shifts to larger angles (see Figure 6.4), which means that the craters on thicker *ZnO* layers have bigger crater angles $\alpha$ than those on thinner ones.

In addition, the initial etching rate increases significantly with the as-deposition *ZnO* thickness in both lateral and vertical directions. With increasing as-deposition *ZnO* thickness from 550 nm to 1050 nm, the average etching rate in the first 10 s increases from 48.0 nm/s to 70.8 nm/s in the lateral direction and from 10.7 nm/s to 23.6 nm/s in the vertical direction. After 20 s of etching, the average etching rate becomes similar for *ZnO* layers with different as-deposition thicknesses.

All these changes in the etching behaviour with the etching time and *ZnO* as-deposition thickness might be related to the microstructure of *ZnO* material. The growth of this type of *ZnO* layers used in this work has been investigated by Zhang [93] and Owen [66]. It was found that the growth starts with randomly oriented grains. After competition of the fastest growth among the grains in the nucleation region (100 nm ~ 200 nm), (001) *ZnO*-terminated grains perpendicular to the substrates overcome others and dominate the surface. Furthermore, Owen [66] developed an etching model which has been introduced in Section 2.2.3. In that etching model, it was proposed that the (001) plane of *ZnO*-terminated grains cannot be etched by *HCl*, whereas grain boundaries have potential to be etched. The etching potential depends on the structure disorder of the grain boundaries. Grain boundaries with less order may have higher potential for etching.

More detailed microscopic model of the *ZnO* growth and etching does not exist so far. We developed a phenomenological model which can be used to explain our experimental results, as follows: The different etching behaviour with the etching time and as-deposition *ZnO* thickness might be attributed to a variation in the disorder of grain boundary along the growth direction. Figure 6.7 shows the schematic graphics of *ZnO* layers grown on glass substrates for (a) a thin *ZnO* layer and (b) a thicker *ZnO* layer. We assume that grain boundaries close to the surfaces are less-ordered and have low compactness or even voids. The less-ordered grain boundaries are indicated in Figure 6.7 with blue dashed lines. We define the region closed to the surfaces with less-ordered grain boundaries as the surface region. In the surface region, etching agent can more easily penetrate the less-ordered grain boundaries, which leads to a fast initial etching rate. The distance of the surface region might increase with the as-deposited thickness of *ZnO* layers. A longer surface region in a thicker *Zn*O layer may lead to higher initial etching rates, especially in the vertical direction and therefore sharper craters.

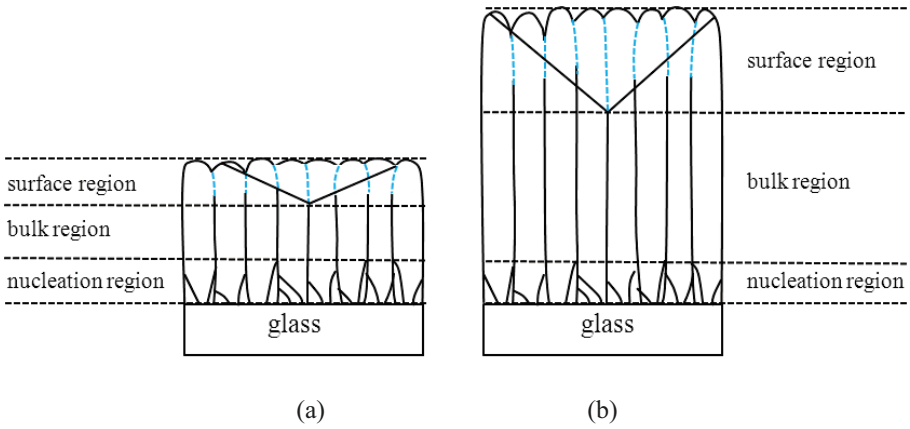


*Figure 6.7 Schematic graphics of ZnO layers grown on glass substrates for (a) a thin ZnO layer and (b) a thicker ZnO layer. Three regions in the growth direction, surface region, bulk region and nucleation region, are shown for both thin and thick ZnO layers in (a) and (b). Less-ordered grain boundaries in the surface region are shown with blue dashed lines for both thin and thick ZnO layers in (a) and (b).*

### 6.1.3 Summary of possible surface morphology variations

The results presented in Section 6.1.2 show that we are able to vary not only the rms roughness of *ZnO* surfaces over a wide range, but also the sizes and angle of craters on the surfaces independently. In Table 6.1, four possible variations of the *ZnO* surface morphology are summarized.

The first possible variation *I* can be achieved by etching the *ZnO* layers with the same as-deposited thickness for different time, before the glass substrate is exposed. Both the diameter and depth of craters increase with the etching time. The peak positions of the surface angular distributions are quite similar, which indicates a similar crater angle α on the surfaces.

The second possible variations *II* and *III* can be achieved by adjusting both the etching time and the as-deposited *ZnO* thickness. By changing the as-deposited *ZnO* thickness, the crater angle can be varied. Then, by adjusting the etching time, one can keep either the mean diameter or depth of craters constant and achieve either Variation *II or III*.

In the fourth possible variation *IV*, *ZnO* is etched down to glass substrates on some places and flat area on the surfaces can be seen. With increasing the etching time, the mean crater diameter and flat area increase, whereas the rms roughness and the crater depth decrease. A second peak of the surface angle distribution at small angles can be seen.

| | Schematic diagram | Crater size | Surface angular distribution | Approach *or method* |
|---|---|---|---|---|
| I | 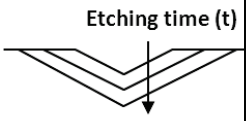 | - varied $d_{mean}$<br>- varied $h_{mean}$ | 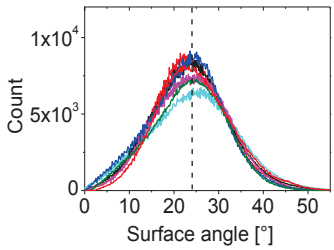 | - keep $d_{ZnO}$ same<br>- vary *t* |
| II | 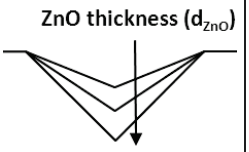 | - similar $d_{mean}$<br>- varied $h_{mean}$ | 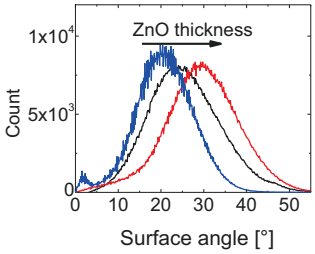 | adjust $d_{ZnO}$ and *t* |
| III |  | - varied $d_{mean}$<br>- similar $h_{mean}$ | 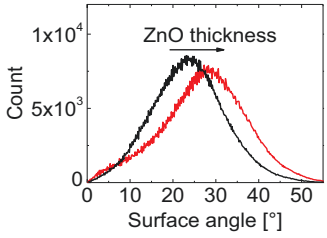 | adjust $d_{ZnO}$ and *t* |
| IV | 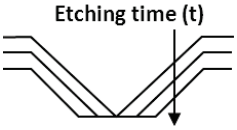 | - varied $d_{mean}$ and $h_{mean}$<br>- varied flat area with *t* | 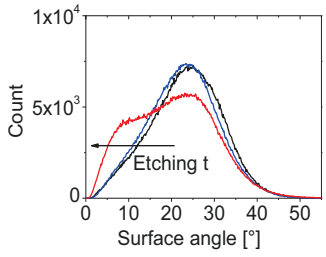 | - keep $d_{ZnO}$ same<br>- vary t, after the ZnO layer is over-etched down to glass substrates |

*Table 6.1 The schematic diagram, approach or method to achieve the variations and changes in the relevant parameters (size and angle of craters), for the four possible variations I, II, III and IV.*

## 6.2 Light scattering on etched-*ZnO/Ag* reflectors

On the etched-*ZnO* layers with different surface morphologies, an around 200 *Ag* layer was deposited by sputtering. The light-scattering properties of the etched-*ZnO/Ag* reflectors were investigated, in terms of the haze and angular intensity distribution *AID*. The relationship between the light-scattering properties for the reflection and the surface morphology will be analysed, in terms of the rms roughness, the mean diameter and angle of craters and flat area on the surface.

### 6.2.1 Haze

**Effects of the etching time and *ZnO* thickness on the haze of reflectors**

The haze of the etched-*ZnO/Ag* reflectors with the varied etching time is shown in Figure 6.8 versus the wavelength of the incident light, for different as-deposited *ZnO* thicknesses of (a) 550 nm, (b) 800 nm and (c) 1050 nm. In general, the haze changes with the wavelength of the incident light and is significantly influenced by both the etching time and as-deposited *ZnO* thickness. Except for three over-etched samples, the haze drops with the light wavelength and most of the samples have very high haze (close to 1) at $\lambda$ = 300 nm.

For a given wavelength of the light and as-deposited *ZnO* thickness, the haze firstly increases with increasing the etching time and then decreases due to over-etching the samples down to the substrates. The changes in the haze with the etching time are stronger at longer wavelengths. For example, for the samples with an as-deposited thickness of 800 nm (see Figure 6.8 (b)), the change in the haze is only around 9% at the wavelength of 300 nm, whereas it is around 55% at the wavelength of 1100 nm.

In addition, the haze is also influenced by the as-deposited thickness of *ZnO* layers. The haze in the case of the 1050 nm thick *ZnO* layers is generally higher than in the case of the other thinner *ZnO layers*. At a given wavelength and etching time, the haze increases with the as-deposited *ZnO* thickness. For example, at $\lambda$ = 800 nm, the haze value of the samples with etching time of 20 s (shown as red lines in Figure 6.8) increases from 0.66 to 0.97 with an increase in the ZnO thickness from 550 nm to 1050 nm.

In brief, the haze of etched-*ZnO/Ag* reflectors can be significantly influenced by the wavelength of the incident light, the etching time and as-deposited *ZnO* thickness. The relationship between the haze and the surface morphology of the reflectors will be analysed in

the following. For the analysis, the same morphologies are assumed for the etched-*ZnO/Ag* reflectors as for the etched-*ZnO* layers.

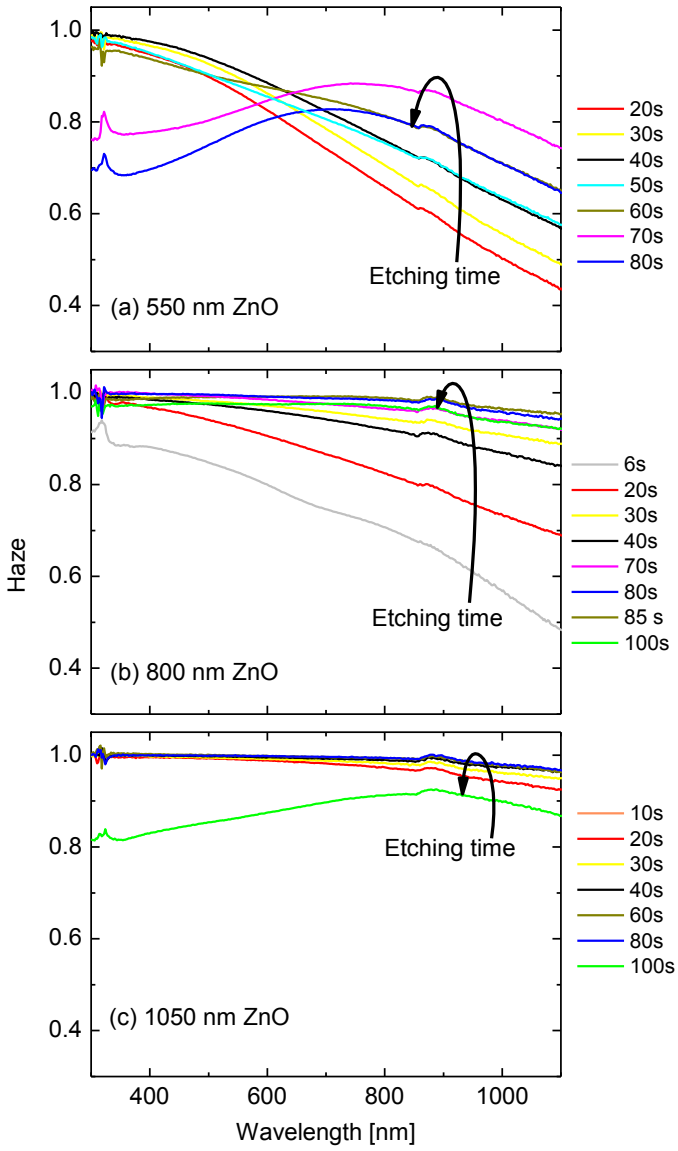


*Figure 6.8 The haze of etched-ZnO/Ag reflectors prepared with varied etching time, for different as-deposited thicknesses of ZnO layers: (a) 550 nm, (b) 800 nm and (c) 1050 nm. The arrows indicate the variation trends of the haze with the etching time.*

## Relationship between the haze and the surface morphology

### i. Haze vs. rms roughness

In Section 2.3, we have introduced the simulation models based on the scalar scattering theory, in which the haze is determined by the rms roughness $\delta_{rms}$ of surfaces. However, in the model where the $\delta_{rms}$ is used as the only parameter to determine the surface morphology, a disagreement between the calculations and measurements was found for certain surface morphologies [124]. This disagreement may be attributed to the deviation of the investigated surface morphologies from the Gaussian height distribution [81], which is assumed in this model for all surfaces. For the surfaces like etched *ZnO*, a fitting factor $C_R(\lambda)$ was suggested to be used to accommodate the deviations [81,86]. With the $C_R(\lambda)$, the haze for the reflection can be calculated by the Eq. 2.3:

$$H_R = 1 - \exp\left\{-\left[\frac{4\pi\delta_{rms} C_R(\lambda) n_1 \cos\theta_i}{\lambda}\right]^2\right\}$$

.

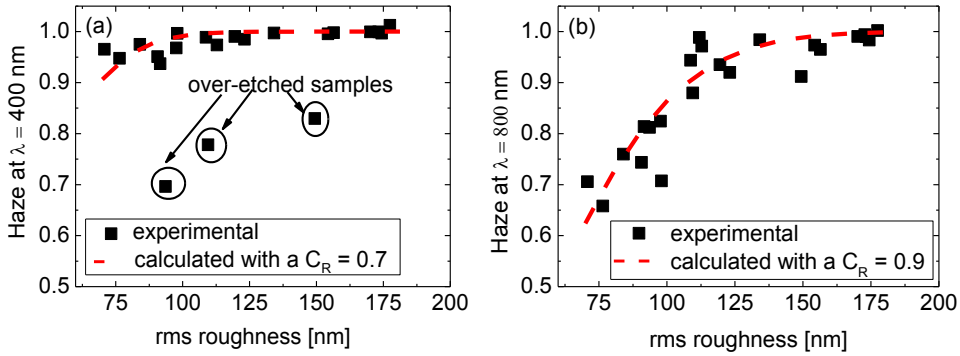


*Figure 6.9 The haze value from experiments and calculated with Eq. 6.1 as a function of the rms roughness, for the wavelengths of (a) 400 nm and (b) 800 nm*

To examine the correlation between the haze and the rms roughness, the haze of all the etched-*ZnO/Ag* reflectors from the experiments is plotted as a function of the rms roughness, for the wavelengths of 400 nm and 800 nm in Figure 6.9 (a) and (b), respectively. For comparison, the haze calculated with Eq. 2.3 is shown as the red lines in Figure 6.9, using a fitting factor of 0.7 and 0.9 for the wavelengths of 400 nm and 800 nm, respectively. It can be

seen that the calculated haze values with Eq. 2.3 are in a good agreement with the experimental results, except for three over-etched samples for $\lambda$ = 400 nm (shown with the circles in Figure 6.9 (a)). This agreement suggests that for most of the samples investigated in this study, the haze value can be determined by the rms roughness of surfaces, using an appropriate wavelength dependent fitting factor. However, it does not fit for some over etched samples, due to the exposed glass (flat) area on the surfaces. The influences of flat area on the haze of reflectors will be analysed in the following.

**ii. Haze vs. flat area on surfaces**

Figure 6.10 shows (a) the haze of etched-*ZnO/Ag* reflectors with a similar rms roughness (150 nm) of the *ZnO* layers and (b) their *AFM* images. The violet line in Figure 6.10 (a) is for the *ZnO* layer with an as-deposited thickness of 800 nm etched for 70 s, on which there is no flat area. The green line in Figure 6.10 (a) is for the *ZnO* layer with an as-deposited thickness of 1050 nm etched for 100 s, on which one can see some large flat area (shown with white arrows in Figure 6.10 (b)). The lower values on the green line in the whole wavelength range indicate that the haze of reflectors with large flat area is overall lower than the haze of reflectors with the same rms roughness without flat area.

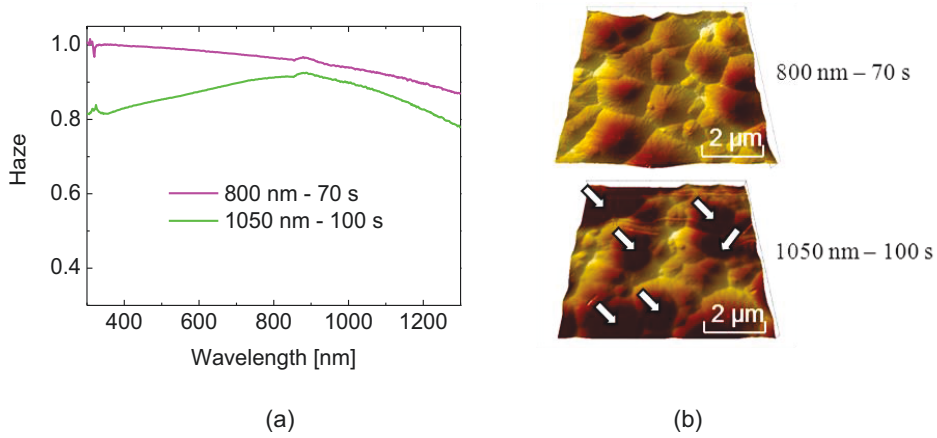


*Figure 6.10 (a) The haze of etched-ZnO/Ag reflectors with a similar rms roughness (150 nm) of the ZnO layers plotted versus the wavelength of the incident light. (b) The AFM images of the etched ZnO surfaces. Some flat areas on the ZnO surface with an as-deposited thickness of 1050 nm etched for 100 s are indicated by white arrows.*

To investigate the influences of flat area on the haze in more details, the *ZnO* layers with an as-deposited thickness of 550 nm etched from 30 s to 80 s are selected. Figure 6.11 shows the *AFM* images of these etched *ZnO* surfaces. With the *AFM* data, we estimated the percentage of the flat area to the total area for the surfaces and plot it versus the etching time in Figure 6.12. After 30 s etching, there is no flat area on the surface. With increasing the etching time, the flat area becomes larger. After 80 s etching, around 65 % of the surface is flat.

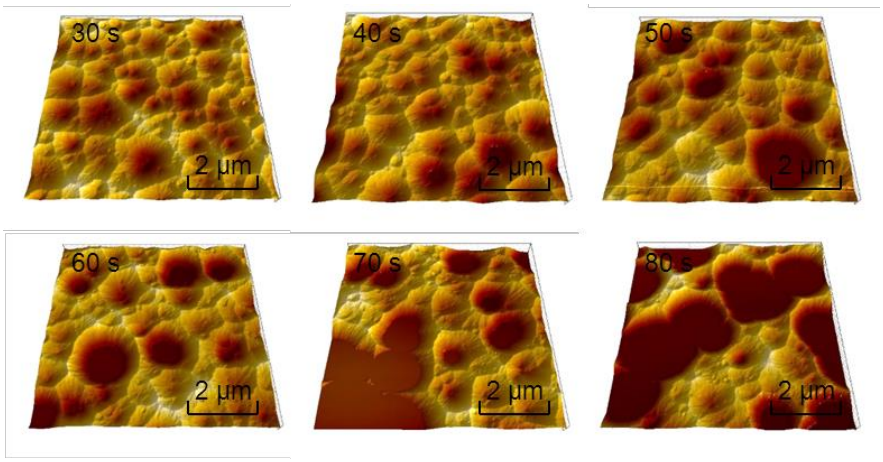


*Figure 6.11 The 3D images from AFM measurements of the ZnO layers with a 550 nm as-deposited thickness, etched from 30 s to 80 s.*

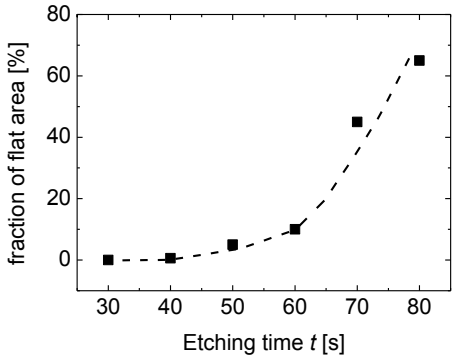

*Figure 6.12 The fraction of flat area for the ZnO layers with a 550 nm as-deposited thickness, etched from 30 s to 80 s.*

The haze of the etched-*ZnO/Ag* reflectors with the surface morphologies shown in Figure 6.11 is plotted versus the wavelength of the incident light in Figure 6.13 (a). It is noticed that the variation trend of the haze with the etching time at short wavelengths of the light is different as at long wavelengths. To see the difference clearly, the haze is plotted as a function of the etching time $t$ in Figure 6.13 (b), for two wavelengths of 400 nm and 800 nm. For $\lambda$ = 400 nm, the haze does not change much with increasing the etching time up to 60 s and decreases significantly at $t$ = 70 s, which results in around 50 % of the total surface flat (see Figure 6.12). For $\lambda$ = 800 nm, the haze increases with the etching time up to 70 s and decreases at $t$ = 80 s, results in around 65 % of the total surface flat (see Figure 6.12).

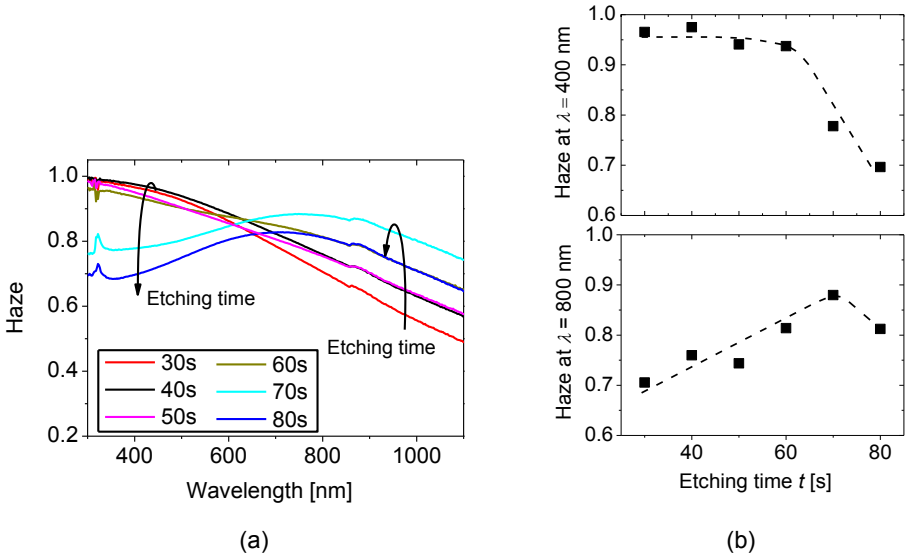


*Figure 6.13 (a) The haze curves of the etched-ZnO/Ag reflectors prepared with a 550 nm ZnO etched from 30 s to 80 s and (b) the haze at the wavelengths of 400 nm and 800 nm versus the etching time.*

**Discussion**

According to the simulation model based on the scalar theory, the haze for the reflection can be determined by the $\delta_{rms}$ of surfaces, using an appropriate correction function for the

surfaces with similar surface features. Our experimental results have a quite good agreement with the prediction of this simulation model (see Figure 6.9), except for some surfaces with large flat area. These surfaces with large flat area have much lower haze than predicted by the simulation model with the same correction function for the surfaces without flat area. It suggests that except $\delta_{rms,}$ the haze is also influenced by flat area on surfaces. This influence can be demonstrated by comparing the haze curves of two surfaces with the same $\delta_{rms}$, but one with and the other without flat area. It is found that the surface with large flat area has overall lower haze than the one without flat area (see Figure 6.10).

In addition, one can see in Figure 6.13 that the variation trends of the haze with the etching time are quite different for short and long wavelengths. The haze starts to decrease earlier for shorter wavelengths (see Figure 6.13 (b)), which indicates a wavelength dependence of the impact of flat area. Surface structures are optically rough as long as the flat area is smaller than the wavelength. Therefore, the haze starts to decrease with smaller flat area for shorter wavelengths. Moreover, one can see in Figure 6.13 (b) that with increasing the etching time from 30 s to 60 s, the haze keeps almost constant for a short wavelength like 400 nm, while it increases for a long wavelength like 800 nm. This difference can result from the wavelength dependence of haze values and the combined impacts of the flat area and rest part of the surfaces. On one hand, with increasing the etching time, the flat area increases. An increase in flat area would reduce the haze, according to what we have concluded above from our experiments. On the other hand, the $\delta_{rms}$ of the rough surface increases with the etching time, which would improve the haze, according to the simulation model and the experimental results shown in Figure 6.9. We assume that the impact of the rough part on the haze is dominant when the flat area on a surface is still small and with increasing the flat area, the impact of the flat area plays more important role and becomes dominant. With this assumption, we can explain the different variation trends of the haze for short and long wavelengths as follows: For a short wavelength like 400 nm, the haze is already close to 1 for the surface with a relative small $\delta_{rms}$ (like the *ZnO* surface etched for 30 s). An increase in the $\delta_{rms}$ cannot lead to even higher haze any more. Thus, the haze keeps almost constant (close to 1) with increasing the etching time until flat area is large enough to have a dominant impact on the haze. For a long wavelength like 800 nm, the haze of a surface with a relative small $\delta_{rms}$ is still far below 1 and has potential to be improved. Thus, the haze firstly increases with the etching time due to an increase in the $\delta_{rms}$ of the rough part of the surfaces. After the flat area is large enough to have a dominant impact on the haze, the haze starts to decrease with increasing the size of flat area.

## 6.2.2 Angular Intensity Distribution *AID*

**Effects of the etching time and *ZnO* thickness on the *AID* of reflectors**

The angular intensity distributions *AID* of the etched-*ZnO/Ag* reflectors are measured by using a laser beam with $\lambda$ = 550 nm. Figure 6.14 shows the *AID*s with the varied etching times, for three different as-deposited *ZnO* thicknesses of (a) 550 nm, (b) 800 nm and (c) 1050 nm. The variation trends of the peak position of the *AID*s with the etching time *t* are shown with black arrows. For a given *ZnO* thickness, the peak position of the *AID*s shifts firstly to larger angles with increasing the etching time, then keeps almost constant for certain etching time and shifts to smaller angles due to the flat area on the over-etched samples. In addition, one can also see that the angular intensity distribution is influenced by the as-deposited *ZnO* thickness. For example, for a given etching time of 40 s, the peak position of the *AID*s (shown as black lines in Figure 6.14) shifts significantly from around 30° to 55°, with increasing the *ZnO* thickness from 550 nm to 1050 nm.

In brief, the angular intensity distribution of etched-*ZnO/Ag* reflectors is significantly influenced by both the etching time and as-deposited *ZnO* thickness. To understand the influences, the links between the *AID* of etched-*ZnO/Ag* reflectors and its surface morphology will be analysed and presented in the following. Again, the same morphologies are assumed for the etched-*ZnO/Ag* reflectors as for the etched-*ZnO* layers for the analysis.

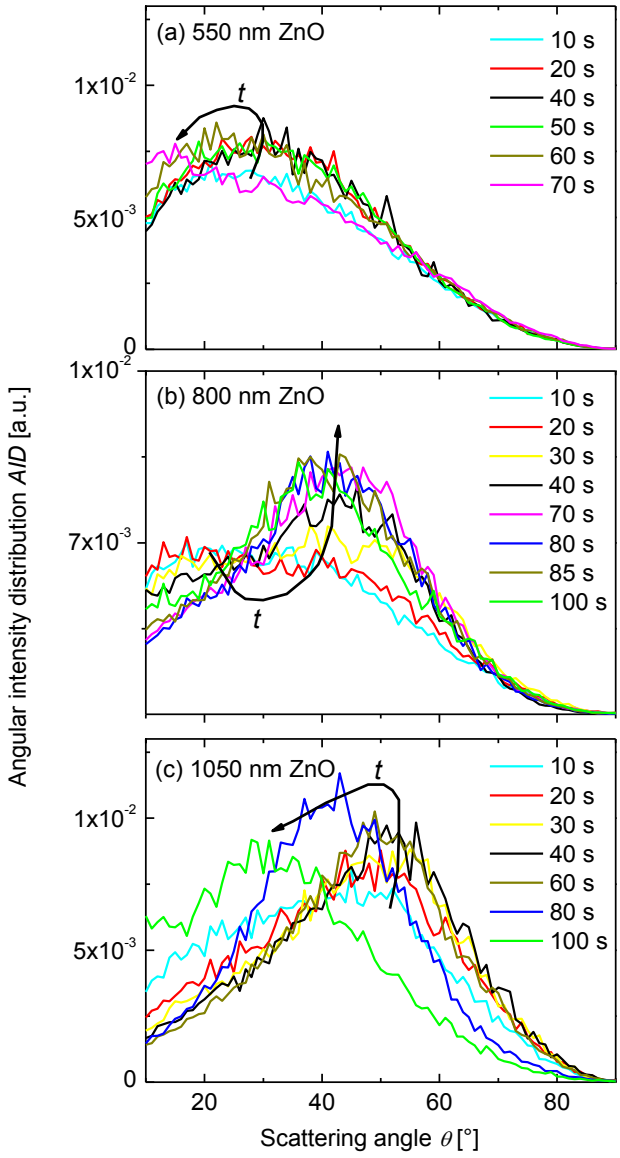


*Figure 6.14 The angular intensity distributions AID of the etched-ZnO/Ag reflectors prepared with varied etching time, for different as-deposited thicknesses of ZnO layers: (a) 550 nm, (b) 800 nm and (c) 1050 nm. The variation trends of the peak position of AIDs with the etching time are shown with black arrows.*

### Relationship between angular intensity distribution *AID* and surface morphology

#### i. Angular intensity distribution vs. rms roughness

In Section 6.2.1, we found that the haze of etched-*ZnO/Ag* reflectors can be determined by the rms roughness $\delta_{rms}$, except for the samples with very large flat area on the surfaces. To examine the relationship between the angular intensity distribution of reflectors and the rms roughness, the peak position of *AID*s is plotted versus $\delta_{rms}$ in Figure 6.15 (a) for all the samples. One can see that the peak position trends to shift to larger angles with increasing the rms roughness, as shown with the dashed line in Figure 6.15 (a). Although the peak position of *AID*s seems to have a positive correlation with the rms roughness, the samples with the same $\delta_{rms}$ may have quite different angular intensity distributions, such as the *AID*s of the samples with the same $\delta_{rms}$ of 150 nm shown in Figure 6.15 (b).

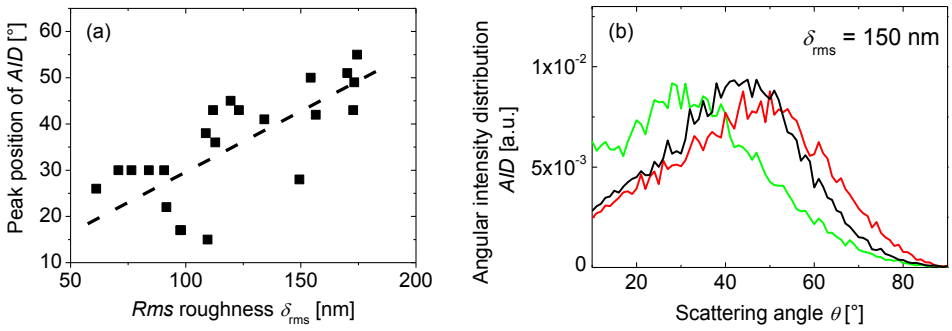


*Figure 6.15 (a) The peak position of AIDs as a function of the rms roughness and (b) the AIDs of three samples with the almost same rms roughness of 150 nm. The dashed line in (a) indicates the general variation trend of the peak position with the rms roughness.*

The results shown in Figure 6.15 both (a) and (b) suggest that the $\delta_{rms}$ alone cannot determine the angular intensity distribution of reflectors and a more detailed description of the surface morphology in terms of the diameter $d$, depth $h$ and angle $\alpha$ of craters may be necessary. In the following, the influences of the crater size (diameter $d$ and depth $h$) and crater angle $\alpha$ on the *AID* of reflectors will be analysed.

**ii. Angular intensity distribution vs. crater size**

To examine the relationship between the angular intensity distribution and crater size (diameter *d* and depth *h*) of the reflectors, samples with the same as-deposited *ZnO* thickness of 800 nm but different etching time from 10 s to 70 s are selected. As described in Subsection 6.1.3 for the first surface morphology variation, the mean diameter $d_{mean}$ and depth $h_{mean}$ of the craters on these samples increase with increasing the etching time, while the crater angle $\alpha$ is similar. This type of variation of the surface morphology is schematically shown in Figure 6.16 (a).

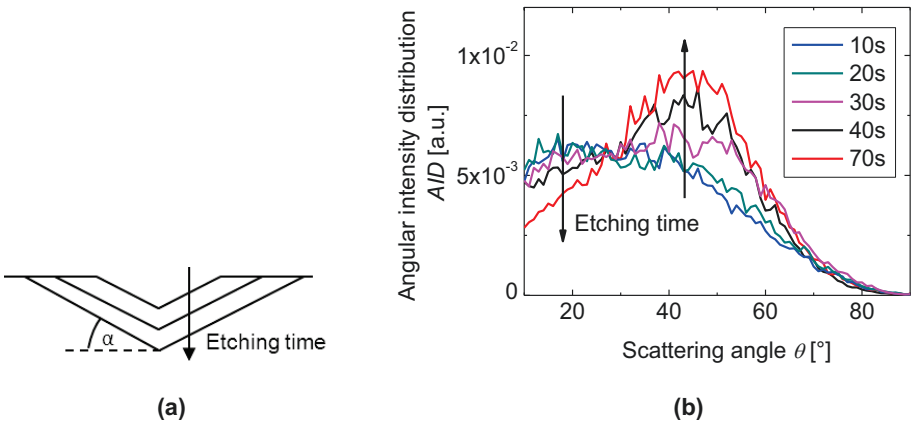


*Figure 6.16 (a) Schematic diagram of the surface morphology variation and (b) the angular intensity distributions of the selected samples with varied crater sizes but similar crater angle α of around 25°. The arrow in (a) indicates the variation trend of the surface morphology with the etching time, while the arrows in (b) indicate the variation trends of the angular intensity distribution with the etching time.*

The angular intensity distributions of the selected samples are shown in Figure 6.16 (b). The following changes in the *AID* can be seen with increasing the etching time (crater size): (1) the light intensity at small scattering angles ($\theta < 30°$) decreases, while it increases at large angles ($\theta > 30°$). (2) The peak position of *AID*s shifts from around 25° to 41° with increasing the etching time from 10s to 30 s and is located almost at the same scattering angle of around

41° for t > 30s. (3) The maximum value of *AID*s increases with increasing the etching time and the *AID* becomes narrower.

### iii. Angular intensity distribution vs. crater angle

As described in Subsection 6.1.3 for the second type *II* of the surface morphology variation, the crater angle $\alpha$ can be enlarged with increasing the as-deposited *ZnO* thickness, while the mean crater diameter can be kept almost constant by adjusting the etching time. To examine the relationship between the angular intensity distribution of reflectors and the crater angle $\alpha$, we select three samples here with almost the same mean crater diameter of 850 nm (shown as sample *A*, *B* and *C* in Figure 6.3) but the different crater angles from ~ 20° to ~ 30° (see Table 6.1). The surface morphology variation of the selected samples is schematically shown in Figure 6.17 (a).

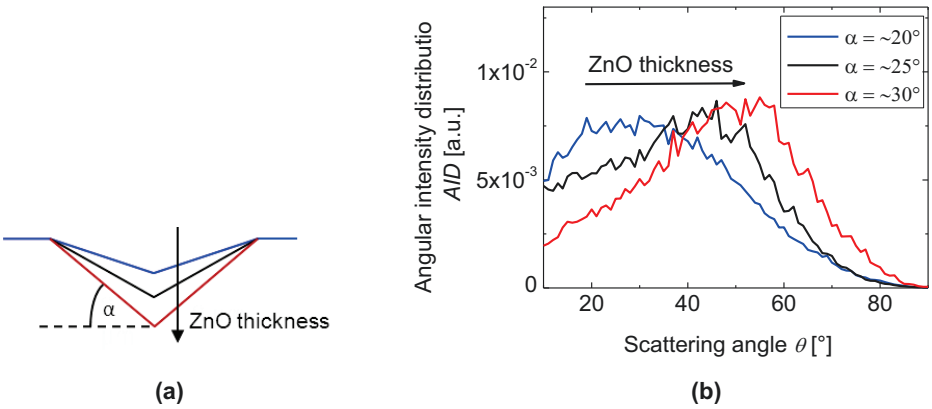


*Figure 6.17 (a) Schematic diagram of the surface morphology variation and (b) the angular intensity distributions of the selected samples with varied crater angles and almost the same mean crater diameter of around 850 nm. The arrow in (a) indicates the variation trend of the surface morphology with the ZnO as-deposited thickness, while the arrows in (b) indicate the variation trends of the angular intensity distribution with the ZnO as-deposited thickness.*

Figure 6.17 (b) shows the angular intensity distributions of the selected samples with different crater angles. It can be seen that the *AID* shifts to larger scattering angles with increasing the crater angle $\alpha$. The peak position of the *AID*s varies significantly from around 30° to around 55° with increasing the crater angle α from around 20° to around 30°.

In the third surface morphology variation (see Table 6.1), both the angle $\alpha$ and mean diameter $d_{mean}$ of craters change, while the mean crater depth $h_{mean}$ is kept constant. Since the change in the mean crater diameter will also have an impact on the *AID*s according to the diffraction grating model (introduced in Section 2.4), the relationship between the *AID* and crater angle cannot be directly examined with this surface morphology variation. Thus, in this thesis, the effects of this surface morphology variation on the *AID* is not analysed.

**iv. Angular intensity distribution vs. flat area on surfaces**

It has been found in Section 6.2.1 that large flat area can lead to lower haze for the reflection. In the following, the influences of flat area on the angular intensity distribution will be investigated. For this investigation, samples with a *ZnO* thickness of 550 nm and different etching time from 40 s to 70 s are selected. The thinnest *ZnO* was used for this investigation since the glass substrate in this case is revealed quite fast with the etching time. The *AFM* images and the fraction of the flat area of these etched *ZnO* surfaces have already shown in the last subsection (Subsection 6.2.1) in Figure 6.11 and Figure 6.12, respectively. After 40 s etching, there is only small flat area on the surface (below 5% of the total surface). With increasing the etching time, the flat area becomes larger. After 70 s etching, around 50 % of the surface is flat.

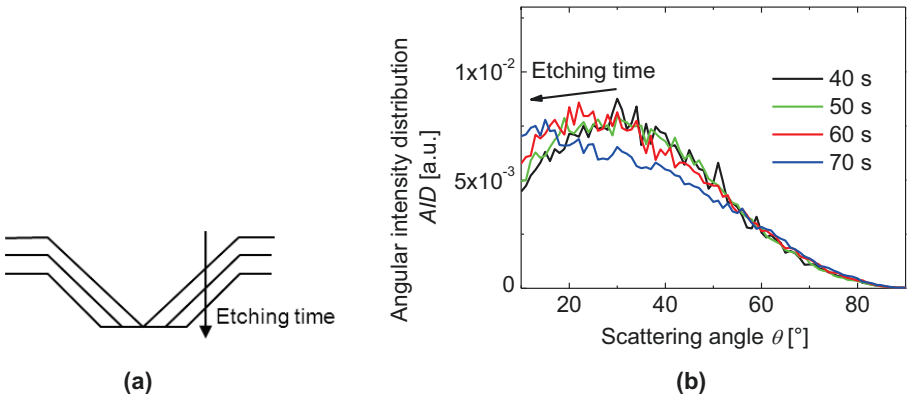


*Figure 6.18 (a) Schematic diagram of the surface morphology variation and (b) the angular intensity distributions of the selected samples with different flat area. The arrow in (a) indicates the variation trend of the surface morphology with the etching time, while the*

*arrows in (b) indicate the variation trends of the angular intensity distribution with the etching time.*

Figure 6.18 shows (a) the schematic diagram of the surface morphology variation and (b) the angular intensity distributions of the selected samples. The *AID*s are not changed with increasing the etching time from 40 s to 50 s. With a further increase in the etching time from 50 s up to 70 s, the peak position of *AID*s shifts from around 30° to 15°.

**Discussion**

According to the variation in the *AID* with the diameter $d$ and angle $\alpha$ of craters shown above, the mechanisms of the light scattering for the reflection will be discussed in the following, in terms of the diffraction and geometric optics.

**(1) Diffraction**

In the so-called grating model introduced in Section 2.3, the *ZnO* surface profile is described as a superposition of periodic gratings. Due to the local periodicities in the surface profile, the incident light can be diffracted into the zeroth order (specular light) or higher orders (diffuse light). Therefore, the angular intensity distribution *AID* can be determined by the lateral size of features (the crater diameter) on a surface. Although diffraction is possible into different orders, for simplification, only diffraction into the first order was taken into account in this grating model. A quite good agreement was found in Ref. [83] between the simulated and experimental results of the *AID* for the transmission through the *ZnO*/air interface. Both the experimental results in Ref. [83,120] and simulated results in Ref. [83] show that with increasing the mean crater diameter (the etching time), the peak position of the *AID* for the transmission through the *ZnO*/air interface shifts to smaller angles.

The same variation trend of *AID* for the reflection is predicted by the grating model based on diffraction of the incident light. However, from the experimental results (see Figure 6.16), we found that with increasing the mean crater diameter (the etching time), the peak position of *AID*s for the reflection shifts firstly to larger angles and then keeps almost constant. The disagreement between the experimental results and the prediction of the grating model can result from the unfulfilled assumption in the grating model, in which only the first order is taken into account. For the reflection, the light travels through the rough region of textured surfaces twice and the higher orders may have more impact than for the case of transmission where the light travels through the rough region only once.

In conclusion, the variation of *AID* for the reflection with the crater diameter cannot be explained by diffraction alone and other mechanisms, such as geometrical optics may also have impact on the variation.

**(2) Geometrical optics**

The geometrical optics (ray optics) describes light propagation in terms of a ray. For simplification, optical effects such as diffraction and interference are not taken into account in the geometrical optics. Figure 6.19 shows the schematic diagram of the reflection on a crater based on the geometric optics. Here, the crater wall is considered as a plane surface with an angle of $\alpha$ to the substrate. According to the law of the specular reflection, the angle between the reflected ray and the surface normal is the same as that between the incident ray and the normal. Therefore, the angle between the specular reflected light on a crater wall and the incident light $\theta_{geo}$ should be twice the crater angle α ($\theta_{geo} = 2\ \alpha$). Thus, for the samples with a crater angle $\alpha$ of 20°, 25° and 30°, the $\theta_{geo}$ should be 40°, 50° and 60°, respectively.

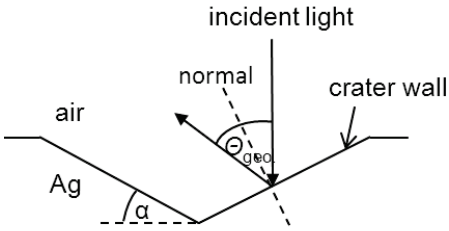


*Figure 6.19 Schematic diagram of the specular reflection on a crater based on the geometrical optics*

The experimental results show that for the reflectors with a mean crater diameter of around 850 nm, the *AID* shifts to larger scattering angles with increasing the crater angle $\alpha$. The peak position of the *AID*s is located at the scattering angle $\theta$ of around 30°, 43° and 55° for the crater angle $\alpha$ of around 20°, 25° and 30°, respectively (see Figure 6.17). The shift of the *AID*s with the crater angle $\alpha$ is in good agreement with the prediction of the geometric optics, although the scattering angle $\theta$ at the peak position of the measured *AID*s is a little smaller that the $\theta_{geo}$ calculated with the law of specular reflection. This difference might result

from *AFM* measurement errors or a slight smoothing effect by sputtering 200 nm *Ag* layers on etched-*ZnO* layers, which has been observed in the past [120].

**(3) Combination of diffraction and geometrical optics**

For all the etched-*ZnO/Ag* reflectors measured in this study, the peak position of the *AID*s is plotted in Figure 6.20 as a function of the mean crater diameter $d_{mean}$, for the samples with the different crater angles of 20°, 25° and 30°. For a given crater angle, the peak position of *AID*s seems to shift to larger angle with increasing the $d_{mean}$ up to a certain value and get into a saturation with a further increase in the $d_{mean}$. This effect can be seen clearly for the reflectors with a similar crater angle of around 25° (black points). For these reflectors, the peak position of *AID*s shifts from around 17° to 43° with increasing $d_{mean}$ from around 650 nm up to 850 nm and keeps almost constant for $d_{mean} > 850$ nm. Moreover, in the saturation region, the peak position of *AID*s shifts from around 30° to 55° with increasing the crater angle $\alpha$ from around 20° to 30°.

These variations in the peak position of *AID*s with the $d_{mean}$ and $\alpha$ are attributed to the combined impacts of diffraction and geometrical optics. When the mean crater diameter is small, diffraction has a dominant impact on the *AID*. In this case, the *AID* is mainly influenced by the diameter and periodicity of craters. With increasing the mean crater diameter, the geometrical optics plays more important role and turns into the dominant physical mechanism for light scattering. In the latter case, the *AID* is mainly influenced by the crater angle, which can explain the shift of the *AID* peak position with the crater angle in the saturation region observed in Figure 6.20. The shift of the *AID* peak position with the $d_{mean}$ can be considered as transition between two dominant physical mechanisms: diffraction and geometrical optics.

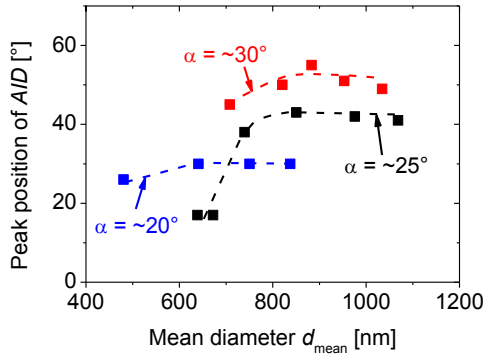


*Figure 6.20 The peak position of AIDs plotted as a function of the mean diameter $d_{mean}$, for the samples with different crater angles of 20° (blue), 25° (black) and 30°(red).*

All the discussions above are based on the measurements in air with one wavelength of the incident light (550 nm). One has to be aware that the variation trends may be different if the refractive index of media or the wavelength of the incident light changes. Which mechanism, whether diffraction or geometrical optics, plays the dominant role for light scattering depends on not only the crater diameter, but also the effective wavelength of the light in a medium. For the case that most of the craters have much smaller diameters than the effective light wavelength, diffraction may play the dominant role for light scattering. In this case, the crater diameter is the most important parameter for the light scattering. According to the diffraction grating model, the smaller is the crater diameter, the larger is the scattering angle. However, this effect of the crater diameter could not be examined with our experimental results since even smaller craters which are homogenously cover the whole surface could not be formed by etching *ZnO* with *HCl* solution. On the other hand, for the case that most of the craters are much larger diameters than the effective light wavelength, geometrical optics may play the dominant role for light scattering. In this case, the crater angle is the most important parameter for the light scattering. The larger is the crater angle, the larger is the scattering angle. This effect of the crater angle was observed by our results (see Figure 6.17 and Figure 6.20).

The light-scattering properties of back reflectors in silicon cannot be measured. In this work, *AID*s in silicon were simulated with the so-called phase model and will present in the next section. Moreover, in the next section, the link between the *AID*s (both measured in air and simulated in silicon) and the light trapping in solar cells will be analysed.

## 6.3 Light trapping in solar cells

In the previous section, we analysed the effects of the surface morphology of etched-*ZnO/Ag* reflectors on their light-scattering properties measured in air (the haze and *AID*). In this section, the effects of the surface morphology of etched-*ZnO/Ag/ZnO* back reflectors on the performance of *μc-Si:H n-i-p* solar cells will be firstly presented. Then, we will discuss the relationship between the light-scattering properties of the back reflectors and light trapping in solar cells. Moreover, the light trapping processes in solar cells will be investigated by simulated angular intensity distributions in *μc-Si:H* ($AID_{Si}$). Finally, the link between the surface morphology of the back reflectors and the light trapping in the solar cells will be analysed.

### 6.3.1 Effects of the back reflector surface morphology on the solar cell performance

The *μc-Si:H n-i-p* solar cells were prepared on the etched-*ZnO/Ag/ZnO* back reflectors with the different surface morphologies by varying the etching time and as-deposited thickness of the etched-*ZnO* layers. All the solar cells are around 1.1 μm thick and were prepared with the constant deposition conditions for the silicon and front contact layers. More details about the preparation of the *μc-Si:H n-i-p* solar cells were introduced in Chapter 3.

**The solar cell performance from I-V measurements**

Figure 6.21 shows the performance of *μc-Si:H n-i-p* solar cells from *I-V* measurements: (a) the cell efficiency $\eta$, (b) open circuit voltage $V_{OC}$, (c) fill factor *FF* and (d) short circuit current density $J_{SC}$ as a function of the etching time of the etched-*ZnO* layers, for different as-deposited *ZnO* thicknesses of 550 nm, 800 nm and 1050 nm. All the solar cells with textured back reflectors (using *ZnO* etched from 10 s to 100 s) work on a high level, with a cell efficiency above 7.4%. The open circuit voltage and fill factor of all the solar cells are quite similar: the $V_{OC}$ is around 504 ± 5 mV and the *FF* is around 70.5 ± 0.9%. Considering the performance of solar cells, the main effect of the morphology of these back reflectors is on the short circuit current density, which varies significantly within ~33% (from around 18 mA/cm$^2$ to 24 mA/cm$^2$) over the investigated range. It is noticed that the $J_{SC}$ varies with both the etching time and as-deposited thickness of the *ZnO* layers, which can be related to the change

in the surface morphology of the back reflectors. The link between the morphology of the back reflectors and the $J_{SC}$ will be analysed in Section 6.3.3 in details.

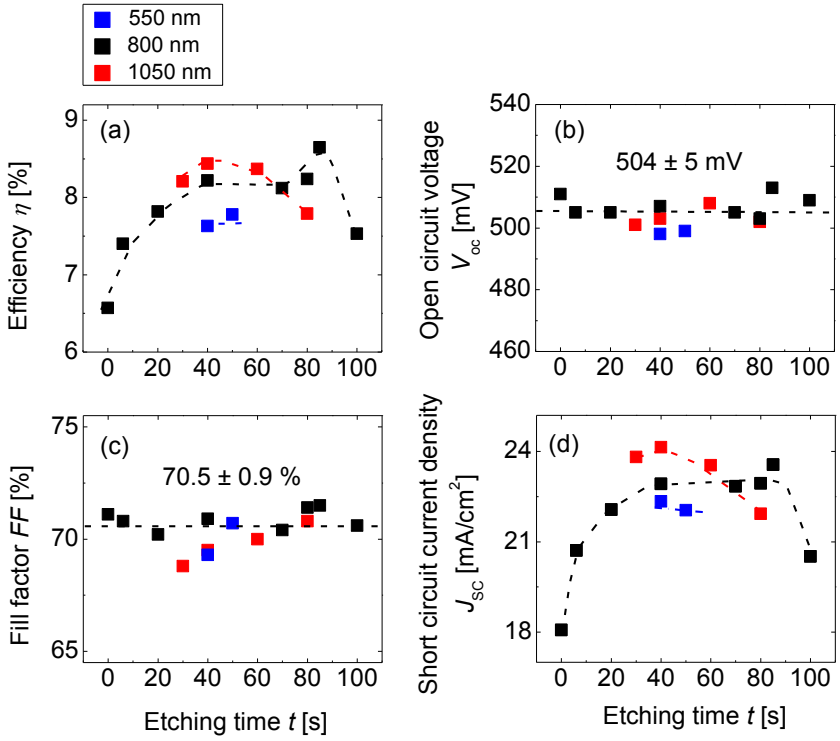


*Figure 6.21 (a) The cell efficiency, (b) open circuit voltage, (c) fill factor and (d) short circuit current density of the solar cells as a function of the etching time of the etched-ZnO layers, for different as-deposited ZnO thicknesses of 550 nm, 800 nm and 1050 nm.*

**The quantum efficiency**

The quantum efficiency *QE* of the solar cells was measured to analyse the effects of the back reflector morphology on the short circuit current density in more details. The *QE* of three solar cells is plotted exemplarily as a function of the wavelength of the incident light in Figure 6.22 (a). The green, orange and violet lines represent the *QE* of the solar cell with the lowest, middle and highest $J_{SC}$, respectively. A significant difference in *QE* can be seen in the long wavelength range, while the *QE* in the short wavelength range varies slightly. These effects of the back reflector morphology on the *QE* of the solar cells can be more clearly seen in Figure 6.22 (b) and (c), where the integrated *QE* current density $J_{ph}$ of all the solar cells is

plotted versus the etching time, for $\lambda$ = 300 ~ 600 nm and $\lambda$ = 600 ~ 1100 nm, respectively. The integrated *QE* current density $J_{ph}$ is calculated with the AM1.5 spectrum and *QE* in the given wavelength ranges. It can be seen that the integrated *QE* current density in the short wavelength range ($\lambda$ = 300 ~ 600 nm) increases slightly from around 9.6 to 10.5 mA/cm$^2$ with increasing the etching time from 0 up to 100 s. On the other hand, the integrated *QE* current density in the long wavelength range ($\lambda$ = 600 ~ 1100 nm) varies significantly from around 8.5 to 14.2 mA/cm$^2$ for the investigated samples. It is noticed that the variation trends of the integrated *QE* current density in the long wavelength range with the etching time and *ZnO* thickness are quite similar as that of the $J_{SC}$ shown in Figure 6.21 (d). This indicates that the change in the $J_{SC}$ with the back reflector surface morphology can be mainly attributed to the change in the spectral response of solar cells in the long wavelength range.

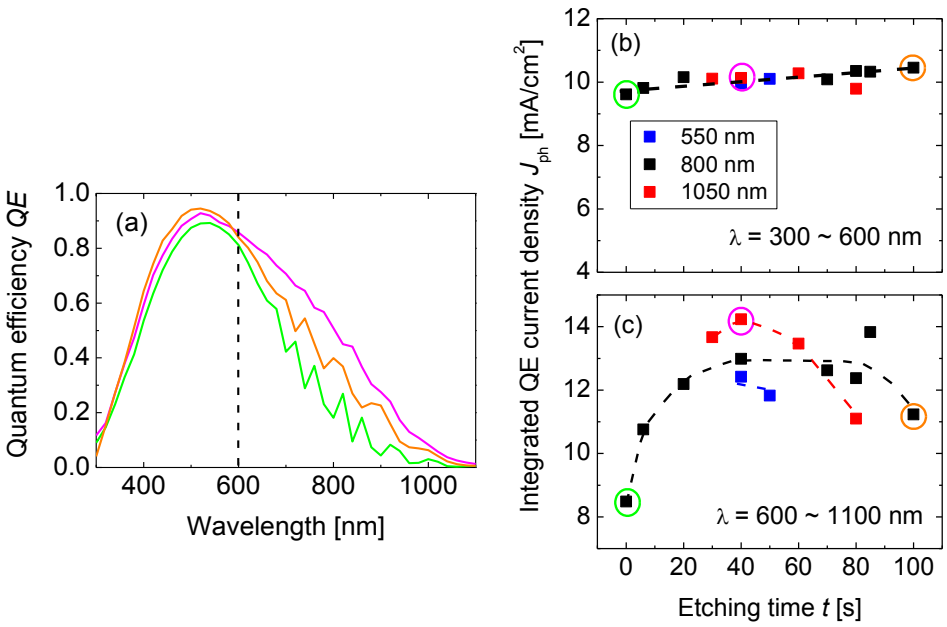


*Figure 6.22 (a) The quantum efficiency QE of three µc-Si:H n-i-p solar cells plotted exemplarily versus the wavelength of the incident light. The green, orange and violet lines represent the QE of the solar cell with the lowest, middle and highest Jsc, respectively. (b) and (c) show the integrated QE current density $J_{ph}$ of all the solar cells versus the etching time, for $\lambda$ = 300 ~ 600 nm and $\lambda$ = 600 ~ 1100 nm, respectively. The $J_{ph}$ of the three solar cells shown in (a) are marked by circles with the correlated colours.*

**The total cell reflectance**

The total cell reflectance $R_{total}$ of the solar cells was measured and is show exemplarily in Figure 6.23 (a) for the three solar cells with the lowest, middle and highest $J_{SC}$. One can see a very slight difference in the $R_{total}$ in the short wavelength range and a significant difference in the long wavelength range.

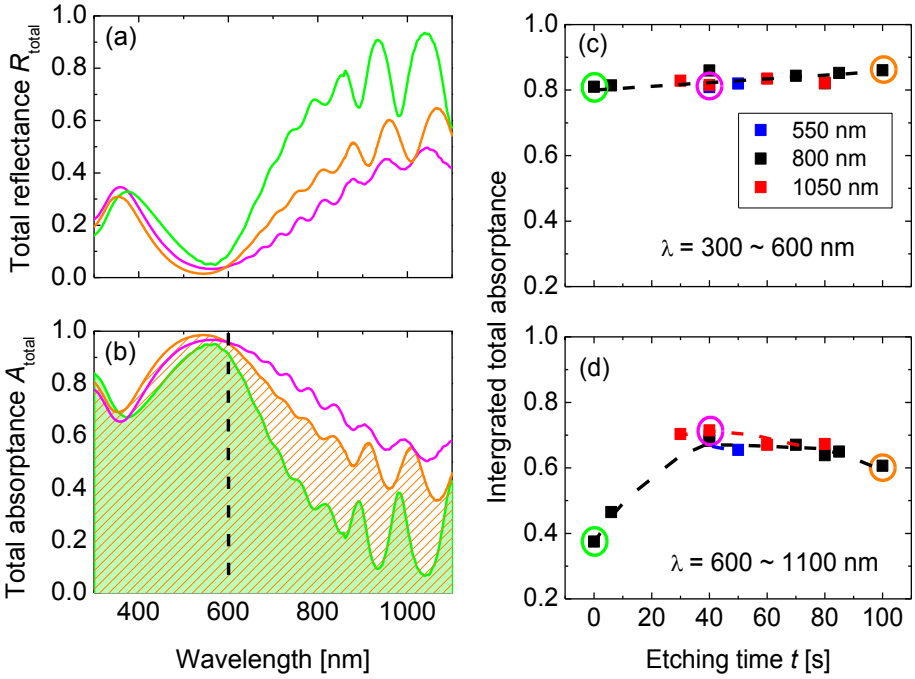


*Figure 6.23 (a) and (b) show the total reflectance $R_{total}$ and absorptance $A_{total}$ of three µc-Si:H n-i-p solar cells versus the wavelength of the incident light, respectively. The green, orange and violet lines represent the $R_{total}$ and $A_{total}$ of the solar cell with the lowest, middle and highest Jsc, respectively. The integrated total absorptance of all the solar cells over the short wavelength range (300~600 nm) and long wavelength range (600~1100 nm) is plotted versus the etching time in (c) and (d), respectively.*

With the measured $R_{total}$ of the solar cells, the total absorptance $A_{total}$ can be calculated by $1-R_{total}-T_{total}$. In our case, the $T_{total}$ is equal to zero due to the highly reflective back reflectors. In Figure 6.23 (b), the total absorptance $A_{total}$ of the three example solar cells is plotted as a

function of the wavelength of the incident light. As expected, a very slight difference in the $A_{total}$ in the short wavelength range and a significant difference in the long wavelength range can be seen. To compare the $A_{total}$ of the solar cells prepared on the different back reflectors in both short and long wavelength ranges, the $A_{total}$ is integrated over the wavelengths from 300 nm to 600 nm and from 600 nm to 1100 nm. The integrated total absorptance is plotted versus the etching time in Figure 6.23 (c) and (d) for $\lambda$ = 300 ~ 600 nm and $\lambda$ = 600 ~ 1100 nm, respectively. It is found that the integrated total absorptance over $\lambda$ = 300 ~ 600 nm increases slightly with the etching time, while the integrated total absorptance over $\lambda$ = 600 ~ 1100 nm varies significantly. By using a textured back reflector with a 1050 nm thick *ZnO* layer etched for 40 s instead of a flat one, the integrated total absorptance over $\lambda$ = 600 ~ 1100 nm increases significantly from 0.37 up to 0.71. It is noticed that the variation trend of the integrated total absorptance with the etching time and *ZnO* thickness is similar as the integrated *QE* current density $J_{ph}$ of the solar cells shown in Figure 6.22 (b) and (c).

**The internal quantum efficiency**

The internal quantum efficiency *IQE* of solar cells is calculated by $IQE = QE / (1-R_{total})$. Figure 6.24 (a) shows exemplarily the *IQE* of the three solar cells with the lowest, middle and highest $J_{SC}$ with a green, orange and violet line, respectively. One can see that the *IQE* curves are quite similar in the short wavelength range, while they have quite different amplitudes of interference in the long wavelength range. The different amplitudes are attributed to different phase shift between the *QE* and $R_{total}$ curves which are used to calculate the *IQE*s. The phase shift between the *QE* and $R_{total}$ curves results from different laser beams and measuring places of the solar cells for these two measurements.

To compare the *IQE* of solar cells with each other, the *IQE* of all the solar cells is integrated over the wavelengths from 300 nm to 600 nm and from 600 nm to 1100 nm and plotted versus the etching time in Figure 6.24 (b) and (c), respectively. It is found that the integrated *IQE*s of all the solar cells are quite similar for both the short and long wavelength range. The integrated *IQE*s over $\lambda$ = 300 ~ 600 nm are all around 0.75, while the integrated *IQE*s over $\lambda$ = 600 ~ 1100 nm are all close to 0.5.

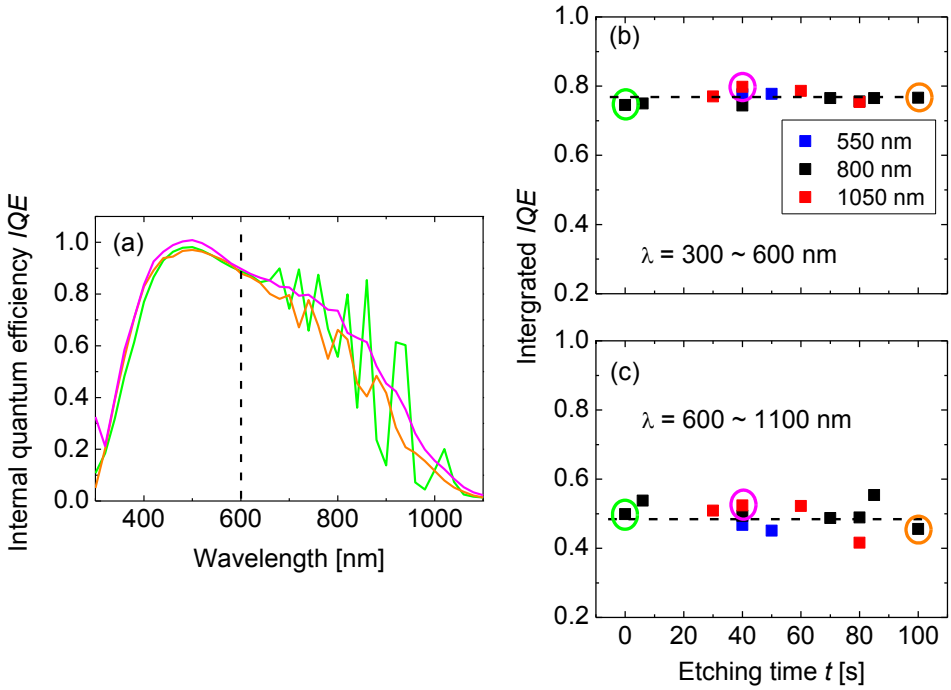


*Figure 6.24 (a) Internal quantum efficiency IQE curves of three μc-Si:H n-i-p solar cells versus the wavelength of the incident light, respectively. The green, valet and orange line represent the IQE of the solar cell with the lowest, middle and highest Jsc, respectively. The integrated IQE of all the solar cells over the short wavelength range (300~600 nm) and long wavelength range (600~1100 nm) is plotted versus the etching time in (b) and (c), respectively.*

**Discussion**

The *I–V* measurement results show that the fill factor and open circuit voltage of the solar cells are quite similar for the solar cells with different back reflector morphologies, while the short circuit current density is significantly changed (see Figure 6.21). The change in the $J_{SC}$ is mainly attributed to the change in the spectral response of solar cells in the long wavelength range, since the change in the *QE* in the short wavelength range is much smaller (see Figure 6.22).

The *QE* in the short wavelength range increases slightly with the etching time of *ZnO* layers (see Figure 6.22 (b)), which may be attributed to an improvement in light in-coupling. It can be demonstrated by the slight increase in the integrated total absorptance over $\lambda$ = 300 ~

600 nm (see Figure 6.23 (c)). An improvement in light in-coupling with textured front *TCO* layers has been also found for *p-i-n* solar cells and related to an effective refractive index grating at the rough *TCO/Si* interface [14,119].

Possible reasons for the significant change in the *QE* in the long wavelength range with the back reflector morphology would be due to changes in: (1) the properties of the silicon layers, (2) parasitic absorption and (3) light trapping in the solar cells. From the results of Raman measurements, it is found that the silicon layers in all these solar cells have very similar crystallinity of ~70% within an error of ± 4% arising likely from background subtraction. From this together with the invariance of *FF* and $V_{OC}$ of the different cells, it can be concluded that the growth and electrical properties of silicon layers are not influenced by the back reflector morphologies used in this study. Also changes in the parasitic absorption are not the main reason for the change in *QE* based on the quite similar *IQE* of the solar cells (see Figure 6.24 (c)). This leaves us with the significant difference in $R_{total}$ in the long wavelength region (see Figure 6.23 (d)). Thus, we conclude that the change in the *QE* in the long wavelength range mainly results from the different light trapping of the solar cells with varied back reflector morphologies.

### 6.3.2 Relationship between light-scattering properties of back reflectors and light trapping in solar cells

The relationship between the light-scattering properties (the haze and *AID*) of back reflectors and the light trapping in solar cells will be analysed in the following.

**Haze of back reflectors vs. short circuit current of solar cells**

The haze is a commonly used parameter to characterize the light-scattering properties of a rough surface. In Section 6.2, we have found that the haze for the reflection depends on the surface morphology of reflectors and the wavelength of the incident light. To examine the relationship between the haze of back reflectors and the light trapping in *μc-Si:H n-i-p* solar cells, the short circuit current density of the solar cells (see Figure 6.21 (d)) is plotted in Figure 6.25 as a function of the haze for the reflection measured in air at $\lambda$ = 300 nm. The wavelength of 300 nm is chosen here for the following reason: For the *μc-Si:H* solar cell application, the typically considered wavelengths vary in a range from 300 to 1100 nm, where the refractive index of *μc-Si:H* layers ($n_{Si}$) is between 3.5 and 4 [84,118]. Thus, according to Eq 6.1, the haze for the reflection at $\lambda$ = 300 nm in air corresponds to that at a wavelength between 1050 and 1200 nm in *μc-Si:H* layers. Therefore, the haze for the reflection at $\lambda$ = 300 nm measured in air can be used to estimate the haze of the back reflectors in the *μc-Si:H* solar cells in the *NIR* region, where light trapping is crucial.

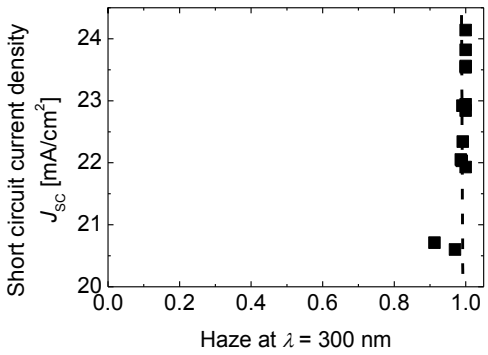


*Figure 6.25 The short circuit current density of the solar cells prepared with the different textured etched-ZnO/Ag/ZnO back reflectors plotted versus the haze of the etched-ZnO/Ag*

*reflectors measured in air at λ = 300 nm. The dashed line shows samples with the same haze close to 1.*

One can see in Figure 6.25 that all the back reflectors with different surface morphologies have very high haze at 300 nm (above 0.9), although they lead to quite different short circuit current densities. For example, the back reflectors with a haze close to 1 (under the dashed line) lead to different $J_{SC}$ from around 22 mA/cm$^2$ to 24 mA/cm$^2$. It suggests that the haze of back reflectors alone is not sufficient to estimate the light-trapping potential of *μc-Si:H n-i-p* solar cells. The light-trapping potential may be more sensitive to other quantities for light-scattering, such as the angular intensity distribution *AID*.

**Short circuit current of solar cells vs. angular intensity distribution of back reflectors**

The angular intensity distribution *AID* provides more detailed information than the haze with respect to a light scattering process since it describes the intensity of the diffuse scattered light at each angle instead of only the portion of the diffuse scattered light. The light scattered into a large angle on the back reflector may also have a large angle to the *μc-Si:H/ZnO* interface on the front side of solar cells. Only if the angle between the scattered light and the *μc-Si:H/ZnO* interface is larger than the critical angle for the total internal reflection, the light will be trapped in solar cells. Therefore, one can imagine that back reflectors with the same haze but different angular intensity distributions may result in quite different light trapping in solar cells.

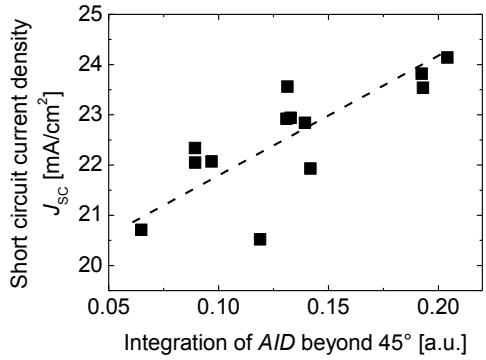


*Figure 6.26 The short circuit current density of the solar cells on the different textured back reflectors plotted versus the integration of the AIDs for the reflection measured in air for the scattering angles beyond 45°.*

To examine the relationship between the angular intensity distribution of the back reflectors and light trapping in the solar cells, the intensities of the light at the scattering angles beyond 45° are integrated for all the samples. The angles beyond 45° are chosen in this study as an example of large angles. Figure 6.26 shows the short circuit current density of the solar cells as a function of the integration of the *AID*s for the scattering angles beyond 45°. It can be seen that the $J_{SC}$ increases with the integration of *AID*s for the scattering angles beyond 45°. This positive correlation between these two parameters indicates that the light trapping in solar cells can be improved when more light is reflected into large angles, for example the angles beyond 45°.

**Investigation of the light trapping process in solar cells with simulation**

A positive correlation between the integration of the *AID*s for the scattering angles beyond 45° and the $J_{SC}$ has been found (see Figure 6.26). To understand more about this correlation and the light trapping process in solar cells, the light scattering processes at different textured interfaces in solar cells are investigated with simulations. Regarding the layer stack of a *μc-Si:H n-i-p* solar cell as shown in Figure 6.27, two main scattering interfaces exist. The first is the interface of the front contact *ZnO* and the *μc-Si:H* layer, where the transmitted light is scattered. The scattering angle for the transmission at the *μc-Si:H/ZnO* interface is defined as $\theta_{tran}$ in this thesis. The second is the back reflector, where the reflected light is scattered. The scattering angle for the reflection at the back reflectors is defined as $\theta_{ref}$. For both interfaces, the scattered light propagates inside silicon.

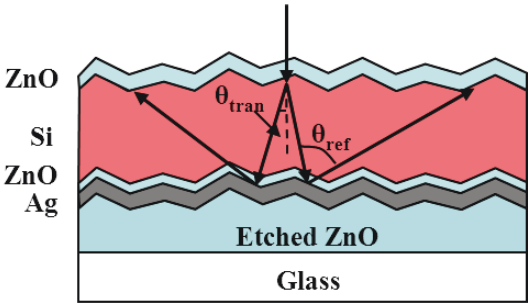


*Figure 6.27 Schematic graphic of light scattering at front and back sides in an μc-Si:H n-i-p solar cell. The scattering angle for the transmission at the μc-Si:H/ZnO interface at the front*

*side of the solar cell is defined as $\theta_{tran}$, while the scattering angle for the reflection at the back reflectors interface at the back side of the solar cell is defined as $\theta_{ref}$.*

Since the light-scattering properties inside silicon cannot be measured experimentally, the so-called phase model is used in this study to simulate the angular intensity distribution for the both interfaces in *μc-Si:H n-i-p* solar cells. Details about the phase model and the calculation of *AID*s with it have been introduced in Section 2.4.

With the phase model, the *AID*s for the transmission at a *ZnO*/air interface have been simulated by Dominé et al. [84] for different textured *ZnO* layers and a very good agreement with the experimental results has been found. To examine this model for the reflection, the *AID*s in air were firstly simulated with λ = 550 nm for different textured reflectors and compared to the experimental results.

**i. Simulation of the angular intensity distribution in air**

Figure 6.28 (a) shows the *AID*s for the reflection from both experimental and simulated results for three samples with quite different surface morphologies: (a) sample I, (b) sample II and (c) sample III. Each curve is normalized to its maximum for the sake of comparison. The *AFM* images of the three samples are shown on the right side of Figure 6.28. Sample I was prepared with a 550 nm thick *ZnO* etched for 50 s, while Sample II and III with a 1050 nm thick *ZnO* etched for 10 s and 60 s.

The angular intensity distribution varies significantly for the three samples. Sample I shows a maximum intensity at the scattering angle of 20° with a steeper slope for lower angles than for higher. Sample II has a much broader *AID* with a maximum at around 45°, while the maximum of the *AID* of sample III is found at 50° with a steeper slope for higher angles than for lower.

The experimental (solid lines) and simulated results with the phase model (dashed lines) are in very good agreement for all the 3 samples shown in Figure 6.28. The smoother shapes of the *AID*s from the experiment can be attributed to the much larger illuminated area than the sampling size (10 μm x 10 μm) in the model. Therefore, a better statistical averaging of scatterers can be achieved in experiment than in the simulation.

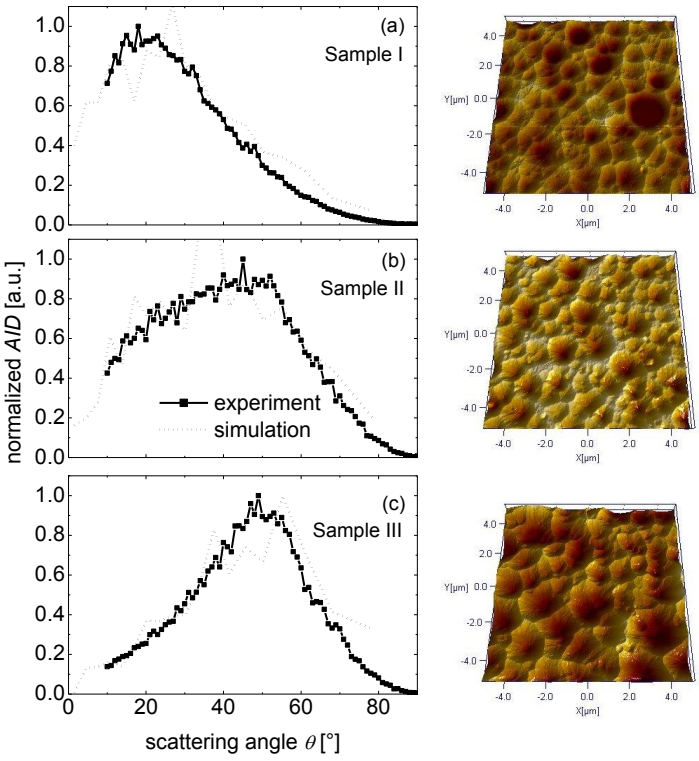


*Figure 6.28 The angular intensity distributions for the reflection in air for three samples with quite different surface morphologies (a) sample I prepared with a 550 nm thick ZnO etched for 50 s, (b) sample II prepared with a 1050 nm thick ZnO etched for 10 s and (c) sample III prepared with a 1050 nm thick ZnO etched for 60 s. The solid and dashed lines represent experimental and simulated results, respectively. The AFM images of the three samples are shown on the right side.*

**ii. Simulation of the angular intensity distribution in solar cells**

With the phase model, the angular intensity distribution in silicon $AID_{Si}$ is simulated for both the transmission at the *µc-Si:H/ZnO* interface and reflection at the back reflectors in *µc-Si:H* solar cells.

Figure 6.29 (a) shows the $AID_{Si}$ for the transmission for three samples (I, II, and III as shown in Figure 6.28) at a wavelength of 800 nm. The wavelength of 800 nm is chosen since at this wavelength the effects of light trapping in *µc-Si:H* layers are strongly pronounced. The critical angle (26.5°) for the total internal reflection at the *µc-Si:H/ZnO* interface is depicted as a vertical line in Figure 6.29 (a). When the angle between the light and the *µc-Si:H/Zn*O

interface is larger than the critical angle, the light can be fully captured inside the absorber layer. The $AID_{Si}$ for the transmission show the maximum at around 8°, 12° and 13° for sample I, II and III, respectively, which are all smaller than the total reflection angle for the *µc-Si:H/ZnO* interface.

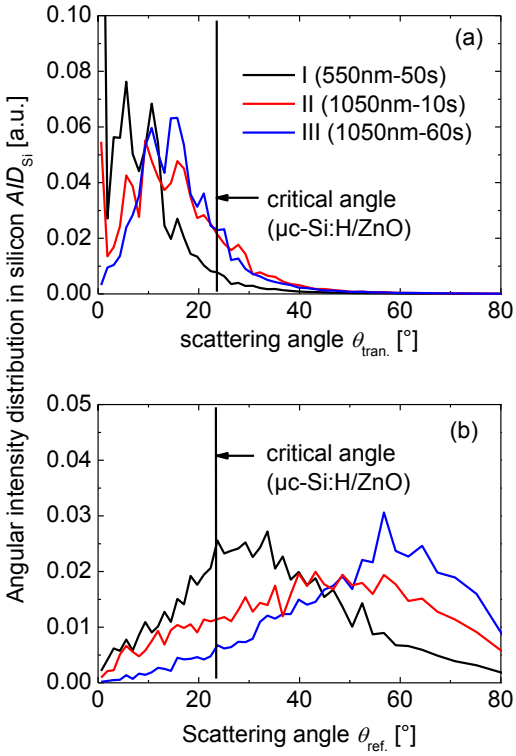


*Figure 6.29 The angular intensity distributions for a wavelength of 800 nm in silicon for (a) the transmission at the µc-Si:H/ZnO interface and (b) the reflection at back reflector, for the same samples as shown in Figure 6.28 (Sample I, II and III). The critical angle for the total reflection at the µc-Si:H/ZnO interface (26.5°) is depicted as a vertical line.*

For comparison, the $AID_{Si}$ for the reflection at the back reflectors in solar cells is simulated also at a wavelength of 800 nm and shown in Figure 6.29 (b) for the same three samples (I, II and III). It is assumed that the light irradiates perpendicular to the surface. This assumption allows the evaluation of the direct light scattering at the back reflector. Again, the

critical angle is depicted as a vertical line in Figure 6.29 (b). One can see that sample I has its maximum in the $AID_{Si}$ for the reflection at around 30°, whereas sample II and III show the highest scattering intensity at around 50° and 60°, respectively. For all these three samples, the maxima are beyond the critical angle for the *µc-Si:H/ZnO* interface. Sample III shows the largest amount of light which is scattered beyond this critical angle. Compared to the light scattering in transmission at the *µc-Si:H/ZnO* interface on the front side of solar cells, where all the maxima of the $AID_{Si}$ are located at angles below the critical angle, it can be concluded that the dominant scattering process regarding the light trapping occurs at the textured back reflectors. Moreover, the differences between the various morphologies are much more pronounced by the $AID_{Si}$ for the reflection.

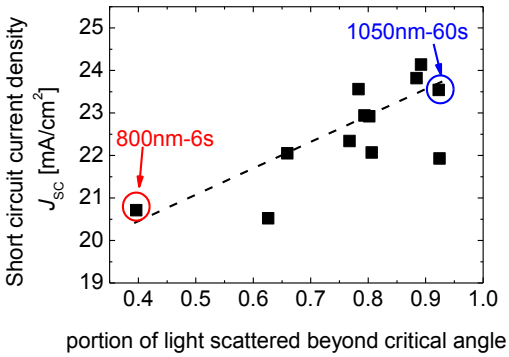


*Figure 6.30 The short circuit current density of the solar cells prepared with different textured etched-ZnO/Ag/ZnO back reflectors versus the portion of light scattered on the back reflectors beyond the critical angle for the total reflection for the µc-Si:H/ZnO interface (26.5°).*

Figure 6.30 shows the $J_{SC}$ of the solar cells versus the portion of light scattered on back reflectors beyond the critical angle for the total reflection for the *µc-Si:H/ZnO* interface (26.5°). The latter quantity is assumed to be a measure for the light trapping potential since the total reflection leads to guided optical modes in the absorber layer [125]. It is found that the short circuit current density increases in general with the portion of light scattered beyond the critical angle on the back reflector. This portion varies from 0.4 in case of the sample with 800 nm initial *ZnO* thickness and an etching time of 6 s (shown with the red circle) to 0.92 for the sample with 1050 nm initial *ZnO* thickness and an etching time of 60 s (shown with the blue circle). The latter means that more than 90% of the light scattered at the back reflector is

scattered sufficiently for light trapping by one single scattering process, whereas for the former sample this portion is only 40%. This leads to the strong variation in the short circuit current density from 20.7 mA/cm$^2$ to 23.5 mA/cm$^2$ for these two samples. The positive correlation between the $J_{SC}$ and the portion of light scattered on the back reflectors beyond the critical angle also suggests that light trapping can be improved when more light is reflected from back reflectors into large angles and the portion of light reflected beyond the critical angle can used to predict the light-trapping potential of solar cells.

**Summary**

Up to now, we have found two quantities which are well correlated to the short circuit current density of the solar cells: the integration of *AID*s of reflectors measured in air for large scattering angles, for example angles beyond 45° (see Figure 6.26) and the portion of light reflected beyond the critical angle calculated with simulated $AIDs_{Si}$ with the phase model (see Figure 6.30). It indicates that both the quantities can be used to predict the light trapping potential of solar cells.

In addition, much larger scattering angles for the reflection than transmission evident from the simulation results suggest that the dominant scattering process regarding the light trapping occurs at the textured back reflectors.

### 6.3.3 Relationship between surface morphology of back reflectors and light trapping in solar cells

In the following, the relationship between the back reflector morphology and the light trapping in the solar cells will be analysed by comparing the variation trend in the surface morphology ($\delta_{rms}$, crater size, crater angle and flat area on surfaces) of the back reflectors to the $J_{SC}$ of the solar cells.

**i. Short circuit current of solar cells vs. rms roughness**

The rms roughness is the most used parameter to statistically characterize the surface morphology. The change in the solar cell performance with the interface morphology is often related to the rms roughness of the interfaces [16,43,81]. In Figure 6.31, the $J_{SC}$ of the solar cells on different textured back reflectors is plotted versus the rms roughness of the back reflectors. One can see a general increase in the $J_{SC}$ with the rms roughness as shown with the dashed line.

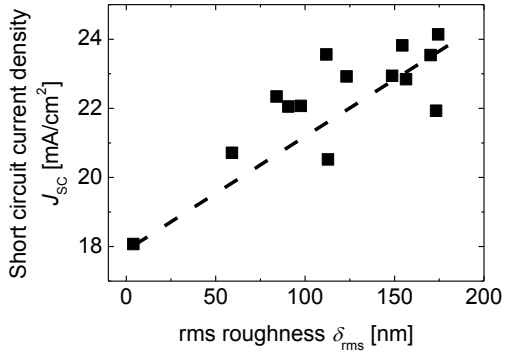


*Figure 6.31 The short circuit current density of the solar cells on the different textured back reflectors is plotted versus the rms roughness. The dashed line indicates the general variation trend of the short circuit current density.*

**Discussion**

Our results show that the $J_{SC}$ of the solar cells increases generally with the rms roughness of the back reflectors. However, it was found in the literature for both the periodical textured

$Al_2O_3$ [18] and randomly textured *Ag* [78] back reflectors, the $J_{SC}$ increases with the $\delta_{rms}$ only up to a certain value (around 60 nm) and gets into saturation. The different variation trends of the $J_{SC}$ with the $\delta_{rms}$ observed from our results and in the literature may be attributed to different types of back reflectors and different variations in the size and angle of surface features. As discussed in Section 6.2, the lateral size or angle of surface textures are the most important parameter for the light scattering, dependent on whether diffraction or geometrical optics playing the dominant role.

Comparing the results in this work and the literature, it can be conclude that the rms roughness of back reflectors alone is not sufficient to estimate the light-trapping potential of solar cells. Other parameters of surface morphologies like e.g. the lateral size and angle of surface textures (craters in our case) may play the essential role for light trapping in solar cells. In the following, the effects of the diameter and angle of craters on light trapping in solar cells will be further examined.

**ii. Short circuit current of solar cells vs. crater diameter**

It was already noticed in Ref. [78,80,126] that light trapping in solar cells is influenced by the lateral size of surface features. However, up to now, the optimal lateral size for the light trapping has not been found from the experimental results. The simulation results with periodical pyramidal features from Haase et al. [22] showed that for features with heights between 400 nm and 500 nm, the lateral sizes between 700 nm and 1300 nm lead to the highest $J_{SC}$ of *p-i-n μc-Si:H* solar cells. In our work, we found a way to vary the mean lateral size of craters (the crater diameter) on *ZnO* surfaces not only in a wide range, but also independent of the crater angle as described in Section 6.1.3. This variation of the surface morphology allows us to analyse the link between the crater diameter and light trapping in solar cells.

Figure 6.32 (a) show the $J_{SC}$ of two series of *μc-Si:H n-i-p* solar cells made on the back reflectors prepared with 800 nm thick *ZnO* layers etched from 0 to 80 s versus the etching time. The $J_{SC}$ is plotted versus the etching time, since it was found in Section 6.1 that the mean crater diameter increases monotonically with the etching time for a given *ZnO* layer thickness (see Figure 6.3 (b)). Two series of solar cells were made for this investigation in order to increase the statistics of the data and verify the reproducibility. One can see in Figure 6.32 (a) the same variation trend of the $J_{SC}$ for both series, although the absolute values at a given etching time are slightly different between Series I and II, likely due to long-term process instability of the *PECVD* system. The short circuit current density increases

significantly with increasing the etching time from 0 to 40 s and gets into saturation. Figure 6.32 (b) shows exemplarily the quantum efficiencies of four solar cells in Series I. One can see a significant difference in the long wavelength region (600 nm ~ 1100 nm).

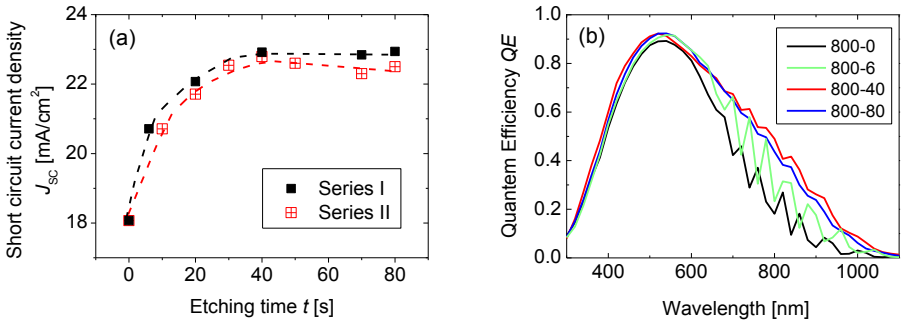


*Figure 6.32 (a) the short circuit current density of two series of solar cells made on back reflectors prepared with 800 nm thick ZnO layers etched from 0 to 80 s. (b) the quantum efficiencies of four solar cells of Series I.*

**Discussion**

On one hand, we found that the mean crater diameter $d_{mean}$ increases monotonically with the etching time for the *ZnO* layers with the as-deposited thickness of 800 nm (see Figure 6.3 (b)). On the other hand, the short circuit current density of the solar cells increases with the etching time only up to certain value (40 s) and is kept almost constant with a further increase in the etching time from 40 s to 80 s (see Figure 6.32 (a)). Therefore, it can be concluded that the $J_{SC}$ increases with the $d_{mean}$ of the back reflectors only up to a certain value and gets into saturation. This variation in the $J_{SC}$ with the $d_{mean}$ is attributed to the changes in the light-scattering properties of the back reflectors. In Section 6.2, the relationship between the angular intensity distribution *AID* for the reflection and the $d_{mean}$ was analysed. The peak position of *AID*s shifts to larger angles with the $d_{mean}$ up to a certain value and keeps at similar angles with a further increase in the $d_{mean}$ (see Figure 6.16 and Figure 6.20). This shift of *AID*s was considered as transition between diffraction and geometrical optics dominant light scattering. In the latter case, the light-scattering properties are mainly influenced by the crater angle. Thus, the saturation of the $J_{SC}$ for certain large $d_{mean}$ can be attributed to the almost constant crater angle of the back reflectors (~25°, see Figure 6.4) in this series of solar cells.

Furthermore, we tried to roughly estimate which crater diameters for a given crater angle of 25° could be most beneficial for the light scattering and trapping in *μc-Si:H* solar cells. It was also published in [127]. For the estimation, the distribution of crater diameters of textured surfaces was analysed. Figure 6.33 shows again the distributions of crater diameters of three 800 nm thick *ZnO* layers etched for (a) 10 s, (b) 40 s and (c) 80 s (also shown in Figure 6.5). As one can see, all the *ZnO* layers have a broad distribution of crater diameters. If craters with certain diameters are much more beneficial for light trapping than the others, we assume that the area density of these craters would have a positive linear correlation to the $J_{SC}$ of the solar cells. Different ranges of crater diameters are considered in this work and shown exemplarily in Figure 6.33 with different colors: Range *A* includes small diameters between 500 nm and 1500 nm (blue), range *B* large diameters between 1500 nm and 2500 nm (green) and range *C* between 900 nm and 2500 nm (red).

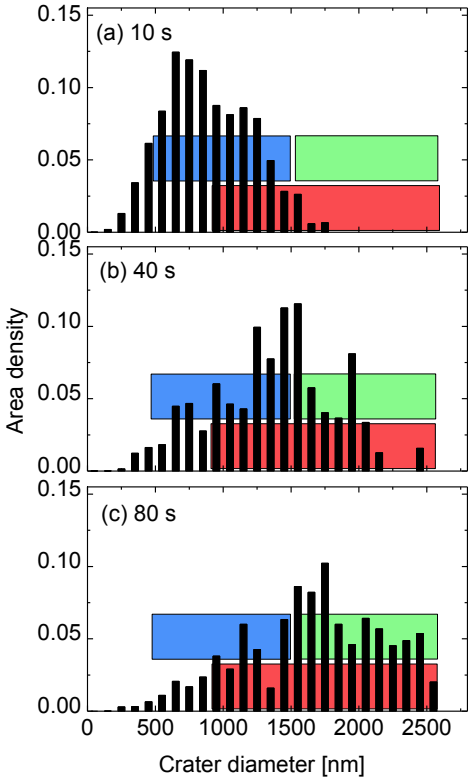


*Figure 6.33 The distributions of crater diameters of ZnO layers etched for (a) 10 s, (b) 40 s and (c) 80 s and four different considered ranges shown with boxes with different colors:*

*Range A includes crater diameters between 500 nm and 1500 nm (blue), range B between 1500 nm and 2500 nm (green), range C between 900 nm and 2500 nm (red).*

The area densities of the craters with diameters in these three considered ranges (*A*, *B* and *C*) are plotted in Figure 6.34 (a) versus the $J_{SC}$ of the solar cells in Series II. It is found that the range *C* with crater diameters between 900 and 2500 nm leads to an almost linear correlation between the area density and $J_{SC}$, while other ranges like A and B together with numerous additional ranges of crater diameters (not shown here) do not. It may suggest that the craters with diameters in the range 900 to 2500 nm are mainly responsible for the change in the $J_{SC}$ and most beneficial for the light trapping of the solar cells.

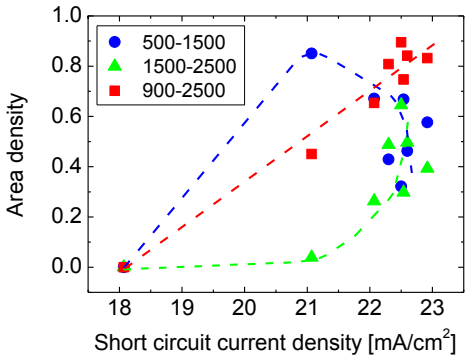


*Figure 6.34 The area density of craters with the diameters in Range A, B and C plotted versus the short circuit current density of the second series of solar cells. Blue, green and red colors are used for Range A (500 nm ~ 1500 nm), B (1500 nm ~ 2500 nm) and C (900 nm ~ 2500 nm).*

**iii. Short circuit current of solar cells vs. crater angle**

It was found in Section 6.2 that the light scattering properties of reflectors is influenced by the crater angle. An increase in the crater angle results in a significant shift of the angular intensity distribution to large angles (see Figure 6.17), which may lead to an improvement in light trapping in solar cells. The link between the crater angle of back reflectors and light-trapping in the solar cells was examined in this work and published in [128].

For this examination, two series of *μc-Si:H n-i-p* solar cells were made on three back reflectors with a similar mean crater diameter of around 850 nm but different crater angles of around 20° (Sample *C*), 25° (Sample *B*) and 30° (Sample *A*). Figure 6.35 (a) shows the short circuit current density of the solar cells versus the crater angle of the back reflectors. For both series of solar cells, the $J_{SC}$ increases by around 1.5 mA/cm$^2$ with an increase in the crater angle from 20° up to 30°. The difference in the $J_{SC}$ between the two series at a given crater angle is likely due to long-term process instability of the *PECVD* system. The quantum efficiencies of the first series of solar cells are shown in Figure 6.35 (b). One can see an improvement in *QE* in the long wavelength region with the increase in the crater angle from 20° up to 30°.

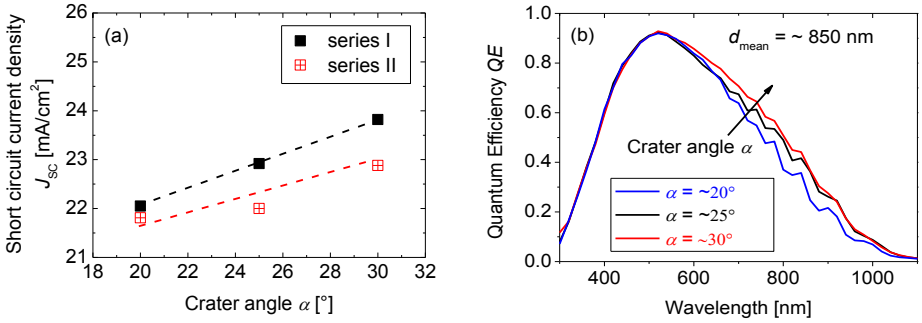


*Figure 6.35 (a) the short circuit current density Jsc of two series of solar cells made on back reflectors with a similar mean crater diameter of 850 nm but different crater angles plotted as a function of the crater angle. (b) The quantum efficiencies of solar cells of Series I on Sample A, B and C with crater angles of 20°, 25° and 30°, respectively.*

**Discussion**

Since the back reflectors in these solar cells have quite similar mean crater diameters, the improvement in the $J_{SC}$ and *QE* in the long wavelength range of the solar cells can be related to the increase in the crater angle of the back reflectors. Together with the results of light-scattering properties presented in Section 6.2, it can be concluded that for back reflectors with a large mean crater diameter like 850 nm, an increase in the crater angle can result in a

significant shift of the *AID* to large angles (see Figure 6.17) and an improvement in the light trapping in *μc-Si:H* solar cells.

**iv. Short circuit current of solar cells vs. flat area on back reflectors**

It was found in Section 6.2 that the light-scattering properties of reflectors are influenced by flat area on their surfaces (see Figure 6.13 and Figure 6.18). In the following, we will investigate the effects of flat area of back reflectors on light trapping of solar cells.

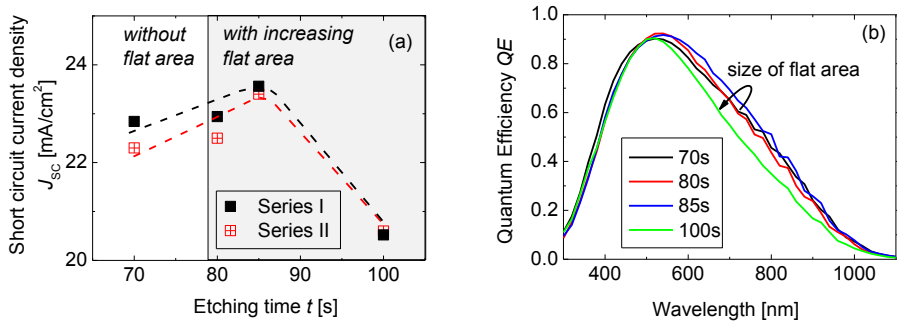


*Figure 6.36 (a) the short circuit current density Jsc of two series of solar cells made on back reflectors prepared with 800 nm thick ZnO layers etched from 70 to 100 s. The white and grey area in Figure (a) show the ZnO surfaces without and with flat area, respectively. (b) the quantum efficiencies of four solar cells of Series I.*

Two series of *μc-Si:H n-i-p* solar cells were made on the back reflectors prepared with 800 nm thick *ZnO* layers etched from 70 s to 100 s. From the *AFM* images in Figure 6.2, one can see flat area starts to appear on the 800 nm thick *ZnO* layer etched for 80 s. With increasing the etching time from 80 s to 100s, flat areas get larger. Figure 6.36 shows (a) the short circuit current density $J_{SC}$ of the solar cells as a function of the etching time. For both series of solar cells, the $J_{SC}$ increases slightly (by 0.8 and 1.1 mA/cm$^2$ for Series I and II, respectively) with increasing the etching time from 70 s to 85 s and decreases significantly by around 3 mA/cm$^2$ with a further increase in the etching time up to 100 s. Figure 6.36 (b) shows the quantum efficiencies *QE* of the first series of solar cells as examples. Main effects

of the etching time (flat area) on the quantum efficiency occur in the long wavelength region. The *QE* in the long wavelength region increases slightly with the etching time from 70 s to 85 s and decreases significantly with increasing the etching time up to 100 s.

**Discussion**

The decrease in $J_{SC}$ with increasing the etching time from 85 s to 100 s (see Figure 6.36) can be attributed to the increase in the flat area on the surface, which leads to worse light-scattering properties of the back reflector, like a decrease in haze (see Figure 6.8) and a shift of *AID* to smaller angles (see Figure 6.14). The slight increase in the $J_{SC}$ with the etching time from 70 s to 85 s (see Figure 6.36) suggests an improvement of light trapping, however, cannot be explained with the similar light-scattering properties (haze and *AID*) of the back reflectors measured in far-field in air (see Figure 6.8 and Figure 6.14). This improvement in light trapping might be attributed to better local scattering properties, which can be measured by near-field scanning optical microscopy *NSOM* and simulated by finite-difference time-domain *FDTD* [129,130]. With the simulation results of the local scattering properties in silicon, it was found in Ref. [130] that more light can be locally absorbed in silicon for craters with a small flat bottom whose lateral size is less than 20% of the crater diameter (the lateral size on top of craters). This prediction is in a good agreement with our experimental results and can be an explanation for the increase in the $J_{SC}$ of the solar cells on the back reflectors with few small flat areas, which act as flat bottoms of craters.

## 6.4 Summary

In this chapter, the analysis of the relationship between the surface morphology, light-scattering properties of back reflectors and light trapping in *μc-Si:H n-i-p* solar cells is presented.

Firstly, the *ZnO* surface morphology was varied by changing the etching time and as-deposited thickness and statistically evaluated in terms of not only the rms roughness, but also the diameter, depth and angle of craters on the surfaces. Based on the statistical evaluation, four possible variations of the surface morphology can be revealed. In the first possible variation I, both the mean diameter and depth of craters vary together while the crater angle α is similar. In the variations II and III, the angle of craters is varied, while the mean crater diameter and depth is kept almost constant, respectively. In the fourth possible variation IV considered here, *ZnO* are over-etched down to glass substrates so that flat area appears on the surfaces. These variations provide the possibility to systematically analyse the effects of the crater size, angle and flat area on surfaces on the light-scattering properties of back reflectors and light trapping in solar cells.

To analyse the relationship between the surface morphology and light-scattering properties for the reflection, etched-*ZnO* layers with different surface morphologies were covered with a thin Ag layer and the light-scattering properties of these etched-*ZnO/Ag* reflectors were investigated in terms of the haze and angular intensity distribution *AID*.

The relationship between the surface morphology and haze of reflectors can be concluded as follows:

- For the surfaces without flat area, the relation between the $\delta_{rms}$ and haze of etched-*ZnO/Ag* reflectors observed from our experiments has a good agreement with the prediction of the simulation model based on the scalar scattering theory. It suggests that the haze for the reflection can be determined with $\delta_{rms}$, as long as no large flat area appears on the surfaces.
- Besides $\delta_{rms}$, the haze of etched-*ZnO/Ag* reflectors is influenced by flat area on surfaces. A surface with some large flat area may have lower haze than the one with the same rms roughness but without flat area.

The relationship between the surface morphology and *AID* of etched-*ZnO/Ag* reflectors can be concluded as follows:

- Surfaces with a quite similar $\delta_{rms}$ may have quite different *AID*s, which suggests that the $\delta_{rms}$ alone cannot determine the *AID* for the reflection and a more detailed description of

the surface morphology in terms of the diameter *d*, depth *h* and angle $\alpha$ of surface features (craters) may be necessary.

- For the surfaces with a given crater angle $\alpha$, the peak position of *AID*s shifts firstly to larger scattering angles with increasing the mean crater diameter $d_{mean}$ and then get into saturation.
- For the surfaces with a given large $d_{mean}$, the peak position of *AID*s shifts significantly to larger scattering angles with increasing $\alpha$.
- The variations in the peak position of *AID*s with the $d_{mean}$ and $\alpha$ are attributed to the combined impact of diffraction and geometrical optics on light scattering. When the mean crater diameter is small, diffraction has a dominant impact on the *AID*. With increasing the mean crater diameter, the geometrical optics plays more important role and turns into the dominant physical mechanism for the light scattering. Thus, the shift of the *AID* peak position with the $\alpha$ for a given large $d_{mean}$ can be explained by geometrical optics. The shift of the *AID* peak position with the $d_{mean}$ for a given $\alpha$ is considered as transition from diffraction dominant to geometrical optics dominant light scattering.

In addition, the effects of the back reflector surface morphology on the performance of *μc-Si:H n-i-p* solar cells were investigated. For this investigation, the etched *ZnO* layers with different surface morphologies were covered with a thin *Ag* and *ZnO* layers and the etched-*ZnO/Ag/ZnO* sandwich layers were used as back reflectors in solar cells. It is found that the *FF* and $V_{OC}$ are quite similar for all the solar cells, while the $J_{SC}$ changes significantly with the back reflector surface morphology. The change in $J_{SC}$ is mainly attributed to the change in the *QE* in the long wavelength range, which is related to the change in the light trapping in the solar cells.

The change in the light trapping may result from the change in the light-scattering properties of the back reflectors with their surface morphologies. To examine the link between the light trapping and haze of the back reflectors, the $J_{SC}$ of all the solar cells is plotted versus the haze of *ZnO/Ag* reflectors at the light wavelength of 300 nm. All the reflectors have very high haze close to 1 at $\lambda$ = 300 nm, although the $J_{SC}$ of all the solar cells are quite different. It suggests that the haze of back reflectors alone is not sufficient to estimate the light-trapping potential of *μc-Si:H n-i-p* solar cells. On the other hand, it is found that the integration of *AID*s for the scattering angles beyond a relative large angle (in our case we chose 45°) is well correlated to the $J_{SC}$ of the solar cells, which suggests that this quantity can be used to estimate the light-trapping potential of *μc-Si:H n-i-p* solar cells.

To further understand the correlation between the *AID* of back reflectors and the $J_{SC}$ of solar cells and the light trapping process in solar cells, *AID*s in silicon were simulated with the phase model for both the transmission at the *μc-Si:H/ZnO* interface on the front side of solar cells and the reflection at the back reflector. For all the investigated samples in this study, the peak position of the *AID*s for the reflection at back reflectors is located at much larger scattering angles than for the transmission at the *μc-Si:H/ZnO* interface. Moreover, a positive correlation is also found between the $J_{SC}$ and the portion of the light reflected on back reflectors beyond a certain large angle, like the critical angle for the total reflection at the *μc-Si:H/ZnO* interface. Both these results suggest that the dominant scattering process regarding the light trapping occurs at the textured back reflectors in the solar cells.

Finally, the link between the surface morphology of back reflectors and the light trapping in *μc-Si:H n-i-p* solar cells were investigated by comparing the variation trend in the surface morphology to the $J_{SC}$ of the solar cells. The investigation results can be concluded as follows:

- The rms roughness of back reflectors alone is not sufficient to estimate the light-trapping potential of solar cells. Other parameters of surface morphologies like e.g. the lateral size and angle of craters may play the essential role.
- By analysing the distribution of crater diameters, we roughly estimated which range of crater diameters for a give crater angle could be most beneficial for the light trapping in solar cells. The area density of craters with diameters between 900 nm and 2500 nm has a positive linear correlation with the $J_{SC}$ of the solar cells. It suggests that the craters with diameters in this range might be mainly responsible for the change in the $J_{SC}$ and most beneficial for the light trapping in solar cells.
- With a similar mean crater diameter, the $J_{SC}$ of the solar cells increases with increasing the crater angle of back reflectors. It suggests that an increase in the crater angle of back reflectors leads to an improvement of the light trapping in solar cells.
- With increasing the size of flat area on back reflectors, the $J_{SC}$ of solar cells firstly increases slightly and then decreases. The slight increase in the $J_{SC}$ suggests that light trapping can be improved by small flat area on the back reflectors, likely due to better local scattering properties. The decrease in the $J_{SC}$ with large flat area suggests a deterioration of the light-scattering properties of back reflectors and the light trapping in solar cells.

# 7. Summary

The present work has focussed on the experimental and theoretical investigation of the light trapping of thin film silicon solar cells in an n-i-p configuration. The *n-i-p* configuration offers more flexibility to modify the surface morphology of back reflectors for light trapping than in the *p-i-n* configuration, where textured front *TCO* are used for light trapping and the modification of its surface morphology is limited by the requirements for the electrical and optical properties.

In the first step, the *n-i-p* solar cell device was set up based on the existing optimized processes for *p-i-n* solar cells. For *μc-Si:H n-i-p* solar cells, the thickness and doping ratio of *p*-type layers, the silane concentration of i-layers and the thickness of front *TCO*s were optimized. Moreover, two types of substrates (*glass/etched-ZnO* and *glass/etched-ZnO/Ag/ZnO*) were used for a series of *μc-Si:H n-i-p* solar cells. The same variation trends in the cell performance are found for all the solar cells with and without the *Ag/ZnO* reflector. The results suggest that simple glass*/ZnO* substrates can serve as a benign and reproducible standard for the optimization of *n-i-p* solar cells. For *a-Si:H n-i-p* solar cells, the material, deposition conditions and thickness of front contacts were optimized. Three types of *TCO*s prepared with different materials (*ZnO* and *ITO*) and conditions were used as front contacts. One type of *ITO* leads to the highest $J_{SC}$ and cell efficiency, due to the lowest light absorption. Finally, a quite high performance of *n-i-p* solar cells is achieved with an efficiency above 8% and 9% for ~ 1μm thick *μc-Si:H solar* cells and ~ 250 nm thick *a-Si:H* solar cells, respectively.

After a good reproducibility of the process was achieved, the links between the surface morphology, light-scattering properties of back reflectors and light trapping in *μc-Si:H n-i-p* solar cells were investigated. The back reflectors were prepared by covering *etched-ZnO* with a thin *Ag* and *ZnO* layers. By using this kind of back reflectors, the link between the surface morphology and light trapping can be directly analysed without taking care of the optical and electrical properties of the *etched-ZnO* layers.

One of the crucial tasks in this work was to vary the surface morphology of *etched-ZnO* layers. In literature, it was found that the size of surface features (craters) on *etched-ZnO* layers can be varied by changing the etching time, while the angle of craters keeps almost constant. In this work, besides varying the etching time, we varied also the as-deposited thickness of *ZnO* layers and found that the angle of craters increases with the as-deposition thickness. This approach provides a possibility to vary the size and angle of craters

independently by adjusting both the etching time and as-deposited thickness of *ZnO* layers. Furthermore, we evaluated the *etched-ZnO* surface morphologies in terms of not only the *rms* roughness (as discussed in the majority of literature) but also the diameter, depth and angle of craters. With such evaluation, we are able to investigate the relationship between the surface morphology and light-scattering properties of back reflectors in details and analyse the impact of different physical mechanism, such as diffraction and geometrical optics on the light-scattering properties.

The light-scattering properties for the reflection were investigated in terms of the haze and angular intensity distribution *AID*. A correlation between the $\delta_{rms}$ and haze for the reflection was observed from our experimental results, except for some surfaces with large flat area. This correlation has a good agreement with the prediction of the simulation model based on the scalar scattering theory. However, no clear relationship between the $\delta_{rms}$ and *AID* was observed. It was found that the surfaces with a similar $\delta_{rms}$ can have quite different *AID*s. Therefore, the relationship between the surface morphology and *AID* was further analysed based on the detailed description of surface morphologies introduced above (in terms of the diameter and angle of craters). For the surfaces with a given crater angle, the peak position of *AID*s shifts firstly to larger scattering angles with increasing the mean crater diameter $d_{mean}$ and then keeps almost constant. For the surfaces with a given large $d_{mean}$, the peak position of *AID*s shifts significantly to larger scattering angles with increasing the crater angle. These variations in the *AID* with the $d_{mean}$ and $\alpha$ of craters are attributed to the combined impact of diffraction and geometrical optics. When the diameter of most of the crater is smaller than the wavelength of the incident light, diffraction has a dominant impact on the *AID*. With increasing the diameter, the geometrical optics plays more important role and turns into the dominant physical mechanism for the light scattering. The latter case can explain well the shift of *AID*s with the crater angle which was observed in our results, while the shift of *AID*s with $d_{mean}$ can be considered as transition between two dominant physical mechanisms: diffraction and geometrical optics.

In addition, the effects of the back reflector surface morphology on the performance of *μc-Si:H n-i-p* solar cells were investigated. The main effect is on the short circuit current density $J_{SC}$, while the fill factor *FF* and the open circuit voltage $V_{OC}$ are quite similar for all the solar cells. The change in $J_{SC}$ is mainly attributed to the change in light trapping in the solar cells, which may result from different light-scattering properties of the back reflectors. To further understand the light trapping process in solar cells, *AID*s in silicon were simulated with the so-called phase model for both the transmission at the *μc-Si:H/ZnO* interface on the

front side of solar cells and the reflection at the back reflector. For all the investigated samples in this study, the peak position of the simulated *AID*s for the reflection is located at much larger angles than for the transmission. Moreover, an almost linear correlation is found between $J_{SC}$ and the portion of the light reflected on back reflectors beyond a relative large angle, like the critical angle for the total reflection at the *μc-Si:H/ZnO* interface. These results suggest that the dominant scattering process regarding the light trapping occurs at the textured back reflectors in the solar cells.

Finally, the link between the surface morphology of back reflectors and light-trapping in *μc-Si:H n-i-p* solar cells was directly analysed by comparing the trend in the variation of the surface morphology with $J_{SC}$ of the solar cells. It is found that the rms roughness of back reflectors alone is not sufficient to estimate the light-trapping potential of solar cells and the size and angle of craters may play the essential role. By analysing the distribution of crater diameters, we estimated roughly which range of crater diameters for a give crater angle (25° in our case) could be most beneficial for light trapping in solar cells. Since the area density of craters with diameters between 900 nm and 2500 nm has an almost linear correlation with $J_{SC}$, we conclude that the craters with diameters in this range are most beneficial for light trapping in solar cells. It was also found that an increase of the crater angle of back reflectors leads to an improvement of light trapping in solar cells. Moreover, a slight increase of $J_{SC}$ with small flat area on back reflectors suggests that light trapping in solar cells might be improved by the small flat area, likely due to better local scattering properties of back reflectors.

In conclusion, the relationships between the surface morphology, the light-scattering properties of back reflectors and $J_{SC}$ of silicon thin film *n-i-p* solar cells were systematically analysed in this work. The etched–*ZnO* surface morphology was statistical analysed in terms of the diameter, depth and angle of craters. With the detailed analysis, the effects of the surface morphology on the light-scattering properties were related to different impacts of diffraction and geometrical optics on the light scattering. By comparing the simulated angular intensity distribution at back reflectors and at the *μc-Si:H/ZnO* interface on the front side of solar cells, we can conclude that the dominant scattering process regarding the light trapping occurs at the textured back reflectors. In addition, by analysing the relationship between the surface morphology of back reflectors and $J_{SC}$ of solar cells, the most beneficial size, angle and shape of craters for light trapping were proposed.

# References


[1] M.A. Green, K. Emery, Y. Hishikawa, W. Warta, E.D. Dunlop, Progress in Photovoltaics: Research and Applications 39 (2012) 12.

[2] J. Zhao, A. Wang, M. a. Green, F. Ferrazza, Applied Physics Letters 73 (1998) 1991.

[3] O. Schultz, S.W. Glunz, G.P. Willeke, Progress in Photovoltaics: Research and Applications 12 (2004) 553.

[4] J. Poortmans, V. Arkhipov, Thin Film Solar Cells- Fabrication Characterization and Applications, John Wiley & Sons, 2006.

[5] A. Shah, Thin-film Silicon Solar Cells, CRC Press, 2008.

[6] K. Yamamoto, M. Yoshimi, Y. Tawada, Y. Okamoto, A. Nakajima, S. Igari, Applied Physics A: Materials Science & Processing 69 (1999) 179.

[7] Y. Mai, S. Klein, R. Carius, J. Wolff, A. Lambertz, F. Finger, Journal of Applied Physics 97 (2005) 114913.

[8] J. Bailat, D. Dominé, R. Schlüchter, J. Steinhauser, S. Faÿ, F. Freitas, C. Bücher, L. Feitknecht, X. Niquille, T. Tscharner, A. Shah, C. Ballif, Proceeding of IEEE 4th World Conference on Photovoltaic Energy Conversion (2006) 1533.

[9] A. Banerjee, T. Su, D. Beglau, G. Pietka, F.S. Liu, S. Almutawalli, J. Yang, S. Guha, IEEE Journal of Photovoltaics 2 (2012) 99.

[10] J. Hüpkes, J. Müller, B. Rech, in: Transparent Conductive Zinc Oxide, K. Ellmer, A. Klein, B. Rech (Eds.), Basics and Applications in Thin Film Solar Cells, Transparen, Springer, Berlin Heidelberg, 2008.

[11] O. Kluth, G. Schöpe, J. Hüpkes, C. Agashe, J. Müller, B. Rech, Thin Solid Films 442 (2003) 80.

[12] J. Krc, B. Lipovsek, M. Bokalic, A. Campa, T. Oyama, M. Kambe, T. Matsui, H. Sai, M. Kondo, M. Topic, Thin Solid Films 518 (2010) 3054.

[13] M. Berginski, J. Hüpkes, M. Schulte, G. Schöpe, H. Stiebig, B. Rech, M. Wuttig, Journal of Applied Physics 101 (2007) 074903.

[14] J. Müller, B. Rech, J. Springer, M. Vanecek, Solar Energy 77 (2004) 917.

[15] J. Yang, a. Banerjee, S. Guha, Applied Physics Letters 70 (1997) 2975.

[16] G. Yue, L. Sivec, J.M. Owens, B. Yan, J. Yang, S. Guha, Applied Physics Letters 95 (2009) 263501.

[17] H. Li, R. Stolk, C. Vanderwerf, R. Franken, J. Rath, R. Schropp, Journal of Non-Crystalline Solids 352 (2006) 1941.

[18] H. Sai, M. Kondo, Journal of Applied Physics 105 (2009) 094511.

[19] F.-J. Haug, T. Söderström, M. Python, V. Terrazzoni-Daudrix, X. Niquille, C. Ballif, Solar Energy Materials & Solar Cells 93 (2009) 884.

[20] T. Söderström, F.-J. Haug, V. Terrazzoni-Daudrix, C. Ballif, Journal of Applied Physics 107 (2010) 014507.

[21] B. Yan, G. Yue, L. Sivec, J. Owens-Mawson, J. Yang, S. Guha, Solar Energy Materials and Solar Cells 104 (2012) 13.

[22] C. Haase, H. Stiebig, Applied Physics Letters 91 (2007) 061116.

[23] H. Zhu, J. Hüpkes, E. Bunte, J. Owen, S.M. Huang, Solar Energy Materials and Solar Cells 95 (2011) 964.

[24] R. Street, Hydrogenated Amorphous Silicon, Cambridge University Press, Cambridge, 1991.

[25] W. Luft, Y. Tsuo, Hydrogenated Amorphous Silicon Alloy Deposition Processes, CRC Press, New York, 1993.

[26] G. Bruno, A. Madan, P. Capezzuto, Plasma Deposition of Amorphous Silicon-Based Materials, Academic Press Limited, 1995.

[27] O. Vetterl, On the Physics of Microcrystalline Silicon Thin Film Solar Cells – From the Materail to Devices with High Conversion Efficiencies, Dissertation, Universität Düsseldorf, 2001.

[28] S. Klein, F. Finger, R. Carius, T. Dylla, B. Rech, M. Grimm, L. Houben, M. Stutzmann, Thin Solid Films 430 (2003) 202.

[29] S. Klein, F. Finger, R. Carius, M. Stutzmann, Journal of Applied Physics 98 (2005) 024905.

[30] D.L. Staebler, C.R. Wronski, Applied Physics Letters 31 (1977) 292.

[31] M. Stutzmarin, W. B.Jackson, C.C. Tsai, Physical Review B 32 (1985) 23.

[32] M. Tzolov, F. Finger, R. Carius, P. Hapke, Journal of Applied Physics 81 (1997) 7376.

[33] M. Luysberg, P. Hapke, R. Carius, F. Finger, Philosophical Magazine A 75 (1997) 37.

[34] L. Houben, M. Luysberg, P. Hapke, R. Carius, F. Finger, H. Wagner, Philosophical Magazine A 77 (1998) 1447.

[35] L. Guo, M. Kondo, M. Fukawa, K. Saitoh, A. Matsuda, Japanese Journal of Applied Physics 37 (1998) 1116.

[36] O. Vetterl, F. Finger, R. Carius, P. Hapke, L. Houben, O. Kluth, A. Lambertz, A. Mück, B. Rech, H. Wagner, Solar Energy Materials & Solar Cells 62 (2000) 97.

[37] S. Ray, S. Mukhopadhyay, T. Jana, R. Carius, Journal of Non-Crystalline Solids 299-302 (2002) 761.

[38] A. Shah, J. Meier, E. Vallat-Sauvain, N. Wyrsch, U. Kroll, C. Droz, U. Graf, Solar Energy Materials and Solar Cells 78 (2003) 469.

[39] S. Okur, M. Günes, O. Göktas, F. Finger, R. Carius, Journal of Materials Science: Materials in Electronics 15 (2004) 187.

[40] J. Kočka, T. Mates, H. Stuchlíková, J. Stuchlík, A. Fejfar, Thin Solid Films 501 (2006) 107.

[41] K. Hattori, H. Okamoto, Y. Hamakawa, 45 (1992) 1126.

[42] I. Sakata, M. Yamanaka, T. Sekigawa, Journal of Applied Physics 81 (1997) 1323.

[43] M. Zeman, R.A.C.M.M.V. Swaaij, J.W. Metselaar, Journal of Applied Physics 88 (2000) 11.

[44] T. Matsui, M. Tsukiji, H. Saika, T. Toyama, Non-Crystalline Solids 302 (2002) 1152.

[45] T. Söderström, F.-J. Haug, V. Terrazzoni-Daudrix, X. Niquille, M. Python, C. Ballif, Journal of Applied Physics 104 (2008) 104505.

[46] K. Sato, Y. Gotoh, Y. Wakayama, Y. Hayashi, K. Adachi, H. Nishimura, Rep. Res. Lab. AsahiGlass Co. Ltd. 42 (1992) 129.

[47] J. Linden, R. Groenen, J. Löffler, J. Rath, P. Sommeling, R. Schropp, M. van de Sanden, Proceeding of the 3rd World Conference on Photovoltaic Energy Conversion (2003) 42.

[48] S. Nicolay, M. Despeisse, F.-J. Haug, C. Ballif, Solar Energy Materials and Solar Cells 95 (2011) 1031.

[49] Y. Nasuno, N. Kohama, K. Nishimura, T. Hayakawa, H. Taniguchi, M. Shimizu, Applied Physics Letters 88 (2006) 071909.

[50] J. Yang, A. Banerjee, S. Guha, Solar Energy Materials and Solar Cells 78 (2003) 597.

[51] K. Saito, M. Sano, H. Otoshi, A. Sakai, S. Okabe, K. Ogawa, Proceeding of the 3rd World Conferance on Photovoltaic Energy Conversion (2003) 2793.

[52] Y. Ichikawa, K. Tabuchi, A. Takano, S. Fujikake, T. Yoshida, H. Sakai, Journal of Non-Crystalline Solids 200 (1996) 1081.

[53] J. Bailat, V. Terrazzoni-Daudrix, J. Guillet, F. Freitas, X. Niquille, A. Shah, C. Ballif, T. Scharf, R. Morf, A. Hansen, D. Fischer, Y. Ziegler, A. Closset, Proceeding of the 20th European PVSEC (2005).

[54] F.-J. Haug, V. Terrazzoni-Daudrix, T. Söderström, X. Niquille, J. Bailat, C. Ballif, Proceeding of the 21st European PVSEC (2006).

[55] O. Kluth, A. Loffl, S. Wieder, C. Beneking, W. Appenzeller, L. Houben, B. Rech, H. Wagner, S. Hoffmann, R. Waser, J.A.A. Selvan, H. Keppnet, Proceeding of the 26th IEEE Photovoltaic Specialists Conference (1997) 715.

[56] O. Kluth, B. Rech, L. Houben, S. Wieder, G. Schöpe, C. Beneking, H. Wagner, A. Löffl, H. Schock, Thin Solid Films 351 (1999) 247.

[57] P.S. Nayar, Applied Physics Letters 39 (1981) 105.

[58] T. Minami, H. Nanto, S. Takata, Japanese Journal of Applied Physics 23 (1984) 280.

[59] A. Suzuki, T. Matsushita, Y. Sakamoto, N. Wada, T. Fukuda, H. Fujiwara, M. Okuda, Japanese Journal of Applied Physics 35 (1996) 5457.

[60] E. Kaidashev, M. Lorenz, H. von Wenckstern, A. Rahm, H. Semmelhack, K. Han, G. Benndorf, C. Bundesmann, H. Hochmuth, M. Grundmann, Applied Physics Letters 82 (2003) 3901.

[61] J.H. Morgan, D.E. Brodie, Canadian Journal of Physics 60 (1982) 1387.

[62] M. Jin, J. Feng, D. Zhang, H. Ma, S. Li, Thin Solid Films 357 (1999) 98.

[63] O. Kluth, Texturiete Zinkoxidschichten Für Silizium-Dünnschichtsolarzellen, Dissertation, Rheinisch Westfälischen Technischen Hochschule Aachen, 2001.

[64] M. Berginski, Lichtsteuende Oberflächen, Schichten Und Schichtsysteme Zur Verbesserung Der Lichteinkopplung in Silizium-Dünnschichtsolarzellen, Dissertation, Rheinisch Westfälischen Technischen Hochschule Aachen, 2007.

[65] J. Hüpkes, B. Rech, S. Calnan, O. Kluth, U. Zastrow, H. Siekmann, M. Wuttig, Thin Solid Films 502 (2006) 286.

[66] J.I. Owen, Growth, Etching, and Stability of Sputtered ZnO:Al for the Thin-Film Silicon Solar Cells, Dissertation, Rheinisch Westfälischen Technischen Hochschule Aachen, 2011.

[67] D.-W. Kang, S.-H. Kuk, K.-S. Ji, S.-W. Ahn, M.-K. Han, Physica Status Solidi (C) 7 (2010) 925.

[68] Y.H. Kim, K.S. Lee, T.S. Lee, B. Cheong, T. Seong, W.M. Kim, Current Applied Physics 10 (2010) S278.

[69] T. Tohsophon, J. Hüpkes, H. Siekmann, B. Rech, M. Schultheis, N. Sirikulrat, Thin Solid Films 516 (2008) 4628.

[70] H. Zhu, E. Bunte, J. Hüpkes, H. Siekmann, S.M. Huang, Thin Solid Films 517 (2009) 3161.

[71] J. Thornton, Journal of Vacuum Science & Technology 11 (1974) 666.

[72] J. Thornton, Annual Review of Materials Science 7 (1977) 239.

[73] W. Jo, S.-J. Kim, D.-Y. Kim, Acta Materialia 53 (2005) 4185.

[74] A.N. Mariano, R.E. Hanneman, Journal of Applied Physics 34 (1963) 384.

[75] K. Sato, K. Adachi, Y. Hayashi, M. Mizuhashi, Proceeding of the 20th IEEE Photovoltaic Specialists Conference (1988) 267.

[76] M. Kambe, M. Fukawa, N. Taneda, Y. Yoshikawa, K. Sato, Proceeding of the 3rd World Conference on Photovoltaic Energy Conversion 02 (2003) 1812.

[77] J. Springer, B. Rech, W. Reetz, J. Müller, M. Vanecek, Solar Energy Materials and Solar Cells 85 (2005) 1.

[78] R.H. Franken, R.L. Stolk, H. Li, C.H.M. van der Werf, J.K. Rath, R.E.I. Schropp, Journal of Applied Physics 102 (2007) 014503.

[79] H. Stiebig, N. Senoussaoui, C. Zahren, C. Haase, J. Müller, Progress in Photovoltaics: Research and Applications 14 (2006) 13.

[80] H. Schade, P. Lechner, R. Geyer, H. Stiebig, B. Rech, O. Kluth, Proceeding of the 31st IEEE Photovoltaic Specialists Conference (2005) 1436.

[81] J. Krc, M. Zeman, O. Kluth, F. Smole, M. Topic, Thin Solid Films 426 (2003) 296.

[82] M. Schulte, K. Bittkau, K. Jäger, M. Ermes, M. Zeman, B.E. Pieters, Applied Physics Letters 99 (2011) 111107.

[83] K. Bittkau, M. Schulte, M. Klein, T. Beckers, R. Carius, Thin Solid Films 519 (2011) 6538.

[84] D. Dominé F.-J. Haug, C. Battaglia, C. Ballif, Journal of Applied Physics 107 (2010) 044504.

[85] C.K. Carniglia, Optical Engineering 18 (1979) 104.

[86] J. Krc, M. Zeman, F. Smole, M. Topic, Journal of Applied Physics 92 (2002) 749.

[87] K. Bittkau, M. Schulte, T. Beckers, R. Carius, Proceeding of SPIE Photonics West 5 (2010) 77250.

[88] J. Goodman, Introduction to Fourier Optics, Roberts & Company, Greenwood Village, 2005.

[89] J.E. Harvey, C.L. Vernold, A. Krywonos, P.L. Thompson, Applied Optics 38 (1999) 6469.

[90] K. Bittkau, W. Böttler, M. Ermes, V. Smirnov, F. Finger, Journal of Applied Physics 111 (2012) 083101.

[91] F.-J. Haug, T. Söderström, O. Cubero, V. Terrazzoni-Daudrix, C. Ballif, Journal of Applied Physics 106 (2009) 044502.

[92] E. Moulin, U.W. Paetzold, H. Siekmann, J. Worbs, A. Bauer, R. Carius, Energy Procedia 10 (2011) 106.

[93] W. Zhang, Ion Beam Treatment of Functional Layers in Thin-Film Silicon Solar Cells, Dissertation, Rheinisch Westfälischen Technischen Hochschule Aachen, 2012.

[94] M. Berginski, J. Hupkes, W. Reetz, B. Rech, M. Wuttig, Thin Solid Films 516 (2008) 5836.

[95] H. Richter, Z.P. Wang, L. Ley, Solid State Communications 39 (1981) 625.

[96] G. Binnig, C.F. Quate, C. Gerber, Physical Review Letters 56 (1986) 930.

[97] S. Beucher, C. Lantuejoul, Proceeding of the Int. Workshop on Image Processing: Real-tim Edge and Motion Detection/estimation (1979).

[98] K. Emery, in: Measurement and Characterization of Solar Cells and Modules, A. Luque, S. Hegedus (Eds.), Handbook of Photovoltaic Science and Engineering, John Wiley & Sons, Chichester, UK., 2003.

[99] T. Kirchartz, K. Ding, U. Rau, in:, D. Abou-Ras, R. Rau, T. Kirchartz (Eds.), Advanced Characterization Techniques for Thin Film Solar Cells, Wiley-VCH Verlag GmbH & Co. KGaA, Germany, 2011.

[100] U. Rau, H.W. Schock, Applied Physics A 147 (1999) 131.

[101] J. Metzdorf, Applied Optics 26 (1987) 1701.

[102] S. Klein, T. Repmann, T. Brammer, Solar Energy 77 (2004) 893.

[103] A. Dasgupta, A. Lambertz, O. Vetterl, F. Finger, R. Carius, U. Zastrow, H. Wagner, 16th European Photovoltaic Solar Energy Conference and Exhibition Energy (2000) 477.

[104] V. Smirnov, C. Das, T. Melle, A. Lambertz, M. Hülsbeck, R. Carius, F. Finger, Materials Science and Engineering B 159-160 (2009) 44.

[105] J. Müller, O. Kluth, S. Wieder, H. Siekmann, G. Schöpe, W. Reetz, O. Vetterl, D. Lundszien, A. Lambertz, F. Finger, B. Rech, H. Wagner, Solar Energy Materials & Solar Cells 66 (2001) 275.

[106] Y. Mai, Microcrystalline Silicon Layers for Thin Film Solar Cells Prepared with Hot Wire Chemical Vapour Deposition and Plasma Enhanced Chemical Vapour Deposition, Dissertation, Nankai University, China, 2007.

[107] K. Ding, T. Kirchartz, B.E. Pieters, C. Ulbrich, A.M. Ermes, S. Schicho, A. Lambertz, R. Carius, U. Rau, Solar Energy Materials & Solar Cells 95 (2011) 3318.

[108] W. Böttler, V. Smirnov, A. Lambertz, J. Hüpkes, F. Finger, Physica Status Solidi (C) 7 (2010) 1069.

[109] J. Kočka, A. Fejfar, H. Stuchlíková, J. Stuchlík, P. Fojtík, T. Mates, B. Rezek, K. Luterová, V. Švrček, I. Pelant, Solar Energy Materials and Solar Cells 78 (2003) 493.

[110] T. Fujibayashi, M. Kondo, Journal of Applied Physics 99 (2006) 043703.

[111] U. K. Das, E. Centurioni, S. Morrison, A. Madan, Proceeding of the 3rd World Conferance on Photovoltaic Energy Conversion (2003) 1776.

[112] K. Adhikary, S. Ray, Journal of Non-Crystalline Solids 353 (2007) 2289.

[113] H. Lee, A. Sazonov, A. Nathan, Proceeding of Materials Research Society 989 (2007) 0989.

[114] P. Kumar, M. Kupich, D. Grunsky, B. Schroeder, Thin Solid Films 501 (2006) 260.

[115] M. Kubon, E. Boehmer, F. Siebke, B. Rech, C. Beneking, H. Wagner, Solar Energy Materials and Solar Cells 41-42 (1996) 485.

[116] G.A. Neuman, Journal of Non-Crystalline Solids 218 (1997) 92.

[117] J. Hüpkes, B. Rech, O. Kluth, T. Repmann, B. Zwaygardt, J. Müller, R. Drese, M. Wuttig, Solar Energy Materials & Solar Cells 90 (2006) 3054.

[118] M. Berginski, J. Hüpkes, A. Gordijn, W. Reetz, T. Watjen, B. Rech, M. Wuttig, Solar Energy Materials & Solar Cells 92 (2008) 1037.

[119] W. Beyer, J. Hüpkes, H. Stiebig, Thin Solid Films 516 (2007) 147.

[120] M. Schulte, Streuverhalten Von Texturierten TCO-Substraten in Silizium-Dünnschichtsolarzellen, Dissertation, Rheinisch Westfälischen Technischen Hochschule Aachen, 2009.

[121] J.I. Owen, J. Hüpkes, H. Zhu, E. Bunte, S.E. Pust, Physica Status Solidi (a) 208 (2011) 109.

[122] E. Bunte, H. Zhu, EPJ Photovoltaics 2 (2011) 20602.

[123] J. Hüpkes, J.I. Owen, S.E. Pust, E. Bunte, Chemphyschem 13 (2012) 66.

[124] P. Spizzichino, A. Beckmann, The Scattering of Electromagnetic Waves from Rough Surfaces, Artech House, Norwood, MA, 1987.

[125] A. Banerjee, S. Guha, Journal of Applied Physics 69 (1991) 1030.

[126] T. Dekker, J.W. Metselaar, R. Schlatmann, B. Stannowksi, R.A.C.M.M. van Swaaij, M. Zeman, Proceeding of the 20th European PVSEC (2005).

[127] W. Böttler, V. Smirnov, J. Hüpkes, F. Finger, Journal of Non-Crystalline Solids 358 (2012) 2474.

[128] W. Böttler, V. Smirnov, J. Hüpkes, F. Finger, Physica Status Solidi (a) 209 (2012) 1144.

[129] K. Bittkau, T. Beckers, Physica Status Solidi (a) 207 (2010) 661.

[130] K. Bittkau, T. Beckers, S. Fahr, C. Rockstuhl, F. Lederer, R. Carius, Physica Status Solidi (a) 205 (2008) 2766.

# List of publications


[1] W. Böttler, V. Smirnov, A. Lambertz, J. Hüpkes, and F. Finger, "Window layer development for microcrystalline silicon solar cells in n-i-p configuration," Physica Status Solidi (C), vol. 7, no. 3–4, p. 1069, Feb. 2010.

[2] W. Böttler, V. Smirnov, A. Lambertz, J. Hüpkes, and F. Finger, "Front and Back Contacts for Microcrystalline Silicon Solar Cells in n-i-p Configuration," Proceeding of the 25th European PVSEC, p. 3060, 2010.

[3] V. Smirnov, W. Böttler, A. Lambertz, H. Wang, R. Carius, and F. Finger, "Microcrystalline silicon n-i-p solar cells prepared with microcrystalline silicon oxide (μc-SiO x :H) n-layer," Physica Status Solidi (C), vol. 7, no. 3–4, p. 1053, Feb. 2010.

[4] V. Smirnov, W. Böttler, A. Lambertz, O. Astakhov, R. Carius, and F. Finger, "N-type Microcrystalline Silicon Oxide (μc-SiOx:H) Window Layers with Combined Anti-reflection Effects for n-i-p Thin Film Silicon Solar Cells," Proceeding of MRS, vol. 1245, 2010.

[5] V. Smirnov, A. Lambertz, W. Böttler, R. Carius, and F. Finger, "N-Type Microcrystalline Silicon Oxide (mc-Siox:H) Layers for n-Side Illuminated Microcrystalline Silicon n-i-p Solar Cells," Proceeding of the 25th European PVSEC, p. 3165, 2010.

[6] U. W. Paetzold, E. Moulin, D. Michaelis, W. Böttler, M. Meier, R. Carius and U. Rau, "Plasmonic reflection grating back contacts for microcrystalline silicon solar cells," Applied Physics Letters, vol. 99, no. 18, p. 181105, 2011.

[7] W. Böttler, V. Smirnov, J. Hüpkes, and F. Finger, "Variation of back reflector morphology in n–i–p microcrystalline silicon thin film solar cells using texture-etched ZnO," Journal of Non-Crystalline Solids, vol. 358, no. 17, p. 2474, Sep. 2012.

[8] W. Böttler, V. Smirnov, J. Hüpkes, and F. Finger, "Texture-etched ZnO as a versatile base for optical back reflectors with well-designed surface morphologies for application in thin film solar cells," Physica Status Solidi (a), vol. 209, no. 6, p. 1144, Jun. 2012.

[9] K. Bittkau, W. Böttler, M. Ermes, V. Smirnov, and F. Finger, "Light scattering at textured back contacts for n-i-p thin-film silicon solar cells," Journal of Applied Physics, vol. 111, no. 8, p. 083101, 2012.

[10] M. Ermes, W. Böttler, K. Bittkau, and V. Smirnov, "Influence of the Back Reflector Texture on Light Scattering and Performance of a nip-Type Microcrystalline Silicon Thin-Film Solar Cell," Proceeding of the 27th European PVSEC, p. 2628, 2012.

[11] O. Astakhov, V. Smirnov, R. Carius, Y. Petrusenko, V. Borysenko, W. Böttler, F. Finger, "Variation of the defect density in a-Si:H and μc-Si:H based solar cells with 2MeV electron bombardment," Journal of Non-Crystalline Solids, vol. 358, no. 17, p. 2198, Sep. 2012.

# Acknowledgements

At the end of this thesis, I would like to thank all the people who kindly helped and supported me during this work, specially the following people for their contribution:

- Prof. Dr. Uwe Rau, for providing me the opportunity to work in IEK-5 in Forschungszentrum Jülich, one of the world leading research institutions in the field of thin-film photovoltaics.
- Dr. Friedhelm Finger, as my first supervisor, for his guidance, encouragement and scientific discussion throughout this work. His comments and criticism were always very precise and valuable.
- Dr. Vladimir Smirnov, for being an excellent supervisor. I deeply appreciate his patience in the design of experiments, discussion of results and correction of manuscript and this thesis. Also from him, I learned how to work and present results in a scientific way.
- Dr. Karsten Bittkau, for insightful discussion, especially regarding the scattering properties of back reflectors. Moreover, the phase model he developed was successfully used in this work and was very helpful to further understand the relation between the surface morphology, light scattering properties of back reflectors and light trapping in solar cells.
- Dr. Jürgen Hüpkes and Dr. Sascha E. Pust, for the guidance and discussion on etching and surface variation of ZnO films.
- Andreas Lambertz, for his technical support on PECVD and results analysis.
- Alain Doumit, for his technical support on Sputtering of front ZnO layers and results analysis.
- Janine Worbs and Hilde Siekmann, for deposition of ZnO and Ag films.
- Rebecca Van Aubel for technical support on deposition of silicon layers and thermal evaporation of Ag grids.
- All those who helped with sample characterization: Silvia Jorke and Ting Guo, for the AFM measurements; Wilfried Reetz, Carsten Grates and Janis Kroll for I-V and quantum efficiency measurements of solar cells; Markus Hülsbeck and Florian Köhler for the Raman scattering measurements; Sandra Moll for the conductivity measurements; Karsten Bittkau and Alain Doumit for the transmission and reflection measurements; Christoph Zahren and Gabrielle Jost for the angular intensity distribution measurements.

- Dr. Etienne Moulin, Dr. Karsten Bittkau, Dr. Jürgen Hüpkes Dr. Sascha E. Pust, Marek Warzecha, Florian Köhler and Andre Hoffmann, for carefully reading some part of this thesis and giving many valuable suggestions.
- Ulrich W. Paetzold, Matthias Meier, Juraj Hotovy, Markus Ermes and Dr. Oleksandr Astakhov, for the nice cooperation and discussion in many interesting projects.
- Andrea Mülheims, for the organization work on the contracts and her encouragement to complete this thesis.
- All the colleagues in IEK-5 for offering friendly working atmosphere and many colleagues and friends, specially David Wippler, Sacha Van Albada, Dr. Etienne Moulin, Dr. Lihong Xiao, Thi Minh Hang Tran, Juraj Hotovy, Marek Warzecha, Jorj J. Owen, Dr. Bart Pieters, Shiwei Ku, Carilin Ulbrich, Katharina Baumgartner, Jonas Noll, Matthias Meier, Max Siegloch, Andre Hoffmann, Stephan Lehnen, Florian Köhler, Thomas C. Müller, Markus Jäckle, Olga Lyapina, Tao Chen, Ting Guo, Wendi Zhang, Xu Xu and Kaining Ding, for helping me to find more balance between work and rest.
- Finally, special thanks are in order for my husband Marc P. Böttler, my parents and relatives, for their emotional support and encouragement.

Band / Volume 231
**Assessment of Laser Induced Ablation Spectroscopy (LIAS) as a method for quantitative in situ surface diagnostic in plasma environments**
N. Gierse (2014), 199 pp
ISBN: 978-3-89336-994-2

Band / Volume 232
**Lattice-Boltzmann-Simulation in faserbasierten Mikrostrukturen**
J. P. Brinkmann (2014), viii, 129 pp
ISBN: 978-3-89336-995-9

Band / Volume 233
**Numerische Simulationen von Abfallgebinden aus der Wiederaufarbeitung von Kernbrennstoffen**
S. Schneider (2014), 201 pp
ISBN: 978-3-89336-998-0

Band / Volume 234
**Materials for Advanced Power Engineering 2014**
J. Lecomte-Beckers, O. Dedry, J. Oakey, B. Kuhn (Ed.)
(2014), xxi, 930, viii pp
ISBN: 978-3-95806-000-5

Band / Volume 235
**Untersuchungen zur Abtrennung, Konversion und Transmutation von langlebigen Radionukliden**
Ein Beitrag zur fortschrittlichen Entsorgung von hochradioaktiven Abfällen
G. Modolo (2014), 291 pp
ISBN: 978-3-95806-005-0

Band / Volume 236
**Keramische Membranen für die $H_2$-Abtrennung in CO-Shift-Reaktoren**
D. van Holt (2014), IV, 169 pp
ISBN: 978-3-95806-007-4

Band / Volume 237
**Entwicklung von porösen Silica-Membranen zur $CO_2$-Abtrennung aus dem Rauchgas fossil befeuerter Kraftwerke**
J. S. Eiberger (2014), II, 163 pp
ISBN: 978-3-95806-008-1

Band / Volume 238
**Development of a highly sensitive and versatile mass spectrometer system for laboratory and atmospheric measurements**
S. Albrecht (2014), iv, 171 pp
ISBN: 978-3-95806-009-8

Band / Volume 239
**High Temperature Corrosion of Alloys and Coatings in Gas-Turbines Fired with Hydrogen-Rich Syngas Fuels**
W. Nowak (2014), 201 pp
ISBN: 978-3-95806-012-8

Band / Volume 240
**Einfluss neuer Membranmaterialien auf Herstellung und Betrieb von Direktmethanol-Brennstoffzellen**
S. Hürter (2014), V, 164 pp
ISBN: 978-3-95806-013-5

Band / Volume 241
**Spannungsinduziertes Versagen in Hochtemperaturschichtsystemen**
C. Nordhorn (2014), v, 118 pp
ISBN: 978-3-95806-016-6

Band / Volume 242
**Änderungsdetektion digitaler Fernerkundungsdaten mittels objekt-basierter Bildanalyse**
C. Listner (2014), 176 pp
ISBN: 978-3-95806-017-3

Band / Volume 243
**Räumlich hoch aufgelöste Modellierung des Spaltprodukt-verhaltens in einem HTR-Core mit kugelförmigen oder prismatischen Brennelementen**
A. Xhonneux (2014), viii, 239 pp
ISBN: 978-3-95806-020-3

Band / Volume 244
**Effects of Cercospora leaf spot disease on sugar beet genotypes with contrasting disease susceptibility**
S. Schmittgen (2015), 121 pp
ISBN: 978-3-95806-021-0

Band / Volume 245
**Light scattering and trapping in thin film silicon solar cells with an n-i-p configuration**
W. Böttler (2015), 132 pp
ISBN: 978-3-95806-023-4

Weitere ***Schriften des Verlags im Forschungszentrum Jülich*** unter
http://wwwzb1.fz-juelich.de/verlagextern1/index.asp

Energie & Umwelt /
Energy & Environment
Band / Volume 245
ISBN 978-3-95806-023-4